Interfacial issues in wide-bandgap II-VI materials and related multiple quantum well structures

Emanuele Pelucchi

Dissertation (Ph.D. thesis)

to obtain the academic degree

Doktor der Naturwissenschaften (Ph.D.)

Dr. rer. nat.

at Department 1

of the University of Bremen

Bremen, 31-01-2001

Whose woods these are I think I know.
His house is in the village though;
He will not see me stopping here
To watch his woods fill up with snow.

My little horse must think it queer
To stop without a farmhouse near
Between the woods and frozen lake
The darkest evening of the year.

He gives his harness bells a shake
To ask if there is some mistake.
The only other sound's the sweep
Of easy wind and downy flakes.

The woods are lovely, dark and deep,
But I have promises to keep,
And miles to go before I sleep,
And miles to go before I sleep

Robert Frost

Chapter one: Introduction

1.1. Motivation

This work examines a number of unresolved issues, mostly interface related, which affect the behaviour of wide-bandgap II-VI semiconductors and limit their applicability in optoelectronic devices. Such issues include the effect of strain on materials degradation and the possibility of fabricating strain-free devices, and the comparatively high resistivity of metal contacts to wide-bandgap II-VI materials.

Our interest in this area has been motivated by recent efforts to implement a viable blue-green optoelectronic technology based on II-VI semiconductors. II-VI based blue-green lasers operating at liquid nitrogen temperature under pulsed current injection were demonstrated in 1991.[1,2] Continuous-wave (cw) operation at room temperature was achieved a couple of years later.[3,4] Since then substantial progress has been made but device lifetimes still barely exceeds 400 hours at room temperature.[5,6]

State-of-the-art blue-green lasers based on II-VI semiconductors are mostly fabricated by molecular beam epitaxy (MBE) on GaAs(001) wafers. Typical devices include cladding and waveguiding $Zn_yMg_{1-y}S_zSe_{1-z}$ layers lattice-matched to GaAs, and pseudomorphic $Zn_{1-x}Cd_xSe$ alloy quantum wells (QWs) as lasing materials.[5,7] A representative II-VI laser structure in shown in Fig. 1.[8]

By employing $Zn_{1-x}Cd_xSe$ quantum wells as active layers the emission wavelength of the device can be tuned gradually from the blue to the green range with increasing x in the alloy, but the corresponding increase in lattice parameter also augments the lattice mismatch with the substrate. Large strains are present in the pseudomorphic QWs as a result of the substantial lattice mismatch with the GaAs substrate (1-3% in-plane strain for x=0.10-0.30, typical concentrations for blue and green emitters).

Several authors have pointed out that the highly strained nature of the QWs may play a

role in promoting device degradation.[8,9,10] Bonard et al.[10] reported that the degradation rate of electron-beam-pumped $Zn_{1-x}Cd_xSe/ZnSe$ graded-index separate confinement heterostructure (GRINSCH) lasers depended critically on the strain in the quantum well.[10]

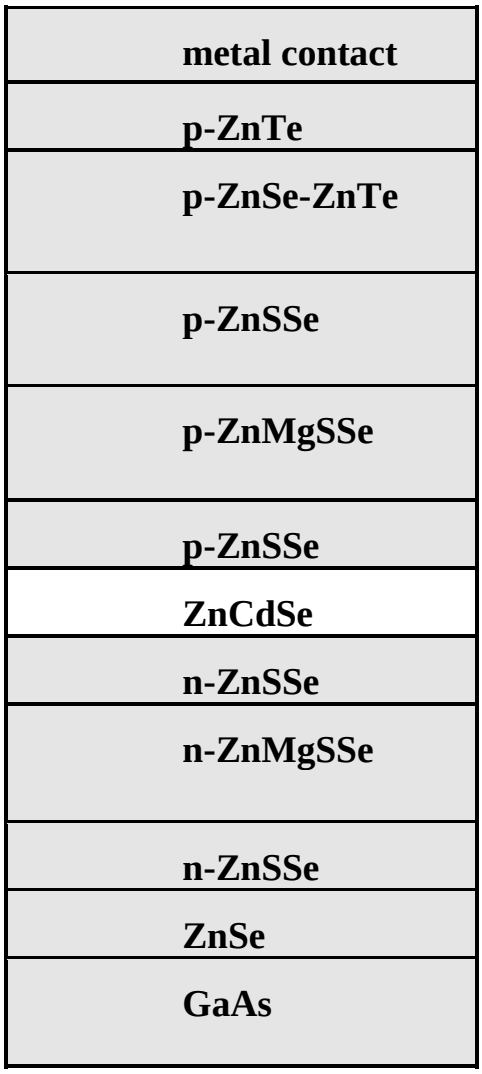

FIG. 1 Representative II-VI laser structure, adapted from Ref. 8. The layer sequence includes an n-GaAs buffer, a ZnSe buffer to avoid direct contact between GaAs and sulphur containing layers, an n-ZnSSe buffer, an n-ZnMgSSe cladding layer about 1.5 μm thick, doped at a few 10^{17} cm^{-3}, an n-ZnSSe optical guiding layer (~100 nm-thick), an undoped ZnCdSe strained quantum well (from 10% to 35% Cd, few nm-thick), a p-ZnSSe optical guiding layer (~100 nm), a p-ZnMgSSe cladding layer about 1,5 μm thick, doped at a few 10^{17} cm^{-3}, p-ZnSSe, p-ZnSe-ZnTe precontact structure, p-ZnTe contact (highly p-doped). The composition of the cladding and optical guiding alloys are chosen in order to have the same lattice parameter as GaAs.

Toda et al.[8] discussing the formation of dark-line defects in laser diodes, proposed that defect formation originated from the co-operative effect of Zn/Cd interdiffusion across the QW boundaries and strain relaxation in the quantum well region.[8] Vogelgesang et al.[9] suggested that the strain in the quantum well region could act as the major driving force for defect propagation.

All this should encourage research towards the development of novel II-VI emitters where no strain is present in the QW region, in order to eliminate any possible strain-assisted degradation. Efforts to remove strain from the ZnCdSe QWs envision II-VI growth on non-conventional substrates, such as InP, or graded-composition $In_{1-x}Ga_xAs$ buffer layers lattice-matched to the $Zn_{1-x}Cd_xSe$ quantum wells.[11,12,13] To achieve sufficient optical quality on such novel substrates is a challenging task, further complicated by the need to develop new lattice-matched cladding and waveguiding layers. Prospective materials in this include a number of Mg- and/or Be-containing multinary alloys, but only limited information is available about the electronic and structural properties of such materials. Moreover, little is known about the properties of the corresponding interfaces, which will have a crucial role in determining device performances. Carrier confinement, for example, and the resulting exciton stability, which often determine the main recombination mechanism in II-VI emitters,[14,15] are virtually unexplored in these new, strain-free structures.

In this area we have elected to focus on the implementation of lattice-matched emitters on graded composition $In_xGa_{1-x}As$ buffer layers on GaAs (001) wafers. As prototype structures we have selected lattice-matched $Zn_{1-y}Cd_ySe/Zn_{1-z}Mg_zSe$ multiple quantum wells. This required a detailed analysis of the structural and electronic properties of $Zn_{1-z}Mg_zSe$ alloys, an investigation of the band alignment across $Zn_{1-y}Cd_ySe/Zn_{1-z}Mg_zSe$ heterojunctions, and characterization of the structural quality, carrier confinement and excitonic properties of the resulting strain free multiple quantum well structure.

The issue of comparatively high resistivity of metal contacts to wide-bandgap II-VI materials stems directly from the low p-type dopability of Se-based II-VI compounds. The transport properties of metal/semiconductor interfaces in most devices are customarily tuned by controlling the doping level of the semiconductor in the near-junction region. ZnSe, however, can

be p-doped up to 10^{18} cm^{-3} and no suitable metal/ZnSe ohmic contact is available.[16,17,18] The p-type dopability becomes even smaller in the wider-gap, ZnMgSSe materials. The use of Te compounds, which can be highly doped p-type, has only partially overcome this problem, through the design of complex contact schemes, such as graded p-ZnTe/ZnSe superlattices,[19] which are highly defected and prone to degradation, and at this time do not guarantee a long-enough lifetime.[18,20] All this should stimulate research into nonconventional methods of controlling the effective Schottky barrier height and therefore contact performance. For example recent work on III-V interfaces have shown that appropriate chemical modifications of the local interface environment can be used to create a local interface dipole and induce a wide tunability of the Schottky barrier height. Such phenomena are largely unexplored in the case of metal/II-VI junctions.

In this area we have concentrated on the identification of prototype metal/II-VI contacts in which to explore the possibility of tuning the transport properties through the local modifications of the interface environment. We selected, in particular, the Zn/ZnSe (001) junctions, since, based on thermodynamic arguments, it was expected to exhibit an ideally unreactive character, and Au/ZnSe (001) contacts, which has been widely studied in recent years, in view of the importance of Au metallizations in current devices, and reportedly exhibits unexpected lateral inhomogeneities.

We were able to show that the Zn/ZnSe (001) interface shows indeed ideal unreactive behaviour, while the lateral inhomogeneities of the Au/ZnSe junctions might reflect an hitherto unreported interface reactivity leading to an inhomogeneous defect distribution. Finally, to demonstrate Schottky barrier control through modifications of the local interface environment, we inserted Zn monolayers at the interface between Au and ZnSe (001) and examined the resulting change in the transport properties.

The thesis is organized as follows: in Chapter 2 we concentrate on the description of our experimental apparatus and on the characteristics of the III-V compounds which have been used as substrates for the different II-VI layers presented in the thesis. Results on structural and electronic properties of $Zn_{1-y}Mg_ySe$ alloys are discussed in Chapter 3. Chapter 4 presents

photoemission spectroscopy results and theoretical studies of lattice matched $Zn_{1-x}Cd_xSe/Zn_{1-y}Mg_ySe$ heterojunctions. Chapter five is dedicated to TEM studies and optical absorption of strain-free $Zn_{1-x}Cd_xSe/Zn_{1-y}Mg_ySe$ multiple quantum well structures grown on lattice matched InGaAs buffer layers. In Chapter six we examine the prototype ideally unreactive Zn/ZnSe contacts. Au/ZnSe is instead investigated in Chapter seven, together with the possibility to improve the lateral homogeneity and to tune the Schottky barrier by appropriate insertion of Zn interlayers in Au/ZnSe junctions. Finally, we summarize our conclusions in Chapter 8.

Chapter two: Experimental notes

2.1. Our growth facility

Fig. 1 shows a schematic representation of the ultra-high-vacuum (UHV) deposition and characterization facility used in this work. It includes two twin Riber molecular beam epitaxy (MBE) growth chambers, a photoemission analysis chamber and a metallization chamber, interconnected via six ultra high vacuum modules. A sample cart, that can contain up to eight three inch sample holders in molybdenum (molyblocks), can be moved through the six modules. The first module, to the right in Fig. 1, is the fast-entry introduction module, with a base pressure in the low 10^{-7} Torr range, assured by an ion pump. The module is isolated from the others by an UHV gate valve, so that it can be vented to remove or introduce

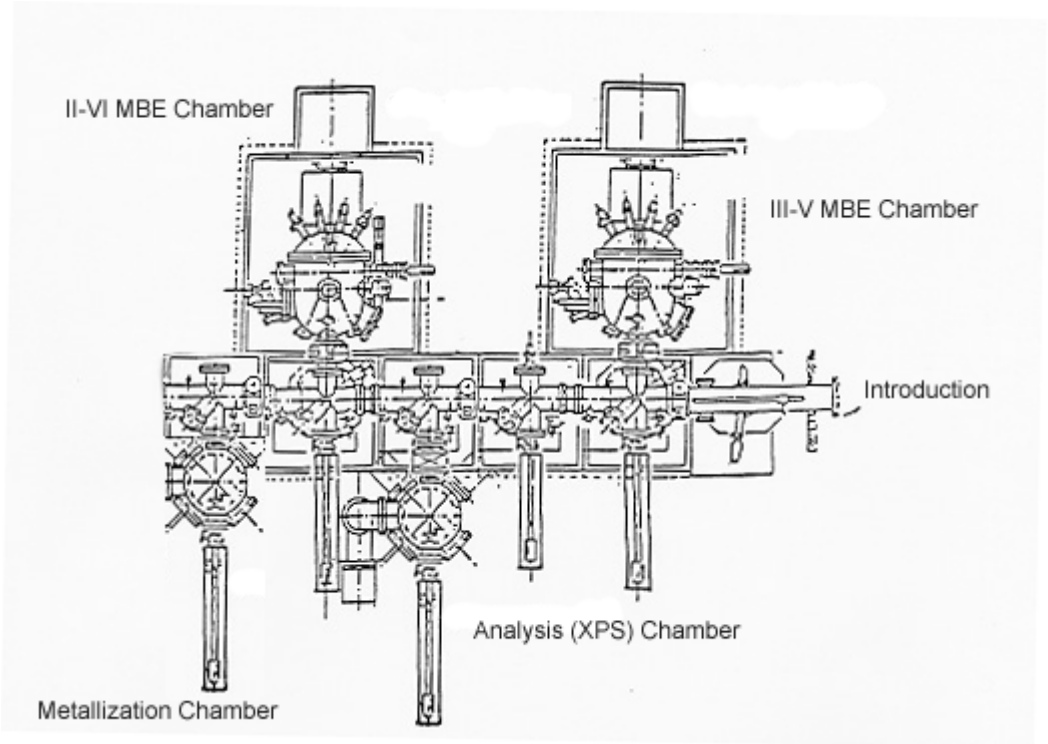

FIG. 1 Our growth facility.

samples from/to the cart without breaking the vacuum in the rest of the system. The introduction module is located within a class 1000 clean room so that samples can be transferred in a clean environment to the lithography facilities of the laboratory.

The first MBE chamber is devoted to the growth of III-V materials, and includes 7 conventional effusion cells (for Al, In, Ga, As, Si and Be) and a radio frequency plasma cell for nitrogen. The chamber is pumped by an ion pump, a titanium sublimation pump and by a CTI cryopump, and is equipped with liquid nitrogen (LN) filled cryopanels to improve the system pressure during growth. The base pressure of the chamber, prior to As evaporation, is in the low 10^{-11} Torr range. The sample holder is resistively heated and allows sample rotation to increase layer homogeneity during growth. An ion gauge lodged on the manipulator can be positioned at the sample location to measure beam equivalent pressures of the elements. A 10 keV reflection high energy electron diffraction (RHEED) apparatus allows monitoring of surface quality and reconstructions during growth. A quadrupole mass spectrometer is used to sample residual gas composition.

The second MBE chamber is dedicated to II-VI materials growth. Seven conventional effusion cells allow evaporation of Zn, Cd, Mg, Se and Te. A solid $ZnCl_2$ source provides n-type doping, while a radio frequency plasma source for nitrogen is used for p-type doping. The chamber is pumped by an ion pump, a titanium sublimation pump, an Edwards cryopump and LN cryopanels. Base pressure is in the low 10^{-11} Torr. As for the III-V chamber, the sample manipulator allows sample heating (up to 800 degrees), it contains an ion gauge which is used for flux measurements and allows sample rotation to increase layer homogeneity during growth. A 10 keV RHEED apparatus is also present together with a quadrupole mass spectrometer.

After growth, the semiconductor samples can be transferred in UHV through the different modules, which are typically at an operating pressure in the low 10^{-10} Torr range, being pumped by ion pumps and titanium sublimation pumps.

The metallization chamber was used to fabricate in situ a number of metal/II-VI contacts. The design, construction and installation of this chamber has been part of our work. Fig. 2 shows a photograph of the metallization chamber. The chamber contains a simple, non-heatable sample manipulator, three effusion cells, a quartz crystal thickness monitor. It is pumped by an ion pump,

a titanium sublimation pump and LN cryopanels, while its operating pressure is in the 10^{-11} Torr range.

The UHV analysis chamber contains an SSX-100 monochromatic x-ray photoemission (XPS) spectrometer. The chamber is pumped by an ion pump and a nonevaporable getter pump (NEG). The combination of the two keeps the chamber in the low 10^{-11} Torr range. An optical microscope allows visual inspection and positioning of the sample, held by an x, y, z, φ manipulator. The spectrometer includes a variable spot size x-ray source adjustable from 150 microns to 1000 microns in four step (150, 300, 600, 1000), a high-throughput bent quartz crystal x-ray monochromator providing monochromatic Al Kα radiation (1486.6 eV photon energy), a large collection angle electron lens system and a 40-millimeter high-resolution channelplate (128

FIG. 2 Our new metallization chamber.

channels). The total system energy resolution is a function of the source spot size and of the analyzer resolution. Calibration of the Fermi level of the spectrometer and of the overall energy resolution was obtained respectively by measuring the Au 4f core levels positions and their full width half maximum. The data discussed in this work were acquired by operating the XPS apparatus with a source spot size of 300 microns, and with an overall system resolution of about 0.8 eV.

2.2. III-V substrates

In the framework of this work, we used the III-V MBE chamber to fabricate GaAs layers on GaAs (001) wafers as substrates for ZnSe, ZnCdSe or ZnMgSe growth. After thermal removal of the native oxide under As flux, micron-thick GaAs layers were grown at 600 °C. The beam equivalent pressure of As, as determined by the ion gauge positioned at the sample location, was in the high 10^{-6} Torr range. The III/V beam pressure ratios (BPR) was typically in the 1/20 range.

All layers exhibited the As-stabilized 2x4 surface reconstruction during growth. The III-V substrates were then either directly transferred to the II-VI MBE chamber or capped with As in the III-V chamber and stored in air.[21] To fabricate the amorphous As cap layer, the sample was cooled down to about -30 °C in the growth chamber, and then exposed to the same As flux used during GaAs growth for about an hour. The resulting As cap layer, 0.5 to 1 micron thick, protected the GaAs surface against oxidation and, in general, contamination.[22] The cap layer was removed upon annealing at around 450 °C in the II-VI chamber immediately prior to II-VI growth. The resulting GaAs (001)2x4 surfaces exhibit morphology and atomic scale roughness comparable to those of surfaces grown in situ.[21,22] II-VI layers were grown on GaAs (001) 2x4 surfaces since several authors have reported that ZnSe growth on such surface reconstructions leads to a 2D, layer-by layer-growth mode, and comparatively lower densities of threading dislocations.[23]

Alternatively, InGaAs buffer layers were synthesized on GaAs (001) wafers in the III-V chamber as lattice matched substrates for II-VI growth of $Zn_{0.85}Cd_{0.15}Se/Zn_{0.74}Mg_{0.26}Se$ (see Chapter 3, 4, 5 for further details) multiple quantum wells structures. After initial growth of a 0.5 μm thick GaAs buffer, 1 μm-thick InGaAs epilayers were grown at 500 degrees with III/V beam

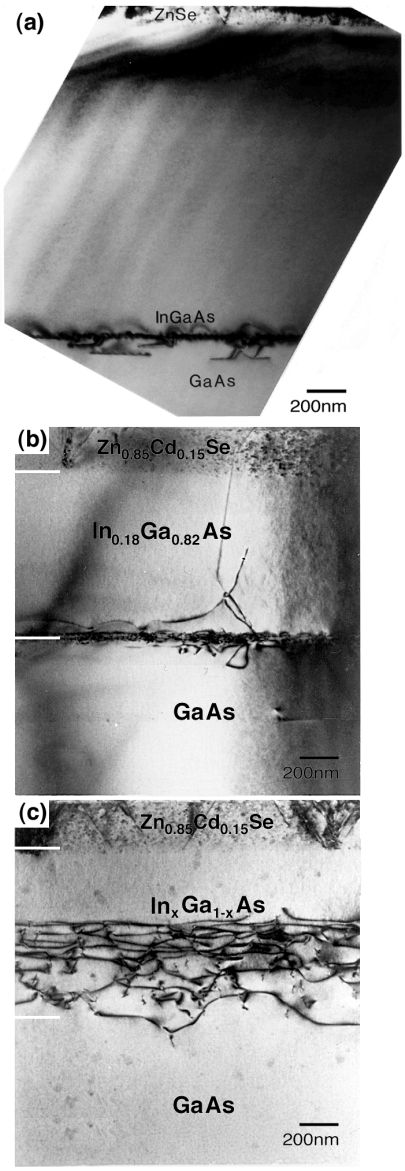

FIG. 3 (a) TEM micrograph of a ZnSe/$In_{0.05}Ga_{0.95}As$/GaAs(001) heterostructure which includes a 100-nm-thick ZnSe epilayer and a 2- mm-thick, homogeneous composition $In_{0.05}Ga_{0.95}As$ layer. The cross-sectional image was obtained in two-beam diffraction conditions near the [1$\bar{1}$0] zone axis. (b) Cross-sectional TEM micrograph of a $Zn_{0.85}Cd_{0.15}Se/In_{0.19}Ga_{0.81}As$/GaAs heterostructure incorporating a 300-nm-thick II–VI overlayer and a ~1-μm-thick, homogeneous composition $In_{0.19}Ga_{0.81}As$ layer. (c) Cross-sectional TEM micrograph of a $Zn_{0.85}Cd_{0.15}Se/In_xGa_{1-x}As$/GaAs heterostructure incorporating a 300-nm-thick II–VI overlayer and a ~1-μm-thick, graded composition $In_xGa_{1-x}As$ layer in which the In concentration exhibited a parabolic, superlinear profile from x=0 at the bottom to x_0=0.23 at the top.[11]

pressure ratios (BPR) in the 1/15-1/30 range. Typical growth rates were between 1 and 1.3 μm/h. With the growth conditions employed, the InGaAs layers exhibited a 3x1 surface reconstruction, as determined by RHEED. The samples were then As capped with the same procedure described

above for GaAs. A 3x1 or 2x4 As rich surface reconstruction can be obtained, depending on the annealing procedure, by desorption of the As layer in the II-VI chamber immediately prior to II-VI growth.

In order to achieve lattice matching to $Zn_{0.85}Cd_{0.15}Se$ active layers (and to the corresponding $Zn_{0.74}Mg_{0.26}Se$ cladding layers), whose lattice parameter is 5.73 Å, $In_xGa_{1-x}As$ wafer with x=0.19 would be necessary. However, since high quality $In_xGa_{1-x}As$ wafers with x>0.02 are not available because of homogeneity problems in high-x ternary alloys during bulk crystal growth, constant composition $In_{0.19}Ga_{0.81}As$ layers grown on GaAs wafers have to be taken into account as a possible solution. Still, the use of constant composition $In_{0.19}Ga_{0.81}As$ layers is not straightforward. The lattice mismatch between GaAs and $In_{0.19}Ga_{0.81}As$ is 1.35%,[24] and is accommodated partly by misfit dislocations (MDs) and partly by elastic strain.[25] Also, $In_xGa_{1-x}As$ layers of practical thickness (a few microns) grown on GaAs are unlikely to be fully relaxed and residual strain has to be taken into account when constant composition layers are grown as substrates for II-VI layers.[26,27] This can be accomplished even if a satisfactory equilibrium theory which describes strain release in $In_xGa_{1-x}As$/GaAs heterostructures does not exist, as a phenomenological relaxation rate has been empirically found.[25] Provided that the growth proceeds two-dimensionally, it has been found that the residual parallel strain follows the general expression:

$$\varepsilon_{//}^2 T=(0.0037\pm0.0007)\ \text{nm}, \qquad (1)$$

where T is the total layer thickness.[11,24,25,28] Since the quantity $Y\varepsilon_{//}^2 T=YK$ (where Y is the Young modulus) in an homogenous-composition film is the elastic energy per unit surface, equation (1) can be interpreted as if MDs are nucleated when a critical elastic energy per unit surface is exceeded.[25,29] Using equation (1) one finds that to achieve lattice matching to $Zn_{0.85}Cd_{0.15}Se$ with one micron thick $In_xGa_{1-x}As$ layer, an In concentration x=0.22 is needed, instead of x=0.19.

If the required In concentration is low enough, the use of homogeneous composition $In_xGa_{1-x}As$ layers on GaAs (001) as substrates for II-VI growth is a suitable option. Fig 3(a) shows a cross-sectional transmission electron microscopy (TEM) micrograph of a ZnSe/In_xGa_{1-}

$_x$As/GaAs heterostructure incorporating a 2-μm-thick ternary buffer layer with homogeneous composition x=0.05[11]. At the interface between the ternary III–V layer and GaAs, a misfit dislocation network can be seen. The dislocations are confined near the interface, and no threading defects are observed within the $In_xGa_{1-x}As$ ternary layer or the ZnSe overlayer. From plan-view studies the authors estimated an upper limit of less than $2x10^4$ cm^{-2} for the threading dislocation density in the II–VI overlayer.[11]

On the other hand when the mismatch between the II–VI/III–V heterostructure and the GaAs substrate becomes too high, homogeneous composition $In_xGa_{1-x}As$ layers become less suitable for the purpose. Two order of problems can be found. First, the growth of highly strained $In_xGa_{1-x}As$ epitaxial layers on GaAs(001) undergoes a 2D-3D growth mode transition beyond the critical thickness. The driving force of this transition is the strain relief by elastic deformation at the free edges of the 3D islands.[30] The island coalescence results then in a high density of misfit dislocations, affecting the quality of the $In_xGa_{1-x}As$ layers.[30,31] The second problem, somehow related to the first one, is dislocation interaction, which is known to enhance the nucleation of additional dislocations since the already-present threading segments are prevented from gliding further.[32] The result is a number of TDs affecting the ternary III–V layers. As an example Fig. 3(b) shows a cross-sectional TEM micrograph of a $Zn_{0.85}Cd_{0.15}Se/In_{0.19}Ga_{0.81}As/GaAs$ heterostructure incorporating a 300-nm-thick II–VI overlayer and a 1-μm-thick, homogeneous composition $In_{0.19}Ga_{0.81}As$ layer.[11] Although the vast majority of the misfit dislocations are at the $In_xGa_{1-x}As$/GaAs interface, the larger dislocation interaction, as compared to Fig. 3(a), is seen to be accompanied by the emergence of a number of threading dislocations (TDs), which affect both the bulk of the ternary III–V layer and the II–VI overlayer.

To reduce the number of TDs and avoid three-dimensional (3D) growth which hinders fabrication of high-quality $In_xGa_{1-x}As$ layers with high In concentration on GaAs, graded composition $In_xGa_{1-x}As$ buffer layers were employed in this work. In these layers the In concentration is varied gradually from x=0 at the interface with the substrate to the desired $x=x_0$ at the surface, i.e., at the II–VI/III–V interface. Several authors have showed that a superlinear concentration profile is effective in confining MDs away from the sample surface while minimizing dislocation interactions and TDs generation.[11,12,25,28,29]

We employed the following parabolic In concentration profile:

$$x(t)=x_0\left[1-\left(1-\frac{t}{T}\right)\right]^2 \qquad (2)$$

where t is the distance from the GaAs substrate and T is the total thickness of the $In_xGa_{1-x}As$ layer. The profile in Eq. (2) was selected[11] for its simplicity and relatively flat behaviour in the near-surface region, which makes it less sensitive than other profiles to variations in composition and layer thickness. The corresponding residual strain at the film surface in the direction parallel to the interface $\varepsilon_{//}$ has been calculated from the following expression, obtained through a semi-empirical model of strain relaxation:[11,12,25,28]

$$\varepsilon_{//}^{5}=\left(\frac{9K}{4}\right)^2\frac{x_0}{T^2}\left(\frac{a_0(\mathrm{InAs})}{a_0(\mathrm{GaAs})}-1\right) \qquad (3)$$

where a_0(InAs) and a_0(GaAs) are the equilibrium (unstrained) lattice parameters for the binary parent compounds. In any layer of finite-size thickness the relaxation will have only a partial character. For example, in order to obtain a surface lattice parameter that matches that of a

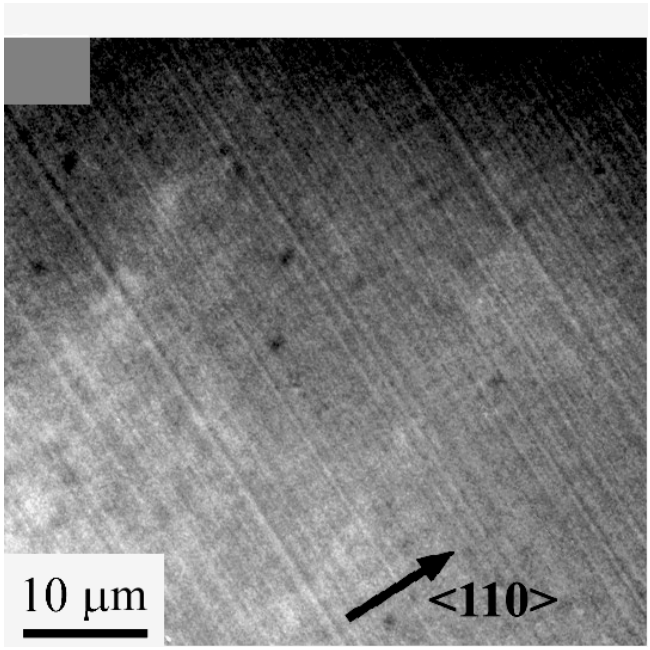

FIG. 4 Nomarski microscopy images of the surface of an $In_xGa_{1-x}As$ graded-composition buffer.[12]

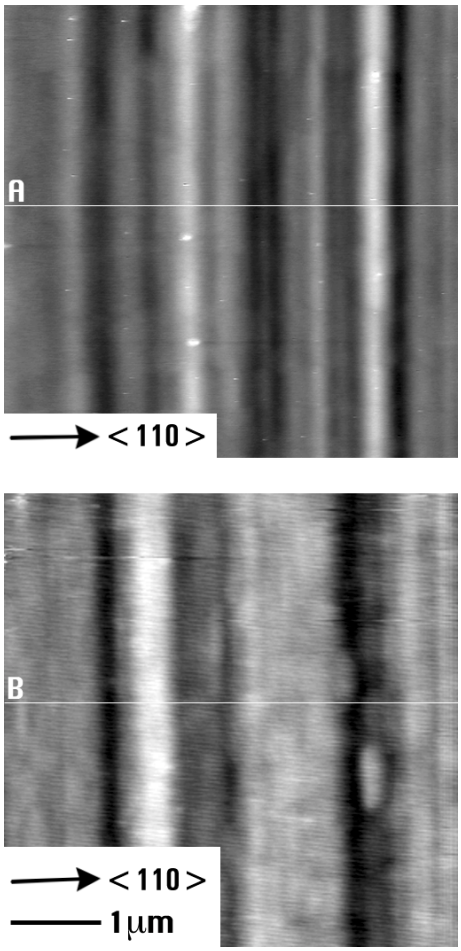

FIG. 5 AFM analysis of the surface morphology of a homogenous-composition $In_{0.19}Ga_{0.81}As$ epilayer on GaAs (top), and a graded-composition $In_xGa_{1-x}As$ buffer on GaAs (bottom). The full grey scale corresponds to a vertical range of 20 nm (top image) And 10 nm (bottom image). The measured rms surface roughness was 3.9±1 and 2.5±0.3 nm for homogenous- and graded-composition buffers, respectively. The quoted uncertainty on the roughness is the standard deviation on a set of ~10 measurements from different regions of the surface. Representative line scans, labelled (A) and (B), are shown in Fig. 6.[12]

$Zn_{0.85}Cd_{0.15}Se$ quantum well layer using an $In_xGa_{1-x}As$ graded layer with T=1100 nm, the surface composition should be x_0=0.245, well above x=0.19 which corresponds to lattice matching in bulk, relaxed $In_xGa_{1-x}As$ and $Zn_{0.85}Cd_{0.15}Se$ alloys. Fig. 3(c) shows[11] a cross-sectional TEM micrograph of a $Zn_{0.85}Cd_{0.15}Se/In_{0.19}Ga_{0.81}As/GaAs$ heterostructure incorporating a 300-nm-thick II–VI overlayer and a 1-μm-thick, graded composition $In_xGa_{1-x}As$ layer in which the In concentration exhibited the parabolic, superlinear profile of equation (2), with x=0 at the interface and x=0.23 at the top. MDs are seen to be distributed throughout a region approximately 500 nm wide, gradually relaxing most of the misfit within this region, and leaving the remaining portion

of the buffer unaffected, in agreement with theoretical predictions.[11,12,25,28,33] Within the experimental sensitivity, no TDs are observed.

Fig. 4 shows a Nomarski microscopy image of an $In_xGa_{1-x}As$ graded buffer[12] (final composition 24% In). The image shows parallel corrugations extending along the $[1\bar{1}0]$ direction and smaller perpendicular corrugations extending in the [110] direction. This type of surface roughness is known to occur in both $In_xGa_{1-x}As$ layers on GaAs as well as for example in $Si_{1-x}Ge_x$ epilayers.[27,31,32,34,35] The surface corrugations that form the crosshatch pattern have been related to the misfit dislocation network at the overlayer/substrate interface, based on their orientation, and on the fact that they are not observed in layers which do not contain substantial numbers of glissile MDs.[12,34,35]

Fig 5 shows atomic force microscopy (AFM) images of a graded-composition $In_xGa_{1-x}As$ buffer (bottom), and a homogenous-composition $In_xGa_{1-x}As$ (x=0.19) layer (top), both 1μm-thick.[12] The smoother appearance of the surface of the graded-composition buffer is borne out by the quantitative comparison of the root-mean-square (rms) roughness. As a statistically significant figure of merit of the surface quality the rms roughness Δ is taken. For one (1D) and two-dimensional (2D) roughness definitions are as follows:

$$\Delta_{1D,\,2D}=\sqrt{\left\langle\left(h-\langle h\rangle_{1D,\,2D}\right)^2\right\rangle_{1D,\,2D}}=\sqrt{\left\langle h^2\right\rangle_{1D,\,2D}-\langle h\rangle_{1D,\,2D}^2} \qquad (4)$$

where *h* is the surface elevation of a given point within the AFM image (2D) or within a cross section along the desired surface direction (line scan, 1D). Line scans along the perpendicular [110] [Fig. 6(a),(b)] and $[1\bar{1}0]$ (not shown) directions in Fig. 5 revealed a rms (2D) surface roughness of 3.9±1 and 2.5±0.3 nm for homogenous- and graded-composition buffers, respectively.[12] The interesting implication of these results is that although the In concentration at the surface of the graded-composition buffer is 28% *larger* than that of the homogenous-composition buffer, its surface turns out to be 36% *smoothe*r. In contrast with the expected trend of increasing surface roughness with increasing In concentration in the alloy,[34] a graded-composition buffer also helps reducing the surface corrugation. Müller et al.[12] tentatively associated the more favourable surface morphology of the graded-composition buffer as

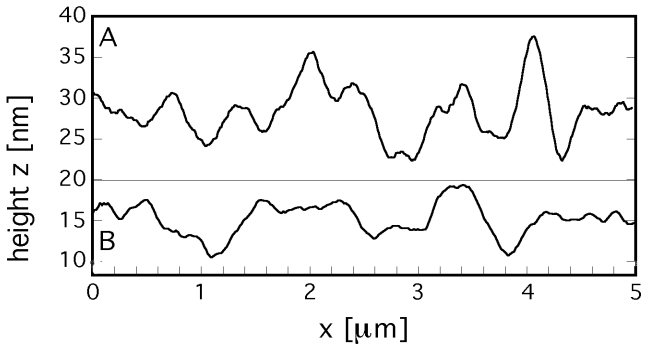

FIG. 6 AFM line scans of the surface of a homogenous-composition $In_{0.19}Ga_{0.81}As$ epilayer on GaAs (top), a graded-composition $In_xGa_{1-x}As$ buffer on GaAs (bottom). The full AFM images can be found in Fig 5. Compared to the homogenous-composition InGaAs buffer, the graded-composition buffer is about 35% smoother.

compared to the homogeneous-composition buffer with the different depth distribution of the MD network depicted in Fig. 4. They proposed that the different distribution affects the concentration of dislocation multiplication sources and the related dislocation bands and pileups. The latter inhomogeneities in the dislocation distribution have been associated with the presence of surface corrugations in $In_xGa_{1-x}As$ alloys on GaAs either because of local fluctuations in the growth rate[34] or due to slip-step formation at the surface.[27]

The value of approximately one μm in thickness selected in our work derives from a compromise between the requirements of minimum threading dislocation density (which decreases with thickness)[25] and minimum surface roughness (which increases with thickness).[34] Still, surface corrugation can not be eliminated from this type of buffers, and the possibility that such roughness affects the quality of the II-VI epilayers needs to be investigated.

Chapter three: ZnMgSe bulk properties

3.1. Literature review and motivation

Ternary and quaternary alloys containing up to 30/40% Mg are widely used in most II-VI device structures. This has motivated several studies of the structural properties of Mg containing layers, including the simple $Zn_{1-x}Mg_xSe$ ternary layer. Nevertheless contradictory results can be found in the literature.[36,37,38,39,40]

To our knowledge Jobst et al.[36] have published the only report about bandgap and lattice parameter of $Zn_{1-x}Mg_xSe$ alloys throughout the whole Mg concentration range. The most striking result by Jobst et al. is the report of a nonlinear dependence (bowing) of the lattice parameter on composition. A substantial bowing was also reported for the bandgap measured by means of optical transmission and reflection. The lattice parameter was determined by x-ray diffraction (XRD) and the composition by electron probe micro analysis (EPMA). The authors reported the use of standards for calibrating the EPMA apparatus, but no more detail was given. The reported lattice parameter dependence on concentration followed the equation:

$$\mathbf{a}(Zn_{1-y}Mg_ySe)(y)=\mathbf{a}(ZnSe)+[\mathbf{a}(MgSe)-\mathbf{a}(ZnSe)-b_a]y+b_ay^2;\ b_a=-0.07 \text{ and } \mathbf{a}(MgSe)=5.91Å$$

where **a(**ZnSe) (5.6687Å)[36,41] and **a**(MgSe) are ZnSe and MgSe lattice constants respectively. Jobst et al. data covered the 0-95 % Mg range, and the MgSe lattice constants was one of the free parameters of the fit from which the above equation was obtained. The resulting value of 5.91Å for **a**(MgSe) agreed well with the experimentally-determined value of 5.904Å, reported by Litz et al.[42]. The reported room temperature (RT) bandgap value as a function of concentration was:[36]

$\mathbf{E}(Zn_{1-y}Mg_ySe)(y)=\mathbf{E}(ZnSe)+[\mathbf{E}(MgSe)-\mathbf{E}(ZnSe)-b_E]y+b_Ey^2$; $b_E=0.4$ and $\mathbf{E}(MgSe)=4.0$ eV

where $\mathbf{E}(ZnSe)$ (2.68eV)[36,43] and $\mathbf{E}(MgSe)$ are ZnSe and MgSe bandgaps respectively. The MgSe bandgap was one of the free parameters of the fit from which the above equation was obtained. The resulting value $\mathbf{E}(MgSe)=4.0$ eV is close to the value of 4.05 eV determined by Lunz et al.[44].

Somewhat different and conflicting results have been reported by other groups. Okuyama et al.[37] measured the Mg concentration x by EPMA, the lattice constant by XRD and bandgap by photoluminescence (PL) at RT too. Measured samples (up to 50% Mg) reportedly showed no bowing neither in the lattice parameter nor in the bandgap as a function of concentration. Extrapolation of the data to Zn 0% concentration would lead to a MgSe lattice constant of 5.89Å and a RT bandgap of 3.59 eV. This would suggest a low temperature (LT) bandgap of about 3.79 eV.[45]

Puls et al.[38] reported no bowing for the lattice dependence on composition in the x=0 to x=0.30 concentration range evaluated by EPMA. The MgSe lattice constant value extrapolated from the data value is distinctly larger than previously reported values, 5.964+/-0.25 Å, but the quoted error is substantial. The bandgap value determined by PL, assuming a constant exciton binding energy of 18 meV throughout the whole concentration range, was found to depend linearly on concentration with an extrapolated LT value of 4.1 eV. This would suggest a RT bandgap value of 3.91 eV.[45]

A different way for evaluating the Mg concentration was exploited by Vögele et al.[39], which sampled ZnMgSe alloys with x<40% by means of secondary ion mass spectrometry (SIMS). The low temperature bandgap was evaluated from reflectivity measurements. These authors found no evidence of bowing for the lattice parameter. The extrapolated value of MgSe lattice parameter was 5.894Å, very close to the lattice constant found by Okuyama et al.. The LT

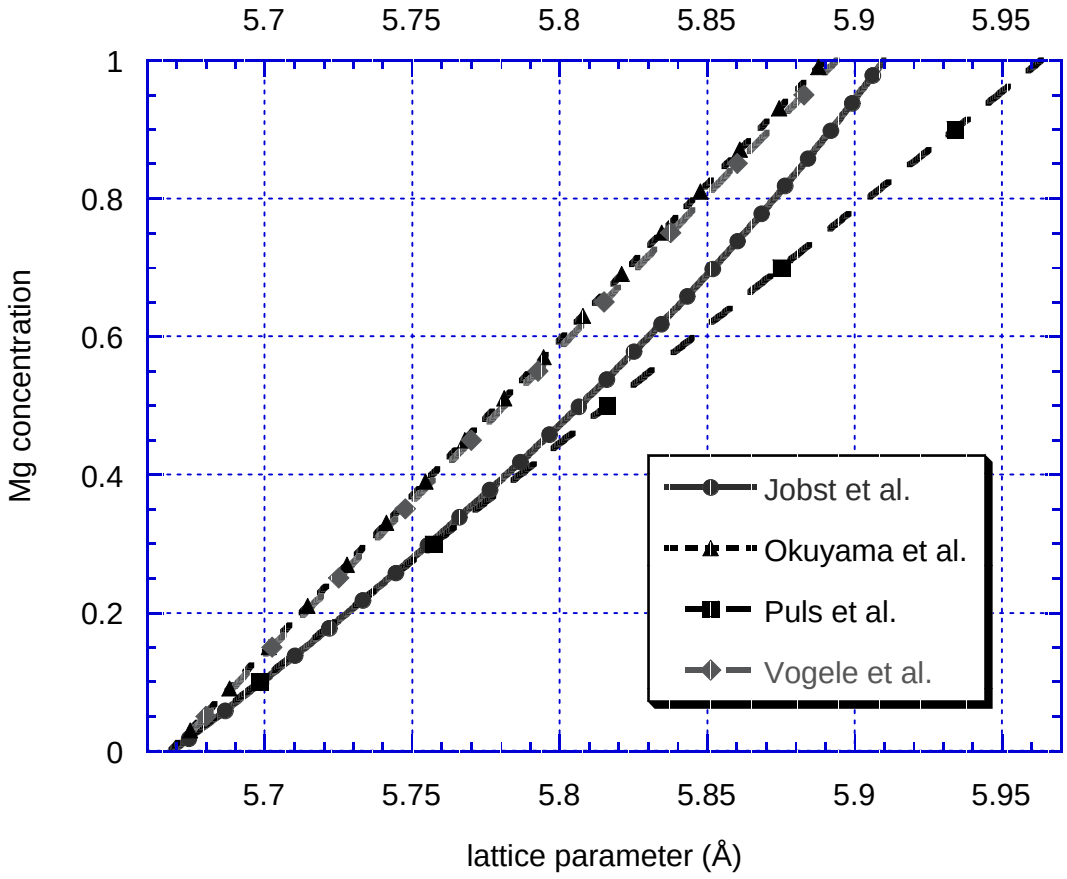

FIG. 1 Experimental concentration vs. lattice parameter dependence reported by Jobst et al [36], Okuyama et al.[37], Puls et al.[38] and Vögele et al.[39]. Only Jobst et al. sampled the lattice dependence on Mg concentration of $Zn_{1-x}Mg_xSe$ over the whole concentration range. The data by the other groups have been extrapolated to 100% Mg for the sake of comparison.

bandgap value for MgSe was 3.85 eV and the bowing parameter in the bandgap vs. x functional dependence was b_E=0.350 eV.

Wörz et al.[40] only measured the bandgap dependence on lattice parameter for 0<x<40%. Their values have been obtained by optical absorption spectroscopy and XRD. Using the lattice parameter vs. x dependence by Jobst they found a LT dependence of the exciton absorption energy given by $E_{ex}(x)$=2.803+0.95x eV. They also measured the exciton binding energy R for 0<x<12% and found: R(x)=20+37.5x meV. No bowing was reported and the extrapolated value for the LT gap of MgSe was 3.81 eV.

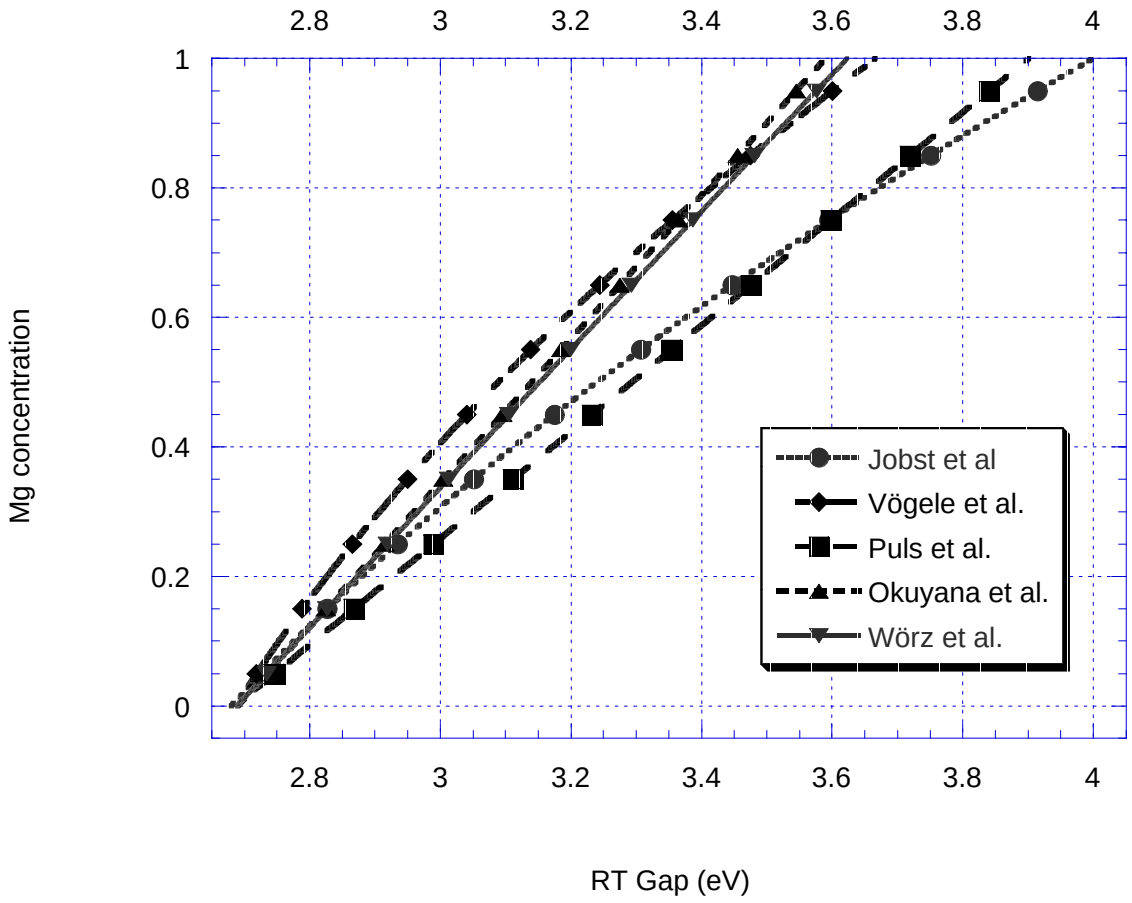

FIG. 2 Experimental concentration vs. bandgap dependence reported by Jobst et al.[36], Okuyama et al.[37], Puls et al.[38], Wörz et al.[40]* and Vögele et al.[39]*. For the sake of comparison LT data (*) have been extrapolated to RT.*

The existing theoretical literature on this subject is rather limited. We are aware of a couple of theoretical reports on bulk MgSe.[46,47] A theoretical study of the quaternary alloy Zn(1-x)Mg(x)S(1-y)Se(y) addresses in detail the structural and thermodynamic properties,[48] while a recent paper addresses effects of disorder on the optical gap.[49] Finally, first-principles studies of the structural properties of ZnSe-MgSe superlattices[50] do not include free-standing superlattices of composition other than 50%.

The theoretical paper by Saitta et al.[48] contains the only predictions we are aware of on the structural properties of $Zn_{1-x}Mg_xSe$ alloys. The authors evaluated the structural properties of (Zn,Mg)(S,Se) solid solutions by combining computational alchemy and cluster expansion

methods with Monte Carlo (MC) simulations. The main thrust of the paper was towards the determination of the phase diagram of the quaternary alloy. The equilibrium lattice parameter resulting from the MC simulations was found to depend almost linearly on composition. Exceedingly slight deviations from Vegard's law were obtained by a fitting procedure. Extrapolating their predictions to ZnMgSe ternary alloys, one would expect a parabolic dependence of the lattice constant on Mg concentration, leading to a bowing parameter b_a=-0.027 (atomic units), corresponding to b_a=-0.014 (Å).

Fig. 1 summarises the experimental concentration vs. lattice parameter dependence reported by the different above-mentioned groups for ZnMgSe. We emphasize that only Jobst et al. sampled the lattice dependence on Mg concentration over the whole concentration range and, for sake of comparison, we have extrapolated the data from the other groups to the whole compositional range, following the functional dependence reported by each group. Discrepancies are evident. For example a lattice parameter of 5.79Å would correspond to a Mg concentration varying from ~40% for Puls et al. to ~55% of Vögele et al., corresponding to differences of ~30% in the expected composition for a given lattice parameter. Discrepancies grow larger in the extrapolated high-x region in Fig. 1.

As detailed above the semiconductor bandgap has been evaluated by two groups at room temperature (Jobst et al. and Okuyama et al.) and by the others at low temperature (Puls et al., Wörz et al. and Vögele et al.). For the sake of comparison LT data have been extrapolated to room temperature and to the whole compositional range. Fig. 2 summarises the resulting experimental bandgap. For the temperature dependence of the bandgap of the alloys we used data measured in our lab in the 0-~35% range and extrapolated the whole compositional range. We stress that any possible uncertainty introduced by the LT to RT extrapolation procedure would be totally negligible for the purposes of our discussion. Discrepancies between the bandgap results from the different groups are evident. For example a RT gap of 3.2 eV would correspond to a Mg concentration varying from ~42% for Puls et al. to ~60% of Vögele et al., i.e., to differences of ~30% in the concentration at a given bandgap value.

In view of such discrepancies, we re-evaluated the electronic and structural properties of ZnMgSe using new experimental and theoretical evidence. Several $Zn_{1-x}Mg_xSe$ samples were grown by MBE and investigated, in situ, by x-ray photoemission spectroscopy, and ex situ by x-ray diffraction (XRD), photoluminescence (PL), optical absorption and Rutherford backscattering spectrometry (RBS), in collaboration with Prof. Drigo's group in Padova. Theoretical investigations were performed in collaboration with the group of Dr. M. Peressi at the University of Trieste using state-of-the-art ab-initio pseudopotential calculations.

3.2. Experimental details

$Zn_{1-x}Mg_xSe$ samples were grown by MBE on 1μm-thick GaAs(001) buffer layer. The buffer layer was As capped, air exposed and subsequently cleaved into several sections. Such wafer sections were used as substrates for the II-VI growth, after As desorption in the II-VI chamber to achieve the GaAs 2x4 surface reconstruction. $Zn_{1-x}Mg_xSe$ alloys were grown at 280^0 C, in Se-rich conditions and exhibited a 2x1 surface reconstruction during growth. The beam pressure ratio (BPR) between Zn and Se was kept in the 0.35-0.38 range. A 20 Å-thick ZnSe cap layer was deposited, on the samples which would have to be air-exposed for ex-situ experimental analysis with the goal of preventing surface oxidation.

Measurements of the samples lattice parameter ware carried out by XRD using a Philips high resolution x-ray diffractometer equipped with a Cu radiation source and a Bartels four-crystal Ge(220) monochromator,[51] providing Cu $K\alpha_1$ radiation (λ=0.154056 nm) with 12 arcsec angular divergence. Rocking curves were used to determine the difference between the lattice parameter of the layer and that of the substrate, a(GaAs)=5.65325 Å.[52] The lattice mismatch between substrate and epilayer was determined by measuring different symmetric (004) and asymmetric (224) reflections both at grazing incidence and grazing exit angle.[53] Samples examined ranged in thickness from 500 nm to more than 1 μm ($0<x<40\%$), all well beyond the critical thickness, and resulted in largely relaxed layers.[54] A small residual strain of the order of 0.2-0.3% was detected by XRD in the thickness range examined.[55] The residual strains could be reduced using higher growth temperatures (~330° C), but we elected to grow at relatively low temperatures because of

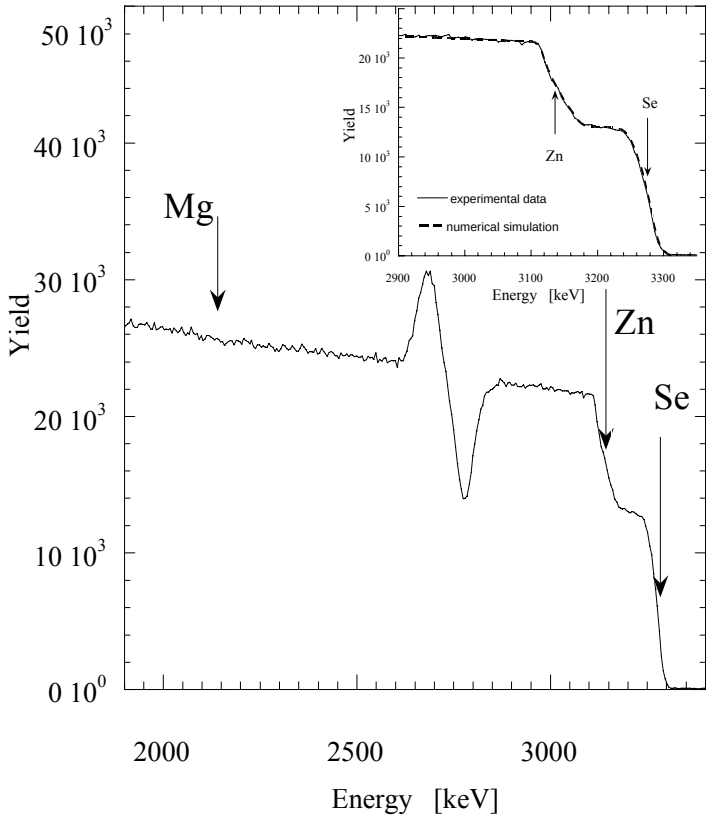

FIG. 3 Representative RBS spectrum of sample y283, whose RBS determined Mg concentration was 0.215. Zn, Mg and Se thresholds are indicated by arrows. The Zn/Se high ratio instead allows to directly evaluate the Zn relative content. Inset: the analysis of the spectra was actually performed by fitting the experimental data with numerically calculated spectra, considering geometrical factors and stopping power functions (see Ref. 62). The numerical data (dashed line) reproduce with remarkable accuracy the experimental points (continuous line). The overall statistical error due to the Poisson noise of the measurements is of about ±1 at %.

the improved optical quality of the layers. For example, PL linewidth was less than 20 meV at 280° C with x=0.25, and near 35 meV in samples grown above 310° C. Only negligible tilt (< 0.01°) was detected in both <110> and <1$\bar{1}$0> directions. For most of the samples a set of 12 reflections was measured to minimize statistical errors.[56]

Alloy composition and electronic properties were sampled in-situ by XPS, using the experimental apparatus described in Chapter 2.

For the evaluation of concentration by XPS, binary ZnSe and MgSe standards were grown by MBE in Se-rich conditions at 280° C. The BPR for ZnSe was 0.4. MgSe was grown with a Mg beam equivalent pressure of $3.5 \cdot 10^{-7}$ Torr and a Se beam equivalent pressure of $1.6 \cdot 10^{-6}$ Torr. The MgSe layer thickness was kept at about 0.07 μm to improve crystal quality. Relaxation was achieved by growing the MgSe layer on top of a 0.5 μm-thick lattice matched $Zn_{0.42}Cd_{0.58}Se$ buffer layer.[42,57] By normalising the emission from the Mg 2p and Zn 3d core levels from the two binary standards to the intensity of the Se 3d doublet, we derived the ratio of the elemental core sensitivity factors for the two cations S(Mg 2p)/S(Zn 3d). The average Mg concentration within the XPS sampling depth could then be determined from the following expression:

$$x = \frac{I(Mg\ 2p)}{I(Mg\ 2p) + I(Zn\ 3d) \cdot \left[\frac{S(Mg\ 2p)}{S(Zn\ 3d)} \right]}$$

We found S(Mg 2p)/S(Zn 3d)= 0.31±0.01. Since no attempt was made to compensate for possible variations in the analyzer throughput with kinetic energy, this value should be considered specific of the XPS spectrometer employed. However, the kinetic energy window involved is relatively narrow, so that we do not expect large variations in the analyzer throughput. Our experimental values can be compared with theoretical predictions based on Hartree-Fock-Slater calculations: S(Mg 2p)/S(Zn 3d)= 0.4, reported by Yeh et al.[58,59].

The $Zn_{1-x}Mg_xSe$ layers grown for the evaluation of concentration by RBS were fabricated on a 100nm ZnSe buffer layer and were 800nm thick. The RBS spectra where obtained at Legnaro National Laboratories, by using a 4 MeV He+ beam and a scattering angle of 170 degrees. The measurements were calibrated in solid angle against a Ta/Si standard samples whose absolute Ta content was known with an accuracy better than 2%.[60] Beam charge collection was performed by using the whole scattering chamber as a Faraday cup, reaching accuracy better than 1%.

As the RBS analysis does not take into account any channelling effect, care was taken to avoid any such effects in the measurement. For this purpose the random spectrum was accumulated while the sample was tilted 5 degrees from the [001] axis and azymuthally rotated. The random spectrum is a good approximation of the average of all the different channelling conditions.[61] The sample composition was derived from the relative intensity of the RBS signal

corresponding to Zn and Se. Analysis of the spectra was performed by fitting the experimental data to numerically calculated spectra, including geometrical factors and stopping power functions.[62] Fig. 3 shows a representative RBS spectrum of sample y283, whose RBS determined Mg concentration was 0,215. The 4 MeV beam energy allows to obtain a large separation between the two signals (Δ~140 keV). The Zn and Se thresholds are indicated in Fig. 3 by two arrows. The Mg signal (indicated by an arrow) was not taken into account being superimposed to a high background coming from the GaAs substrate. The Zn/Se high ratio instead allows to directly evaluate the Zn relative content eliminating any systematic error related to the collected beam charge and solid angle. In the inset of Fig. 3 the result of the spectrum simulation is shown together with the experimental data. The simulations (dashed line) reproduce with remarkable accuracy the experimental data in the energy range of interest (>2900 keV: continuous line). The overall statistical error due to the Poisson noise of the measurements was about ±1 at %.

The optical properties of $Zn_{1-x}Mg_xSe$ samples were investigated by means of photoluminescence (PL) and optical absorption spectroscopy. All measurements were performed at 15 K using a closed-cycle He refrigerator. For PL measurements, the 363 nm line from an Ar^+ ion laser was focused at normal incidence onto the sample surface. The PL emission was collected in a backscattering geometry along the growth direction and dispersed by a 0.05-nm resolution monochromator. For transmission measurements a 90W tungsten-halogen lamp was used as source. The samples were first glued face down on a sapphire holder and mechanically thinned down to about 50 μm. Circular areas of the III-V substrate -about $6x10^{-4}$ cm^2 in size- were selectively removed by photolithographic and wet-etching techniques. A Hg lamp operated at 350W (wavelength: 400nm) was used to expose for 15s the positive photoresist through a quartz mask with a transparent dot matrix. The selective etching solution was NaOH (2.5%): H_2O_2 (42:8). Mechanical damage to the structures was ruled out by comparing PL spectra recorded before and after substrate removal.

3.3. Theoretical results

Global structural and electronic properties of the ternary Zn(1-x)Mg(x)Se alloy as well as

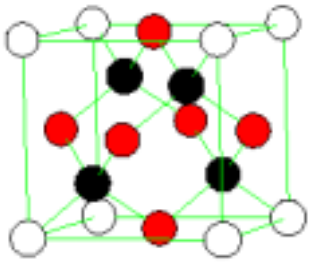

Luzonite

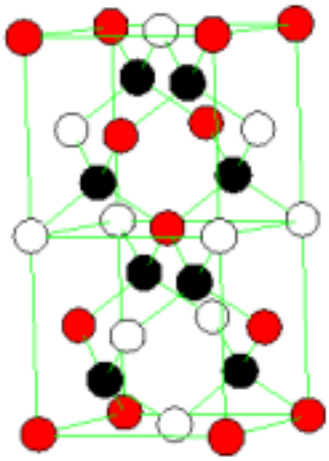

Chalcopyrite

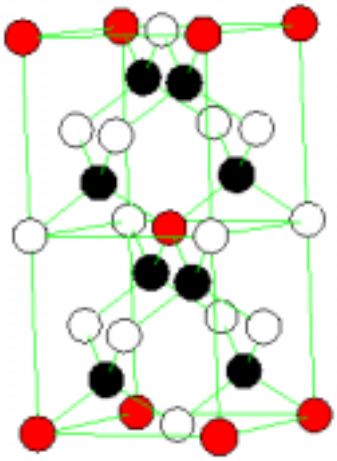

Famatinite

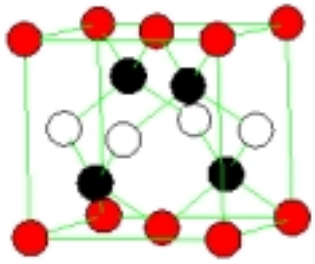

SL (001)

FIG. 4 The four different crystal structures considered for the theoretical analysis are shown. Anions are depicted in black, while the two cations are in white and grey.

their atomic-scale features were investigated using a state-of-the-art ab-initio pseudopotential approach based on a direct supercell description. More precisely, the theoretical effort was addressed to the study of the average lattice parameters, of the nearest-neighbour (NN) bond lengths and of the total density of occupied states

The pseudopotentials used were found to well reproduce the equilibrium experimental lattice parameter and bulk modulus of the binary compounds. For example, equilibrium theoretical lattice constants of 5.59, 5.91, and 6.10 Å were obtained for cubic ZnSe, MgSe, and CdSe respectively. The ternary alloys were modelled at selected compositions corresponding to well defined stoichiometries with "ordered" structures whose symmetry group is a zincblende subgroup, allowing for internal distortions. This can be done with limited computational effort (i.e., with few atoms per unit cell) for compositions x=0.25, 0.50, 0.75. For the structures considered, which are described by periodically repeated supercells, a structural optimization minimizing the total energy with respect to the cell parameters and to the atomic positions was performed. This provides not only the average lattice parameter of the alloy but also the individual anion-cation bond lengths. The calculations are performed with a kinetic energy cutoff of 16 Ry and using in the self-consistent cycle a Brillouin zone sampling of 6 special points in the irreducible wedge for the zincblende structure, and sets giving a comparable accuracy for the other structures.

For the compositions x=0.25 and x=0.75 the simplest structure is a 8-atom simple cubic cell (Luzonite, see Fig. 4), where the cations with lower concentration form a regular simple cubic lattice. Another simple structure that can be considered for the same composition is the Famatinite (see Fig. 4), with 16 atoms in the primitive unit cell and where the "minority" cations form a body-centered tetragonal lattice. In this structure, because of symmetry, the bonds can be of two slightly different lengths for each type of anion-cation pair.

For the composition x=0.5, the smallest ordered structure is a 4-atom tetragonal cell, corresponding to the (ZnSe)(MgSe) (001) [or equivalently (110)] superlattice (see Fig. 4). Such a structure is strongly anisotropic, and thus not very suitable for simulating random alloys which are macroscopically isotropic. We considered, therefore, also the Chalcopyrite structure, which is described by a 16-atom tetragonal cell (see Fig. 4).

If, in the evaluation of the nearest-neighbour bond lengths, the results obtained for these compositions could suffer for the small size of the supercells chosen, which does not allow full internal lattice relaxations, those derived for the cases of extreme dilutions ($x \rightarrow 0$ and $x \rightarrow 1$) are more meaningful. To this aim, a 32-atoms BCC supercell with only one substitutional impurity, i.e. x=1/16 (or the complementary case x=15/16) was considered. Among the shells of ions

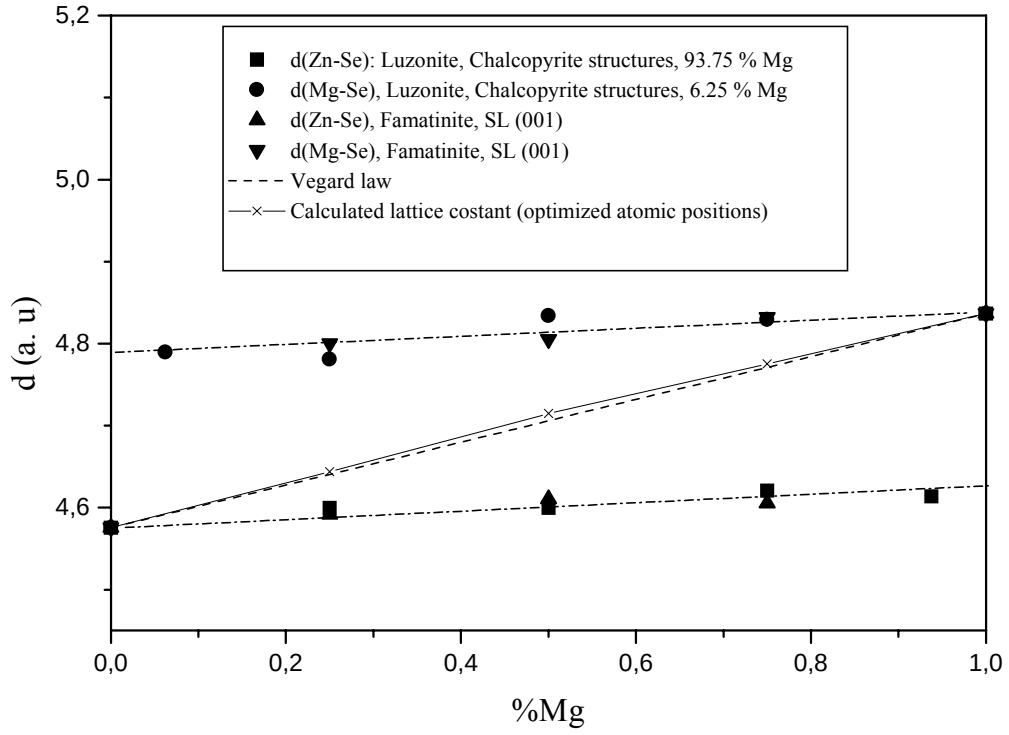

FIG. 5 Average interatomic and NN distances in atomic units (a.u.) as a function of Mg concentration. For the NN distances results of different supercells structures for the same composition are shown. Solid squares, d(Zn-Se) obtained from the following superstructures-concentration pairing:(Luzonite,0.25%), (Chalcopyrite,0.50%), (Luzonite,0.75% Mg), (32-atoms BCC supercells,93.75% Mg); solid circles, d(Mg-Se) obtained from the following pairing: (32-atoms BCC supercells,6.25% Mg),(Luzonite,0.25%), (Chalcopyrite,0.50%), (Luzonite,0.75% Mg)]. For comparison results obtained with different structures are also shown. Upwards pointing triangles, d(Zn-Se) obtained from: (Famatinite,0.25%), (SL (001),0.50%), (Famatinite,0.75% Mg); Downwards pointing triangles, d(Mg-Se) obtained from: (Famatinite,0.25%), (SL (001),0.50%), (Famatinite,0.75% Mg). The relaxed lattice parameter shown is that derived from the Luzonite supercell (0.25%, 0.75% Mg) and the Chalcopyrite (0.50% Mg) supercell. Vegard's law dependence is shown for comparison. The relation between the interatomic distance (d) and the lattice parameter (a) is given by: $d=a\cdot\sqrt{3}/4$.

surrounding the substitutional impurity, in fact, only the first shell shows significant distortions, whereas the second and the third one are already only slightly distorted, thus indicating that the size of this cell is large enough.

On the optimized structure density of states calculations (DOS) were performed. The numerical accuracy of these theoretical results can be pushed to a very high level without much effort, and depends on the kinetic energy cutoff used for the size of the plane-wave basis set and on the accuracy of the Brillouin zone sampling. With the technical parameters used in the calculations (kinetic energy cutoff, special points for the self-consistency, points for the band-structure non-self-consistent calculations), DOS with a numerical resolution of 0.1 eV were obtained. An uncertainty much larger than the numerical one comes from the use of the density-functional theory in the local-density approximation (DFT-LDA), and from the non-relativistic (i.e. spin-averaged) approach.[63]

Other structures could be chosen, following different criteria as proposed in Ref. 64, 65 and 66,[64,65,66] with the aim of better simulating the randomness of the alloy and to obtain better statistics about the nearest neighbours (NN) bond length distribution. This more detailed investigation is beyond the present purposes. The theoretical choices have only been tested considering few other structures, checking that the results for the DOS do not change appreciably within the resolution required.

In Fig. 5 we summarize the calculated structural parameters of the alloys. The average interatomic and NN distances in atomic units (a.u.) are shown as a function of Mg concentration. For the NN distances results of different supercells structures for the same composition are shown for comparison. Same symbols are used, for both the two distinct cation-anion bond lengths, for the following two superstructure-concentration pairing sets: {Luzonite-0.25%, Chalcopyrite-0.50%, Luzonite-0.75% Mg, 32-atoms BCC supercells-(93.75% or 6.25% Mg)} and {Famatinite-0.25%, SL (001)-0.50%, Famatinite-0.75% Mg}. The relaxed lattice parameter shown is a parabolic fit derived from 5 points, i.e., the Luzonite supercells (0.25%, 0.75% Mg) and the Chalcopyrite (0.50% Mg) supercell, and the two binary theoretical lattice parameters. Vegard's law dependence is shown for comparison. The relation between the interatomic distance (d) and the lattice parameter (a) is given by: $d=a\cdot\sqrt{3}/4$.

The calculated average lattice parameter is very close to the Vegard's prediction, with a small positive bowing: $a_0(x)= a_0(MgSe)*x + a_0(ZnSe)*(1-x) - 0.06*x(x-1)$ (in atomic units, while

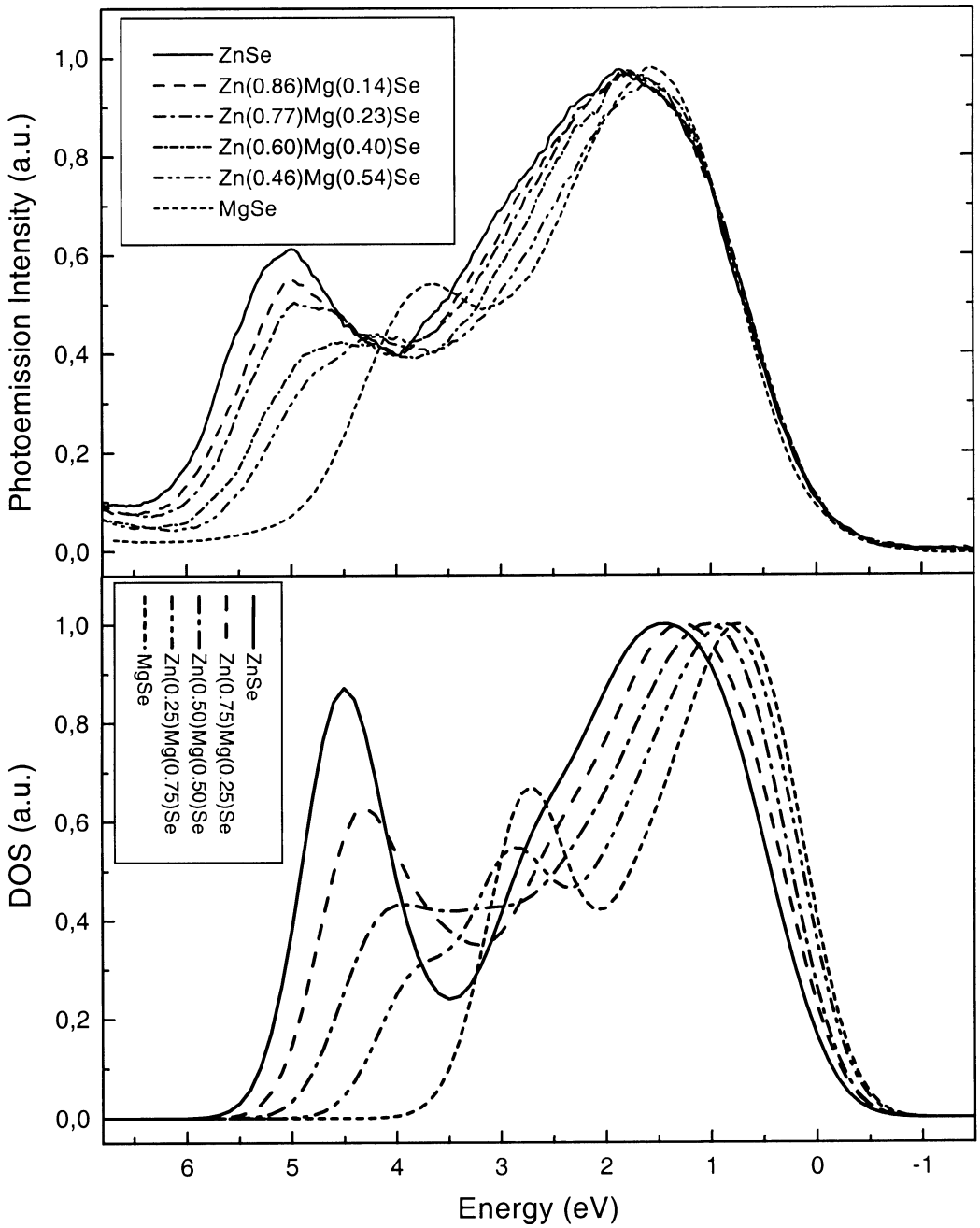

FIG. 6 (bottom) Theoretical DOS curves. Theoretical data (numerical resolution of 0.1 eV) have been convoluted with Gaussian function (FWHM=0.8 eV) in order to facilitate comparison with experimental EDCs. The spectra have been aligned to the top of valence band, corresponding to the zero of the scale. (top) Experimental EDCs of valence band emission for ZnSe, MgSe and several ZnMgSe alloys (14, 23, 40 and 50% Mg). The Mg concentrations reported have been measured by XPS. Spectra have been aligned to the linearly extrapolated valence band maximum, which was used as the zero of the energy scale (binding energy).

b=-0.03 if expressed in Å). We emphasize that the estimate of the bowing parameter is affected by a relatively large uncertainty, depending on which supercell structures are considered. A bimodal distribution of the NN distances was found, as typically observed in other ternary ionic and semiconducting alloys. The variation of the NN distances as a function of the alloy composition is usually gauged by the ratio: $\eta(x)= \{d[Mg-Se](x)-d[Zn-Se](x)\}/\{d[Mg-Se](1)-d[Zn-Se](0)\}$ where d[Mg-Se](1) and d[Zn-Se](0) are the bulk values. The value $\eta=0$ would indicate that the lattice is undistorted and that the NN distances have the common value predicted by the Vegard's law, whereas $\eta=1$ would describe the case in which the NN distances conserve the values observed in the parent binaries. Since d[Mg-Se](x) and d[Zn-Se](x) have a similar linear behaviour, η is almost constant and predicted from the calculations to be 0.82, a value which is typically observed in covalent alloys.

The calculated DOS curves obtained on the basis of the structural optimisation are presented in Fig. 6 (bottom). The results (numerical resolution of 0.1 eV) have been convoluted with Gaussian function (FWHM=0.8 eV) in order to facilitate a subsequent comparison with experimental energy distribution curves (EDCs). All the spectra have been aligned to the top of valence band, corresponding to the zero of the scale. The two major DOS features reflect mainly a Se 4p-derived structure in the 0-2 eV range, and Se p-cation s hybrid levels in the 2-5 eV range.[67] A clear general trend towards a reduction in the overall width of the DOS, of the order of 30%, when going from ZnSe to MgSe is found. The trend has a nearly linear behaviour with concentration. At high Mg concentration a broadening of the feature arising from the cation-anion states hybridisation is predicted.[67] When the alloy with 75% Mg is considered two clear features can be distinguished in that region, corresponding to a superposition of Zn- and Mg-related features. The Zn-related peak then disappears when MgSe is considered.

3.4. Experimental results

The electronic structure of $Zn_{1-x}Mg_xSe$ alloys were probed by photoemission (XPS). Fig. 6 (top) shows the measured valence band emission from the binary ZnSe, from the MgSe parent compound, and from ternary alloys with 14, 23, 40 and 50% Mg in the alloy. All the spectra were aligned to the linearly extrapolated valence band maximum, which was used as the zero of the energy scale. The theoretical DOS are found to capture the essential trends in the experimental data. The two major features, Se 4p-derived structure at low binding energies and Se p-cation s

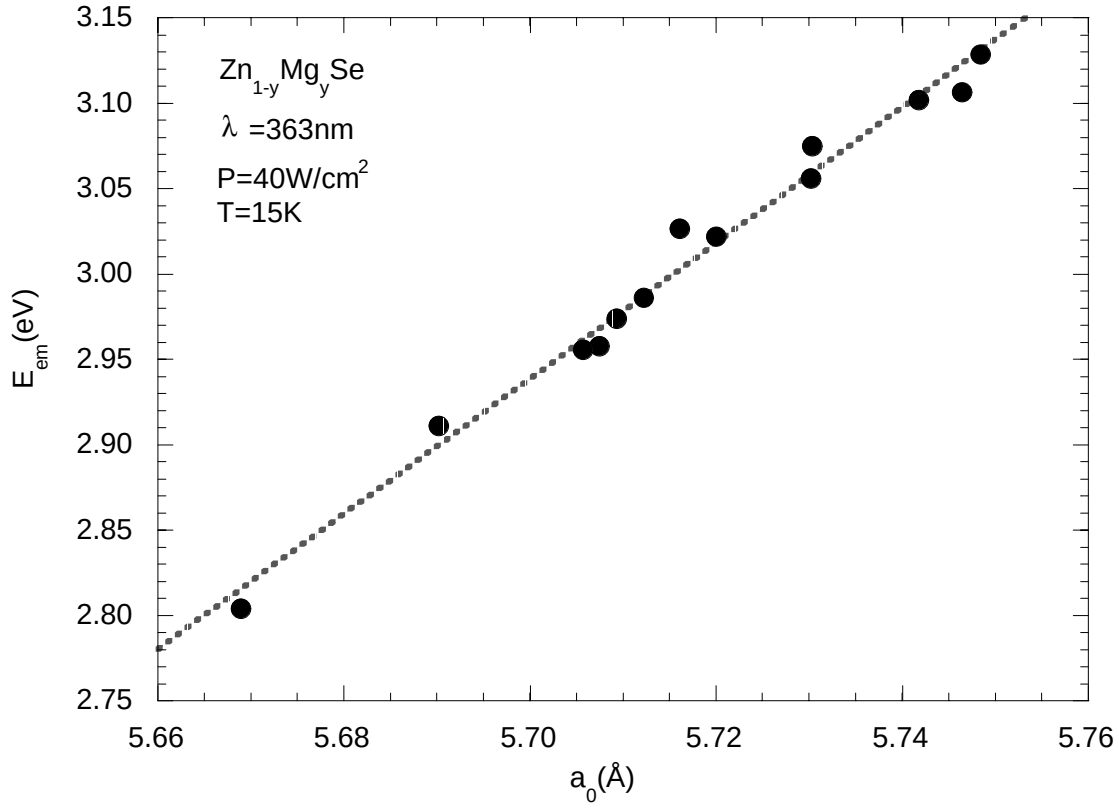

FIG. 7 Exciton peak emission dependence at 15 K for $Zn_{1-x}Mg_xSe$ alloys (solid circles). A dotted line through the data shows a linear fit using the following expression: $E_{Em}(eV)$= -19.671+3.9666x, where x is the lattice constant expressed in Å.

hybrid levels features at higher binding energies,[67] are clearly distinguishable. The trend towards a reduction of the overall width of the measured EDC when going from ZnSe to MgSe, of the order of 25% for the experimental data, is confirmed. At higher Mg concentration the same broadening arising from the cation-anion states hybridisation due to the superposition of Zn and Mg related states can be observed in the experimental and theoretical results.

We monitored, in the low Mg concentration range of interest, the free-exciton emission at 15 K as a function of the alloy composition. Fig. 7 shows the resulting experimental dependence (solid circles). A dotted line through the data shows the result of a linear fit to the data using the following expression: E_{Em} (eV)= -19.671+3.9666x, where x is the lattice constant expressed in Å.

Among the samples analyzed in Fig. 7, six were also characterized by means of room

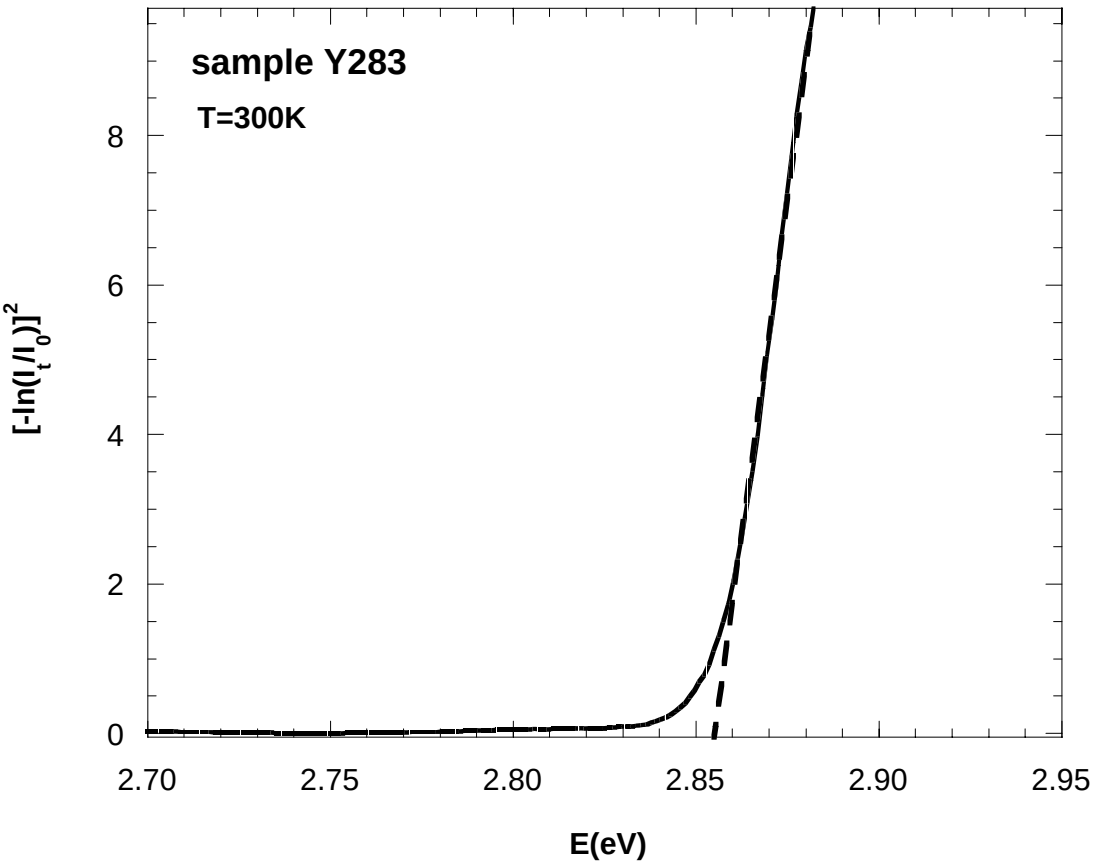

FIG. 8 RT plot of $\alpha^2 \cdot d^2 = [-\ln(I_t / I_0)]^2$ versus photon energy, where α is the absorption coefficient, d the sample thickness, I_0 the incident light intensity, and I_t the transmitted light intensity. The linear extrapolation (dashed line) to $\alpha^2 \cdot d^2 = 0$ of the absorption edge allowed us to determine the bandgap value.

temperature optical absorption. This was enough to determine the RT dependence of the bandgap on the lattice parameter and on the concentration. For example, we show in Fig. 8 a plot of $\alpha^2 \cdot d^2 = [-\ln(I_t / I_0)]^2$ as a function of photon energy, where α is the absorption coefficient, d the sample thickness, I_0 the incident light intensity, and I_t the transmitted light intensity for sample y283. The linear extrapolation of the absorption edge was used to determine the bandgap value.[68] The measured room temperature bandgap of these samples, together with the low temperature exciton peak position allowed us to estimate the LT-RT bandgap variation for alloys with lattice constant below about ~5.76Å.[69] The functional dependence we found was: $E_{15K}(eV)-E_{RT}(eV)= -1.1+0.21778*x$, where x is the lattice constant expressed in Ångström.[70]

Fig. 9 shows the RT bandgap for our samples (solid squares), together with previously published results, as a function of the measured lattice parameter. Published LT measurements of

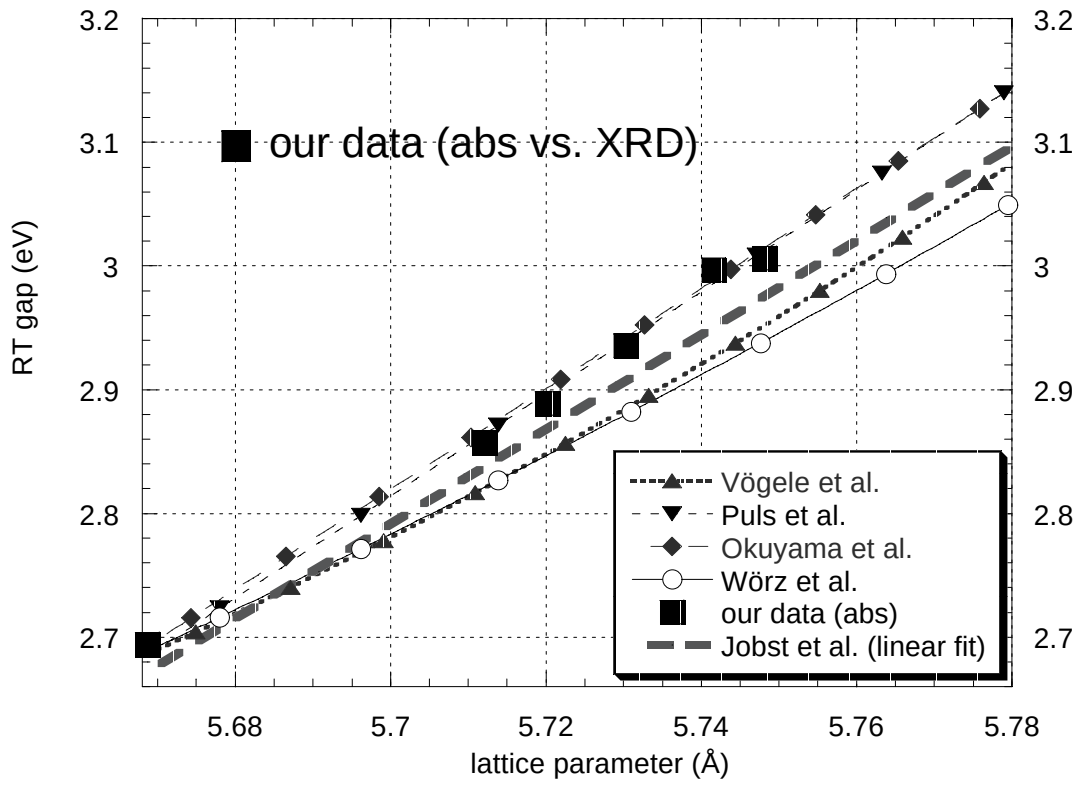

FIG. 9 RT gap vs. lattice constant for selected samples. Our results have been superimposed on previously published results. LT published measurements of the gap dependence on lattice constant have been shifted to RT, and data by Jobst et al. have been linearly fitted in the lattice parameter range shown in the figure (see also Ref. 71).

the gap dependence on lattice constant have been extrapolated to RT, and data by Jobst et al. have been linearly fitted in the lattice parameter range shown in Fig. 9.[71] The expected uncertainty on the bandgap determination is only of the order of few tens of meV. For example the room temperature gap of ZnSe has been in the recent past measured by different groups, which reported values ranging from 2.68 to 2.71, as a result of the different experimental techniques employed.[43] Our data in Fig. 9, which are in remarkable agreement with data by Okuyama et al. and by Puls et al., exhibit differences when compared to those reported by Wörz et al. and Vögele et al. For example, considering a given lattice parameter of 5.74Å, the range of bandgap value reported goes from ~2.91 eV to ~2.98 eV, i.e. 70 meV, and corresponds to differences of few percents in the bandgap at a given lattice parameter. These limited discrepancies should be compared to the 30% scatter in Fig. 2 (and in Fig.1). Clearly, most of the discrepancies in Fig. 2 are due to uncertainties in the determination of the sample composition, as opposed the bandgap. This was our major motivation in determining the composition of our samples with two totally independent methods, such as XPS and RBS. Moreover, the two techniques have different surface sensitivities, and this is of paramount importance when probing alloys which may exhibit surface segregation phenomena. The electron escape depth in a solid is known to follow a nearly "universal" trend as a function of the kinetic energy, which predicts an escape depth minimum of ~ 5Å somewhere in the 60-90 eV range.[72] The escape depth for electrons from the Mg 2p and Zn 3d core levels excited by Al Kα radiation is of the order of ~15Å.[73] This means that the overall sample thickness probed by XPS is less than 50Å. On the other hand RBS is a relatively bulk sensitive technique, sampling several thousands Ångströms of the sample.[74]

Fig. 10 shows the results of the XPS and RBS determination of the sample composition. The XRD-determined alloy lattice parameter is plotted as a function of the sample composition as determined by RBS (solid circles) and XPS (open squares). We also show, for comparison published results by other authors. Our XPS and RBS results agree within the quoted 1% experimental uncertainty, supporting the accuracy of our composition determination and the absence of surface segregation. Discrepancies with earlier results are instead quite substantial in Fig. 10, with our data occupying the middle range of the wide distribution of literature results. Data reported by Okuyama et al., Puls et al. and Jobst et al. have all been obtained by means of

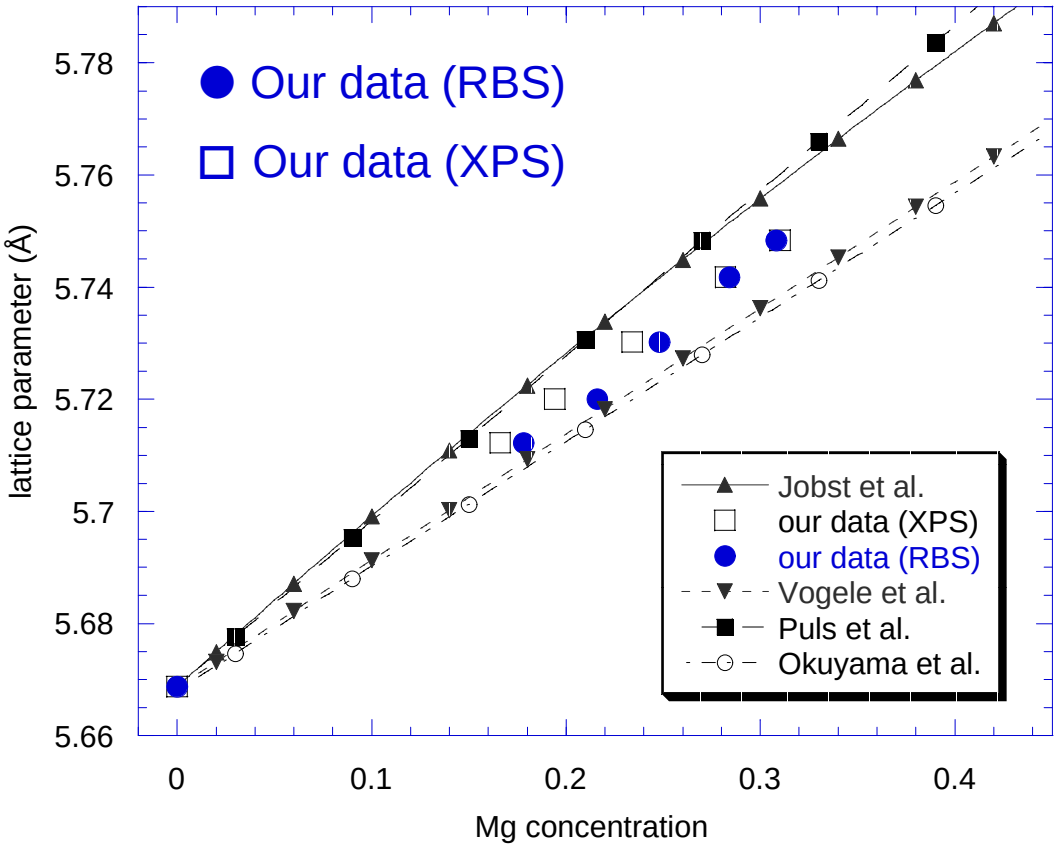

*FIG. 10 Joint XPS-RBS concentration analysis vs. lattice parameter. Data are compared to previously published results. XPS and RBS concentration evaluations agree within the 1% error quoted. The agreement of the two techniques rules out the possibility of surface segregation in our samples. A linear fit to RBS data yields: y=5.6687+0.25172*x, where x is the Mg concentration and y the lattice parameter expressed in Ångström. Using, in addition, the reported lattice parameter of MgSe by Lunz et al.[44] the best fit is a parabolic one, with a bowing parameter of -0.02 using the RBS data (-0.03 by XPS).*

electron microprobe analysis. We suggest that the scatter between different data sets, and the discrepancy with our consistent RBS and XPS results might reflect differences in the calibration and background subtraction procedures employed by the different authors during electron microbe analysis.

Our data in Fig. 10 are consistent with either no bowing, or with a bowing sensibly smaller than previously reported. A linear fit to our data (RBS) would yield:

$a(Zn_{1-x}Mg_xSe)=5.6687+0.25172*x$.

By including the lattice parameter reported by Lunz et al.[44] for MgSe, a best fit is obtained with the following parabolic expression:

$a(Zn_{1-x}Mg_xSe)=5.6687+[0.2353-b_a]x+b_ax^2$

with bowing parameter b_a=-0.02, if using the RBS data, or b_a=-0.03 if using the XPS results. Such values are only about a third as large as that reported (-0.07) by Jobst et al.[36], and are in remarkable agreement with the theoretical predictions (b_a=-0.03).

3.5. Conclusions

We re-evaluated the electronic and structural properties of $Zn_{1-x}Mg_xSe$ alloys using new experimental and theoretical results. All expected alloy trends in the electronic density of states, including the progressive, 30% reduction in the valence band width with increasing Mg content, were borne out by our results. First principle calculations predict only a reduced bowing in the composition dependence of the alloy lattice parameter. Our new experimental results confirm that only a reduced bowing, if any, is present, with a bowing parameter b_a which does not exceed –0.03. Comparison with previously published results suggest that existing discrepancies in the literature are likely to reflect systematic uncertainties in the calibration and data analysis procedures employed during electron microprobe analysis of the sample composition.

ACKNOWLEDGEMENTS

We gratefully thank S. de Gironcoli for the calculation of MgSe elastic constants.

Chapter four: Lattice-matched heterojunctions

4.1. Introduction

$Zn_{1-y}Mg_ySe$ alloys can be grown lattice matched to $Zn_{1-x}Cd_xSe$ and potentially serve as barrier layers in strain-free emitters. Little information is available, however, on the properties of the corresponding interfaces, which will have a crucial role in determining device performance.

We present here a combined experimental and theoretical investigation of (001)-oriented interfaces between $Zn_{1-y}Mg_ySe$ and $Zn_{1-x}Cd_xSe$ alloys. Lattice-matched heterostructures were fabricated, by means of molecular beam epitaxy (MBE), at selected compositions and examined using monochromatic x-ray photoemission spectroscopy (XPS) and high resolution x-ray diffraction (XRD). Theoretical predictions were obtained in collaboration with Dr. M. Peressi of the University of Trieste. Both the band alignment and the composition-dependence of the alloy lattice parameter were derived from *ab-initio* pseudopotential calculations.

Experimental results were obtained from six types of lattice-matched heterojunctions, i.e., $Zn_{0.85}Mg_{0.15}Se/Zn_{0.90}Cd_{0.10}Se$ (a_0=5.71 Å), $Zn_{0.74}Mg_{0.26}Se/Zn_{0.85}Cd_{0.15}Se$ (a_0=5.73 Å), $MgSe/Zn_{0.42}Cd_{0.58}Se$ (a_0=5.904 Å), and the corresponding interfaces obtained through the reverse growth sequence. We use here the convention that an A/B heterostructure is fabricated by growing overlayer A on substrate B. All heterostructures were fabricated on GaAs (001) buffers. A 0.5 μm-thick, undoped (001) 2x4 GaAs buffer layer was initially grown in the III-V MBE chamber at 600°C on the GaAs(001) wafers after thermal removal of the oxide. The GaAs layer was either As capped, as described in Chapter 2, or directly transferred to the II-VI MBE chamber. Undoped II-VI epilayers, were grown in Se-rich conditions, as confirmed by the 2x1 reconstruction in the reflection high energy electron diffraction (RHEED) pattern. II-VI growth temperatures were in the 250 to 280°C range. The II-VI overlayer growth mode was layer-by-layer in all cases, as indicated by RHEED.

The thickness of the first II-VI epilayer grown on GaAs (typically 0.5 to 1.0 μm-thick) was selected in order to achieve lattice relaxation, through formation of a misfit dislocation network at the II-VI/III-V interface. The XRD-determined residual strain at the surface was below 0.2-0.3% for $Zn_{1-y}Mg_ySe$ layers, but also $Zn_{1-x}Cd_xSe$ alloys showed a non total relaxation of the same order. Such a residual strain is totally negligible for the purposes of valence band alignment determination by XPS. The thickness of the binary MgSe layer was kept at about 0.07 μm in all cases, to improve crystal quality. Relaxation was achieved by growing the MgSe layer on top of a 0.5 μm-thick $Zn_{0.42}Cd_{0.58}Se$ buffer layer. To complete the heterojunction for band offset studies, the desired II-VI overlayer was then grown in the form of an undoped thin film, typically 2 to 4 nm-thick.

The maximum lattice mismatch which was observed by XRD as a result of unintentional variations in the alloy composition was of the order of ~0.1-0.2 %, i.e., effectively negligible for the purpose of the present work. Throughout this chapter the quoted alloy compositions for $Zn_{1-y}Mg_ySe$ are derived from the consistent XPS (and RBS) determinations described in Chapter 3, and the quoted lattice parameters from our own XRD studies of the same samples. The quoted alloy compositions for $Zn_{1-x}Cd_xSe$ layers have been determined by XRD as Vegard's law holds. We did not, however, give up the possibility of monitoring in situ the concentration of $Zn_{1-x}Cd_xSe$ layers by XPS. Also for such materials a good agreement was found between the XPS determination of the concentration and the XRD measurements.[57] The required XPS cross-sections for the Mg 2p, Cd 3d and Zn 3d and Zn 2p core levels were determined empirically from XPS studies of binary MgSe, CdSe and ZnSe epitaxial standards, as already explained in Chapter 3 in the special case of Mg containing layers. In the case of ZnCdSe we found S(Cd 3d)/S(Zn 2p)=0.86±0.03, i.e., relatively close to predictions based on Hartree-Fock-Slater calculations by Yeh et al.[58], who reported: S(Cd 3p)/S(Zn 2p)= 0.7. We used the Zn 2p core levels rather than the Zn 3d levels due to the partial superposition of the Zn 3d with the Cd 4d levels, which complicates extraction of the different contributions from the two cations.

4.2. Interface quality

We monitored the lineshape and integrated intensity of substrate and overlayer core levels as a function of overlayer thickness to probe the different heterojunctions for atomic interdiffusion. For example, we show in Fig. 1 the integrated intensities of the Cd 3d and Mg 2p core emission from the six types of heterojunctions examined as a function of overlayer thickness. The latter was calculated from our growth rate calibration. For substrate and overlayer core levels we plot in a logarithmic scale $I_{cl}(\vartheta)/I_{cl}^{0}$ and $1-\left[I_{cl}(\vartheta)/I_{cl}^{\infty}\right]$, respectively, where I denotes the

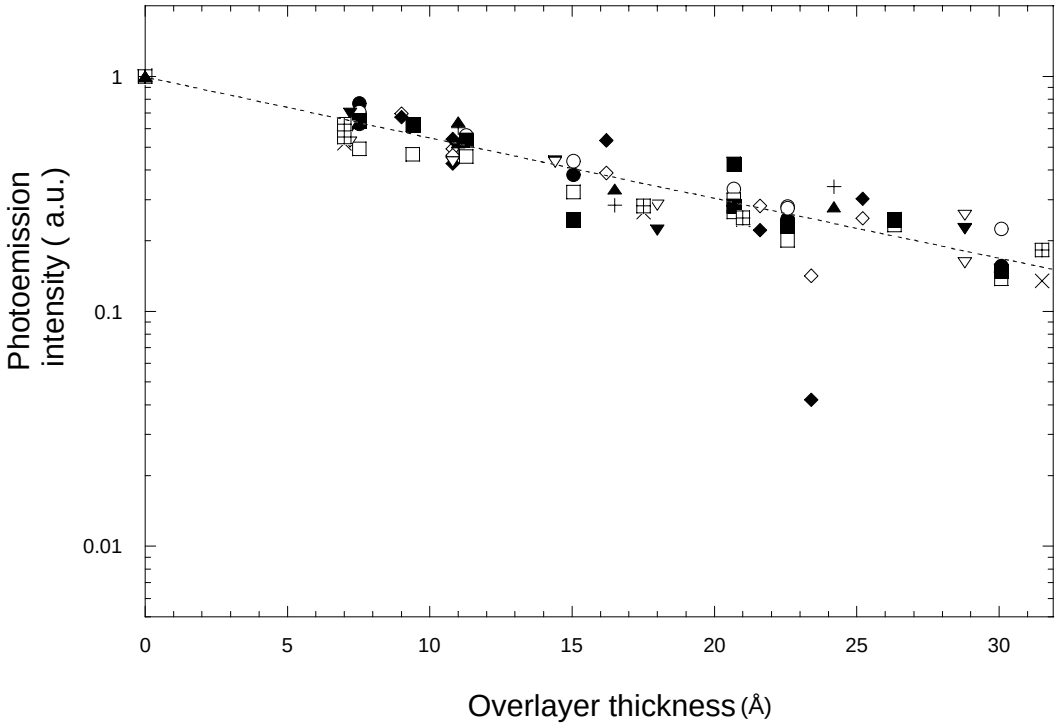

FIG. 1 Integrated intensities of the Cd 3d and Mg 2p core emission from six types of heterojunctions between $Zn_{1-y}Mg_ySe$ and $Zn_{1-x}Cd_xSe$ semiconductors as a function of overlayer thickness θ. For substrate and overlayer core levels we plot in a logarithmic scale $I_{cl}(\vartheta)/I_{cl}^{0}$ and $1-\left[I_{cl}(\vartheta)/I_{cl}^{\infty}\right]$, respectively, where I *denotes the integrated core emission intensity after background subtraction, the subscript* cl *specifies the core level under consideration (Cd or Mg), and the superscript denotes the initial substrate emission prior to overlayer deposition or the thick-coverage limit of the core emission from the overlayer. The dotted line depicts the expected, ideal behaviour for layer-by-layer growth in the absence of interdiffusion. Different symbols denote different alloy compositions and growth sequences: ◊/◆ substrate (x=0.1) Cd/overlayer (y=0.15) Mg emission; ▼/∇ substrate (y=0.15) Mg/overlayer (x=0.10) Cd emission □/■ substrate (x=0.15) Cd/overlayer (y=0.26) Mg emission; ●/○ substrate (y=0.26) Mg/Cd overlayer (x=0.15) emission;* X/+ *substrate (x=0.58) Cd/overlayer (y=1) Mg emission; ▲/+ substrate (y=1) Mg/overlayer (x=0.58) Cd emission.*

integrated core emission intensity after background subtraction, the subscript *cl* specifies the core level under consideration (Cd or Mg), and the superscript denotes the initial substrate emission prior to overlayer deposition or the thick-coverage limit of the core emission from the overlayer. The dotted line with slope corresponding to the photoelectron escape depth (~15 Å in our experimental conditions)[73] depicts the expected, ideal behaviour for layer-by-layer growth in the absence of interdiffusion. The core intensities were consistent with the ideal behaviour within the XPS experimental uncertainty of about ±1%. The lineshape of the different core levels (not shown) exhibited no evidence of major chemically-shifted contributions.

The implication of this, and of the results of Fig. 1, is that the heterojunctions considered grow in a layer-by-layer mode, with no evidence of atomic interdiffusion and/or interface reaction products within the experimental uncertainty.

4.3. Band alignment

4.3.1 Measuring band offsets by photoemission

Two methods are typically used to estimate valence band offsets at semiconductor heterojunctions by XPS. The first method, illustrated in Fig. 2, involves measuring directly the two valence band maxima of the two semiconductor constituents near the interface. In Fig. 2 we schematically show the valence band emission expected when a thin layer of semiconductor A is grown onto a semiconductor B. The double-edged emission structure in Fig. 2 includes features of both semiconductors. The two valence band maxima are obtained through a least squares linear extrapolation of the corresponding valence band edges. The energy difference of the two valence band maxima gives directly the valence band offset ΔE_v. This method is often difficult to apply because of the need of distinguishing between the two valence-band contributions, even when the valence-band offset happens to be larger than the experimental energy resolution. We actually could not use this method to the determination of the band alignment in any of the junctions investigated, both in the case A/B or B/A, as the superposition of valence band contributions from the two layers unfortunately hindered the extraction of two clear valence band edges.

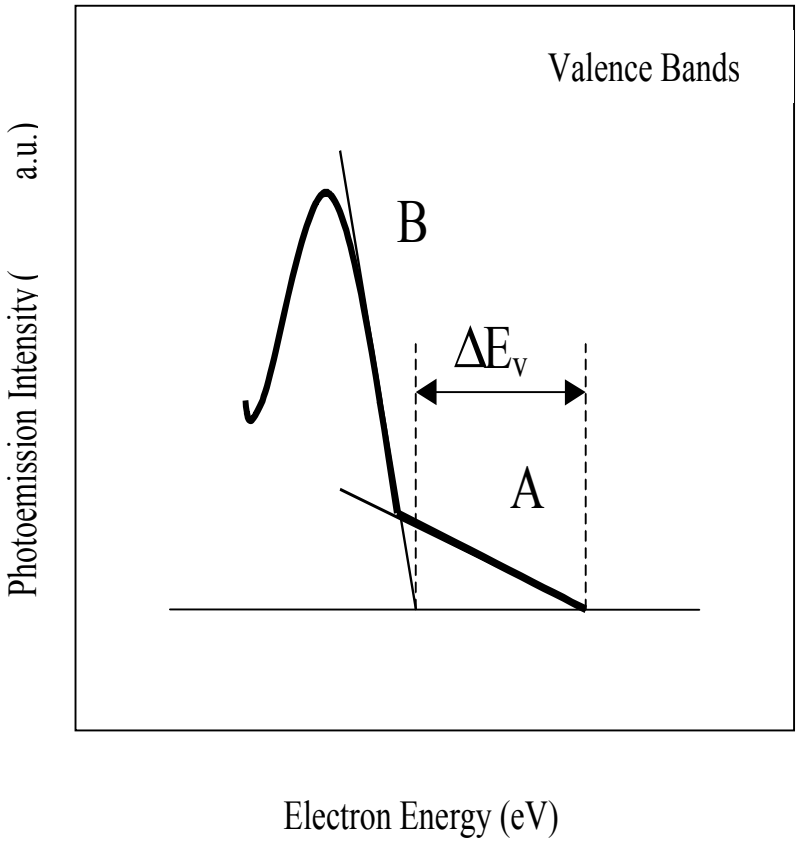

FIG. 2 Representative valence band emission from a thin layer of semiconductor A onto semiconductor B (A/B). The double-edged emission structure in fig. includes features of both semiconductors. The two valence band maxima are obtained through a least squares linear extrapolation of the corresponding valence band edges. The energy difference of the two valence band maxima gives directly the valence band offset ΔE_v.

The second method extracts ΔE_v from the energy separation of substrate and overlayer core levels across the interface, and does not have the limitations of the first method. In Fig. 3 we show a schematic band diagram of a heterojunction between two semiconductors A and B. The flat band approximation shown in Fig. 3 is justified when the experimental sampling depth is much smaller than the Debye length of either semiconductor. In the presence of sufficiently high doping of one or both of the two semiconductors, corrections may have to be implemented for band bending. $E_C(A)$ and $E_C(B)$ in Fig. 3 are the conduction band minima in the two semiconductors, $E_V(A)$ and $E_V(B)$ the valence band maxima, and $E_{cl}(A)$ and $E_{cl}(B)$ two representative core levels of semiconductors A and B. Inspecting Fig. 3 reveals that the valence band offset ΔE_v can be obtained from:

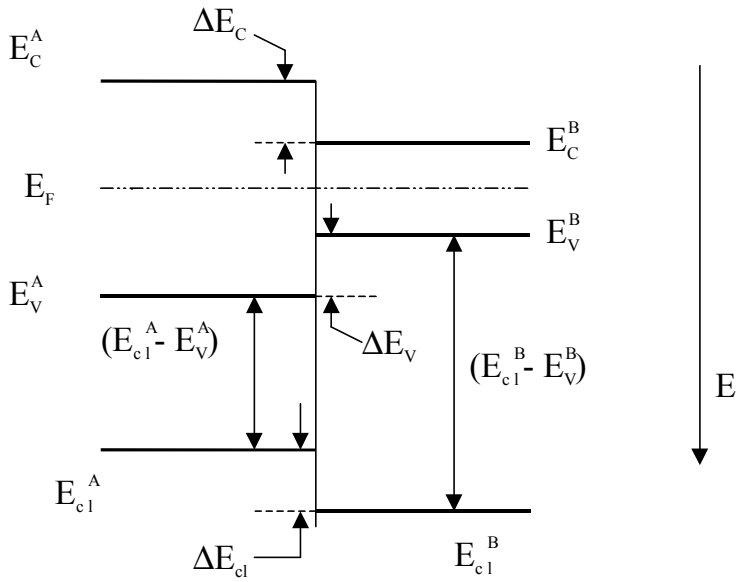

FIG. 3 Band diagram of a heterojunction between two semiconductors A and B in the flat band approximation. $E_C(A)$ and $E_C(B)$ are the conduction band minima, $E_V(A)$ and $E_V(B)$ the valence band maxima and $E_{cl}(A)$ and $E_{cl}(B)$ are two representative core levels of the semiconductors, respectively, A and B. The valence band offset ΔE_v can be obtained from: $\Delta E_V(A/B)=[E_{cl}(B)-E_v(B)]-[E_{cl}(A)-E_v(A)]+\Delta E_{cl}(A/B)$ where $\Delta E_{cl}(A/B)=[E_{cl}(A)-E_{cl}(B)]$ is the apparent energy separation between the substrate and overlayer core levels measured at the interface by photoemission. $[E_{cl}(B)-E_v(B)]$ and $[E_{cl}(A)-E_v(A)]$ are the binding energies of the core levels relative to the corresponding valence band

$$\Delta E_V(A/B)=[E_{cl}(B)-E_v(B)]-[E_{cl}(A)-E_v(A)]+\Delta E_{cl}(A/B) \quad (4.1)$$

where $\Delta E_{cl}(A/B)=[E_{cl}(A)-E_{cl}(B)]$ is the apparent energy separation between the overlayer and substrate core levels measured at the interface by photoemission. In Eq. 4.1 $[E_{cl}(B)-E_v(B)]$ and $[E_{cl}(A)-E_v(A)]$ are the binding energies of the core levels relative to the corresponding valence band maxima. Under the reasonable assumption that $(E_{cl}-E_v)$ is a bulk parameter that does not change when the interface is formed (in the absence of strain and interface reaction products), $[E_{cl}(B)-E_v(B)]$ and $[E_{cl}(A)-E_v(A)]$ can be determined a priori from the respective bulk materials. The uncertainty in the numerical determination of the offset derives mostly from the uncertainty in the determination of the position of the valence-band maximum relative to the Fermi level for each bulk material. The position of E_v is usually determined either from a linear extrapolation of the leading valence band edge,[75] or through a least squares fit of the data[76] to a suitable broadened

theoretical electronic density of states (DOS) near E_v. Although the linear extrapolation is in principle less accurate, it is likely to be adequate for deriving the valence-band offset for common anion systems such as AlAs-GaAs,[77] due to the cancellation of systematic errors that follows from the similarity of the anion-derived DOS features.[78]

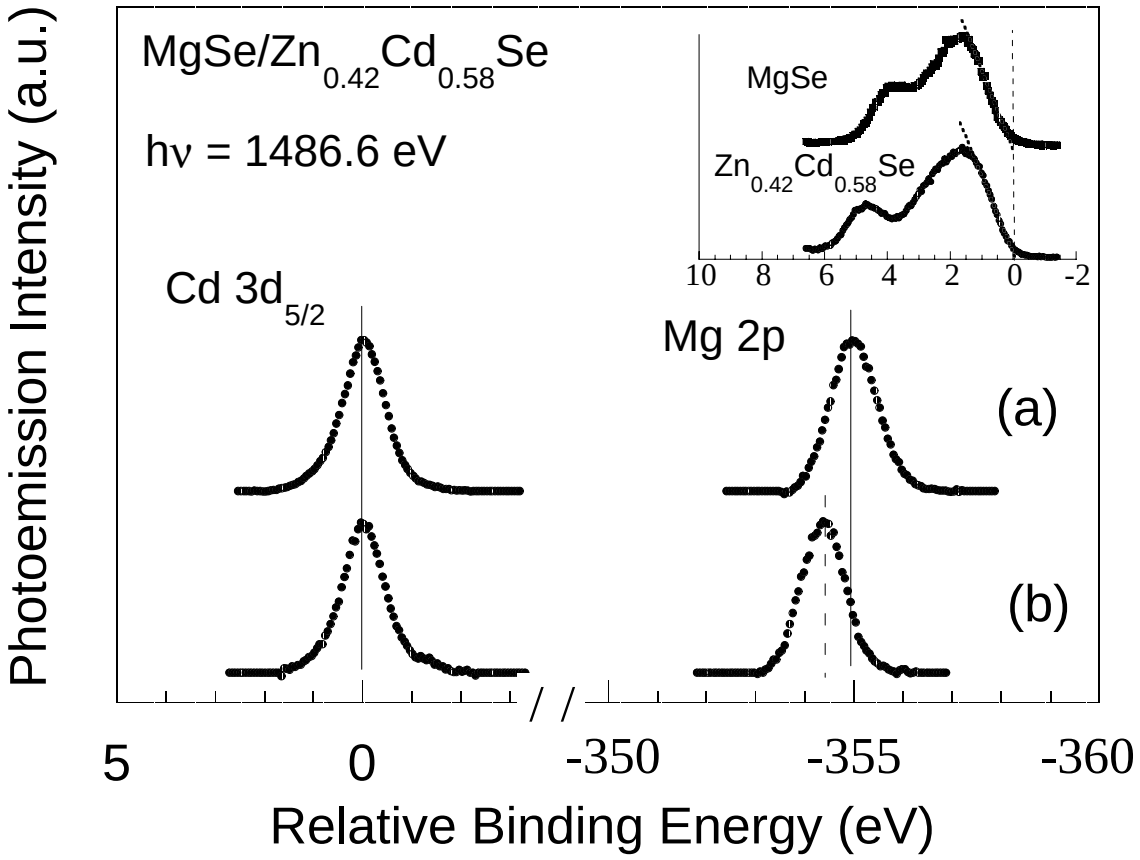

FIG. 4 Photoemission determination of the valence band offset for a MgSe/$Zn_{0.42}Cd_{0.58}$Se(001) heterojunction. Inset: valence band emission from $Zn_{0.42}Cd_{0.58}$Se (top) and MgSe (bottom) epitaxial standards. The zero of the binding energy scale is at the linearly extrapolated position of the valence band maximum E_v. (a) Mg 2p and Cd 3d emission from the bulk standards. The apparent core energy separation is that expected from a hypothetical heterojunction with zero valence band offset. (b) Mg 2p and Cd 3d emission from a MgSe/$Zn_{0.42}Cd_{0.58}$Se(001) heterojunction which includes a 3nm thick MgSe overlayer. The variation in the core separation relative to (a) gives directly the valence band discontinuity ΔE_v=0.57±0.05eV.

4.3.2 Experimental results

The valence band offset ΔE_v was then determined experimentally by means of XPS *in-situ* from the position of the Mg 2p and Cd 3d core levels relative to the valence band maximum E_v in thick epitaxial standards, and the observed energy separation ΔE_{cl} between the Mg 2p and Cd 3d core levels at the heterojunction interface. Representative results are shown in Fig. 4 for a MgSe/$Zn_{0.42}Cd_{0.58}Se$ heterostructure. In the inset, we show valence band spectra for a 0.5 μm-thick $Zn_{0.42}Cd_{0.58}Se$ epitaxial layer (top) and a 0.07 μm thick-MgSe epitaxial layer (bottom). The zero of the binding energy scale corresponds to the valence band maximum E_v, as determined from a least-squares linear extrapolation of the leading valence band edge.

Spectra for the Mg 2p and Cd $3d_{5/2}$ emission from the same samples are shown immediately below the inset. The core positions referenced to E_v for each sample were 48.93±0.05 and 403.90±0.05 eV, respectively. The apparent core energy separation of 354.97±0.05 eV in Fig. 4 (solid vertical lines) is therefore that expected from a hypothetical heterojunction with zero valence band offset. In the bottom-most section of Fig. 4 we show the core level emission from a MgSe/$Zn_{0.42}Cd_{0.58}Se$ heterojunction which includes a 3nm thick overlayer. The variation in the core separation relative to the previous result was independent of overlayer thickness in the thickness range of interest (1-5 nm) and gives directly the MgSe/$Zn_{0.42}Cd_{0.58}Se$(100) heterojunction valence band offset of 0.57±0.05 eV.

In Fig. 5 we summarize our measurements of the valence band offset for the six interfacial systems examined, at different overlayer coverages. Solid symbols denote results for $Zn_{1-y}Mg_ySe/Zn_{1-x}Cd_xSe$ heterojunctions, open symbols for $Zn_{1-x}Cd_xSe/Zn_{1-y}Mg_ySe$ heterojunctions. Different symbol shapes correspond to results from different experimental runs. The quoted experimental uncertainty (see vertical error bars in Fig. 5) takes into account the combined uncertainty in core level position and alloy composition.

The value of the measured offsets are summarized in Table I. For $Zn_{0.90}Cd_{0.10}Se$ /$Zn_{0.85}Mg_{0.15}Se$ and $Zn_{0.85}Mg_{0.15}Se/Zn_{0.90}Cd_{0.10}Se$ interfaces (topmost panel in Fig. 5) we observed valence band offsets of 0.04±0.05 and 0.12±0.05 eV, respectively. Strictly speaking, the two values are consistent within experimental uncertainty. However, it should be noted that due

to the method employed in the XPS determination of the offset, deviations from commutativity could be assessed by monitoring solely the core level separation ΔE_{cl} at the interface for the two growth sequences, i.e., without the additional uncertainty due to the determination of the core level position relative to E_v in bulk standards. For the two junctions examined we observed interface core level separations ΔE_{cl} of 354.72±0.03 and 354.64±0.03 eV, clearly suggestive of a 0.08 eV deviation from commutativity.

Since the bandgap difference ΔE_g between the two materials at room temperature is about 0.295 eV,[79,85] the measured valence band offsets would correspond to valence band contributions to the bandgap difference Q_v of 0.14±0.17 and 0.41±0.17, respectively, for the two heterojunctions.

For $Zn_{0.85}Cd_{0.15}Se/Zn_{0.74}Mg_{0.26}Se$ and $Zn_{0.74}Mg_{0.26}Se/Zn_{0.85}Cd_{0.15}Se$ junctions (centre panel in Fig. 5) we determined valence band offsets of 0.14±0.05 and 0.25±0.05 eV, respectively. The corresponding interface core level separations ΔE_{cl} of 354.63±0.03 and 354.52±0.03 eV, indicate a 0.11 deviation from commutativity, clearly exceeding the combined experimental uncertainty. At room temperature ΔE_g=0.439 eV,[79,85] so that the corresponding values of Q_v would be 0.32±0.11 and 0.57±0.11, respectively.

Finally, for $Zn_{0.42}Cd_{0.58}Se/MgSe$ and $MgSe/Zn_{0.42}Cd_{0.58}Se$ heterojunctions (bottom-most panel in Fig. 5) we determined ΔE_v=0.57±0.05 and 0.60±0.05 eV, respectively. Such values are consistent with the result of 0.56±0.07 reported by Wang et al.[80] for $MgSe/Zn_{0.46}Cd_{0.54}Se$, and show no deviations from the predictions of the commutativity rule. If one uses the room-temperature value proposed by Lunz et al.[44] for MgSe, ΔE_g =2.03 eV,[85] leading to Q_v values of 0.28±0.03 and 0.30±0.03 for the two types of heterojunctions.

According to linear response theory (LRT), deviations of the band offsets from the predictions of the commutativity and transitivity rules are not expected in lattice-matched, isovalent heterojunctions such as $Zn_{1-y}Mg_ySe/Zn_{1-x}Cd_xSe$.[78,106]

LRT indicates that in isovalent heterojunctions the band alignment should be primarily a property of the bulk semiconductor constituents, and therefore commutative, transitive, and relatively independent of the local atomic configuration. Conversely, for heterovalent

heterojunctions with polar orientation current theories do predict a strong dependence of the band discontinuities on the atomic configuration of the interfaces.[78,106]

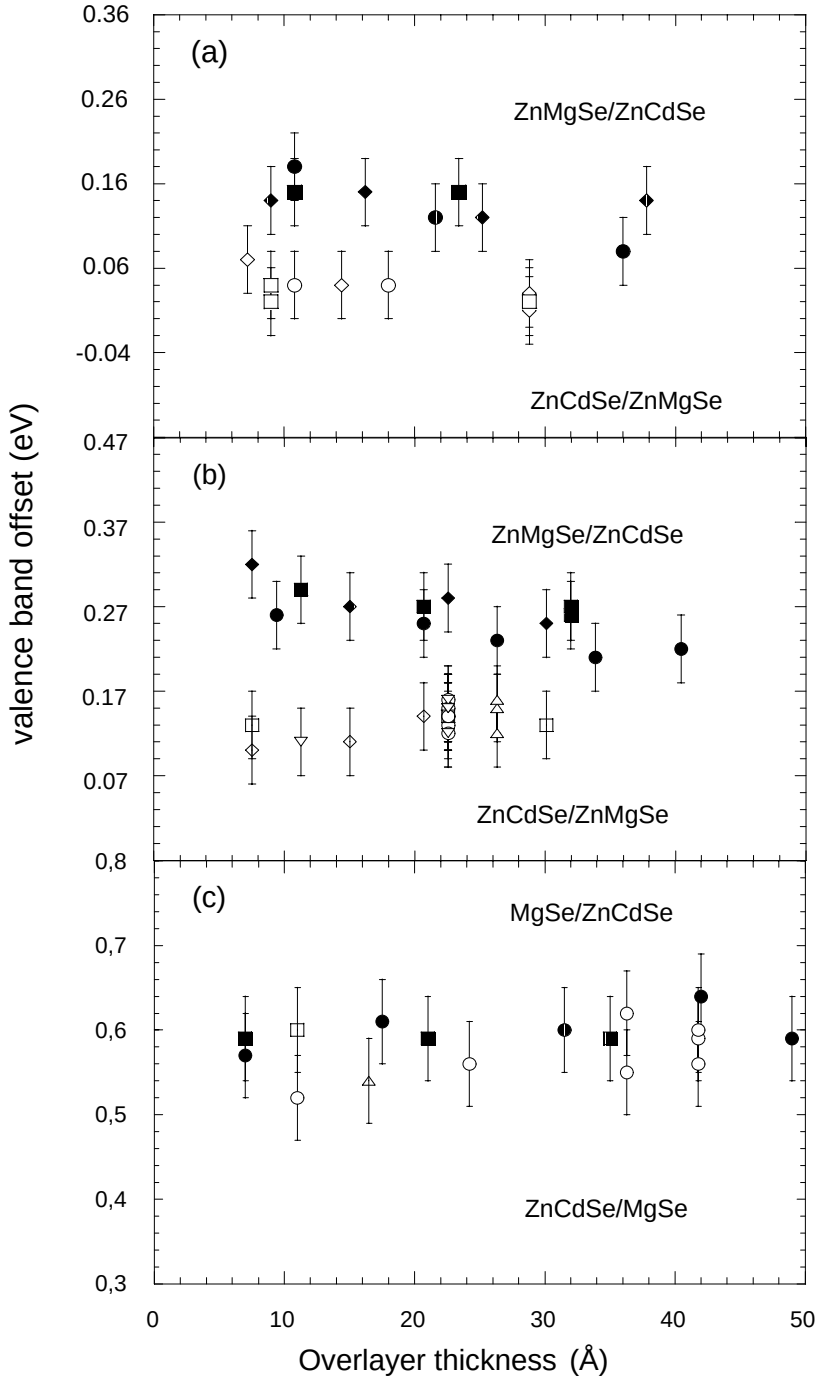

FIG. 5 Photoemission-determined valence band offsets for six lattice-matched interfacial systems as a function of overlayer thickness. Solid symbols denote results for $Zn_{1-y}Mg_ySe$ overlayers on $Zn_{1-x}Cd_xSe$ substrates, while open symbols show the corresponding results for $Zn_{1-x}Cd_xSe$ overlayers on $Zn_{1-y}Mg_ySe$ substrates. Different symbol types denote results from different experimental runs.
(a) $Zn_{0.90}Cd_{0.10}Se/Zn_{0.85}Mg_{0.15}Se$ and $Zn_{0.85}Mg_{0.15}Se/Zn_{0.90}Cd_{0.10}Se$ interfaces.
(b) $Zn_{0.85}Cd_{0.15}Se/Zn_{0.74}Mg_{0.26}Se$ and $Zn_{0.74}Mg_{0.26}Se/ Zn_{0.85}Cd_{0.15}Se$ interfaces.
(c) $Zn_{0.42}Cd_{0.58}Se/MgSe$ and $MgSe/Zn_{0.42}Cd_{0.58}Se$ interfaces.

Two types of arguments have been put forth to explain why the band alignment at isovalent heterojunctions might come to depend on the growth conditions and/or the growth sequence. In the case of BeTe/ZnSe heterojunctions it has been proposed that the highly covalent character of one type of II-VI bond (Be-Te) relative to the other (Zn-Se), would make LRT arguments inappropriate, so that such interfaces would behave more as heterovalent than isovalent heterojunctions.[102] Alternatively, the experimental observations could be reconciled with LRT predictions if charged point defects - such as antisites - were to be present at the interface.[106,81]

4.4. Theoretical predictions

To gain further insight into the factors influencing the band alignment, *ab-initio* pseudopotential calculations of the heterostructure electronic and structural properties were performed, following the approach described in detail in Ref. 106. A cutoff energy of 25 Ry, a set of 10 special k points in the irreducible part of the Brillouin zone for the bulk zincblende calculations, and an almost equivalent sampling for the supercell calculations was used. Some details on these results for the structural properties have been discussed in Chapter 3 for $Zn_{1-y}Mg_ySe$ alloys. The same technique was used for $Zn_{1-x}Cd_xSe$ alloys. We only emphasize here that the pseudopotentials employed reproduced quite well the experimental lattice parameters and bulk moduli of all binary parent compounds. For the ternary alloys, an almost linear variation of the average lattice parameter with composition was obtained. The calculations indicate approximately y/x~1.6 as a condition for lattice matching.

The band offsets at all compositions were evaluated using the virtual crystal approximation for the alloys. The accuracy of the results was verified by performing calculations with true -as opposed to virtual- atoms for selected stoichiometries. In particular, $MgSe/Zn_{0.375}Cd_{0.625}Se$ (Zn:Cd=3:5), and $Zn_{0.75}Mg_{0.25}Se/Zn_{0.833}Cd_{0.167}Se$ (Zn:Mg=3:1 and Zn:Cd=5:1) heterojunctions were selected. Such systems have stoichiometries as close as possible to the compositions of some of the experimental samples, and are suitable to be described using a

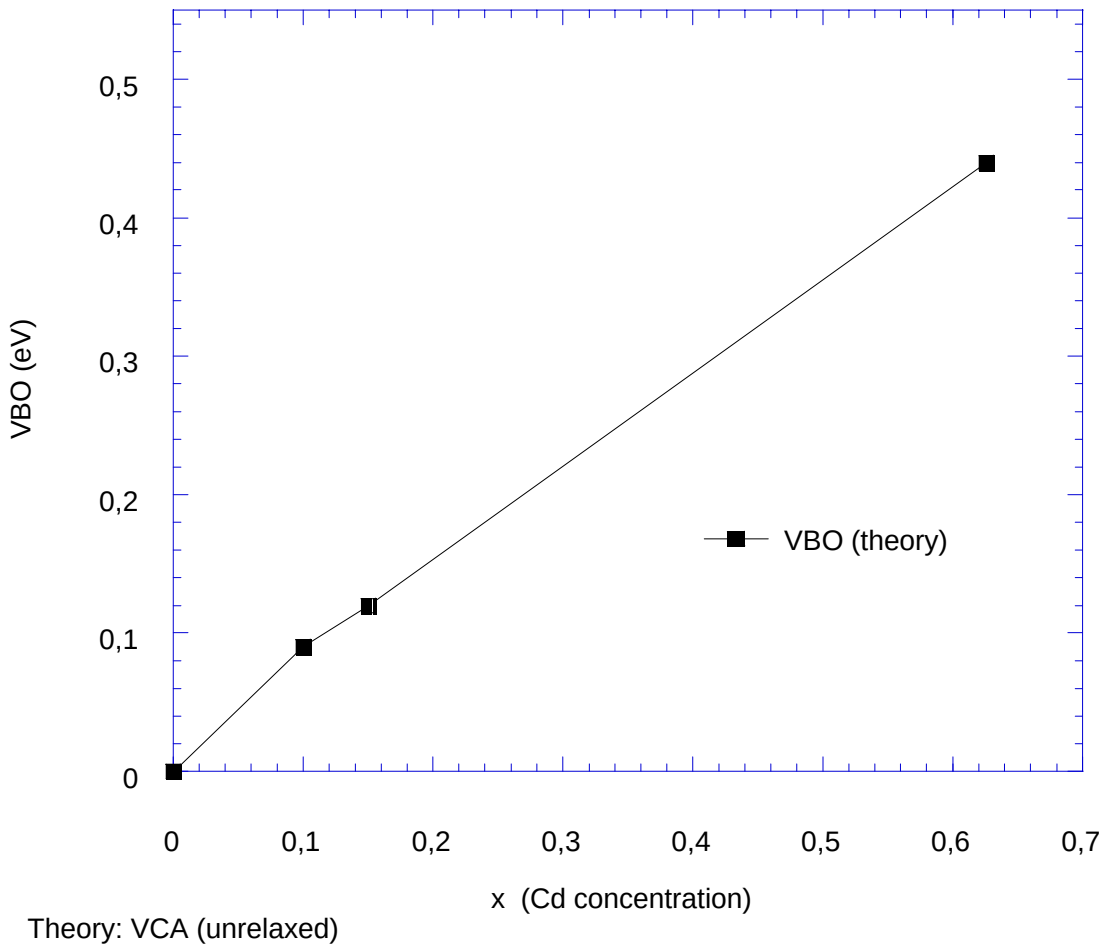

FIG. 6 VBO values as a function of Cd concentration for the three junctions examined theoretically, before self-energy corrections. The continuous line is a guide for the eye. A small positive bowing of ΔE_v relative to a linear interpolation between the y=0 and y=1 (y/x=1.6) values is found.

reasonable number of true atoms in the supercell. The two types of calculations gave consistent results, within the numerical accuracy of the calculations, which was of the order of 20 meV.

The calculated valence band offsets for the heterojunctions examined experimentally (Fig. 6), prior to any self-energy and relativistic corrections, were 0.09 eV (y=0.16; x=0.10), 0.12 eV (y=0.24; x=0.15), and 0.44 eV (y=1; x=0.626), and reflect a small positive bowing of ΔE_v relative to a linear interpolation between the y=0 and y=1 (y/x=1.6) values (Fig. 6). We stress that the validity of LRT does not necessarily imply a linear dependence of ΔE_v on alloy composition, as explained in Ref. 106.

A substantial uncertainty in the above theoretical predictions may in principle derive from the use of density-functional theory in the local-density approximation (DFT-LDA), and from the nonrelativistic (i.e., spin-averaged) approach. As far as relativistic corrections are concerned, the spin-orbit splittings can be added *a posteriori* to the calculated valence band maxima for the two semiconductors comprising the junctions. The reported experimental spin-orbit splittings are very similar, i.e., 0.40-0.43 eV in ZnSe,[52,82] 0.42 eV in CdSe,[52] and 0.435 eV in MgSe,[40] because the common anion dominates the behaviour of the topmost valence bands. Therefore in what follows we will neglect the relativistic correction to the valence band offsets, which would be smaller than the numerical accuracy of the calculations.

Self-energy corrections can also be added *a posteriori* to the calculated valence band maxima for the two semiconductors comprising the junctions. *Ad hoc* calculations are not available, but an estimate can be derived from existing calculations for other lattice-matched, isovalent common-anion systems, namely AlX/GaX(001) (with X=As, P or Sb), for all of which a self-energy related increase of about 0.11 eV (specifically ranging from 0.09 to 0.12 eV in the series) was calculated in ΔE_v.[83] This reflected the increased downward shift of E_v in AlX relative to E_v in GaX as a result of the larger ionicity of AlX relative to GaX.

Because self-energy corrections to the band offsets in common-anion systems are determined by the difference in the cation cores, one can exploit the similarity between Mg and Al cores, and between Zn - and, to a lesser extent, Cd - and Ga cores, to extend the above results for AlX/GaX to lattice-matched $Zn_{1-y}Mg_ySe/Zn_{1-x}Cd_xSe$ heterojunctions. One would expect a maximum self-energy related increase of about 0.11 eV in ΔE_v, scaling linearly with the Mg concentration y and relatively independent of the Zn to Cd ratio. The estimated self-energy corrections for the three heterojunction systems in Fig. 5 would therefore be 0.02, 0.03 and 0.11 eV. The resulting calculated valence band offsets of 0.11, 0.15 and 0.55 eV (at 0K) have been included in Table I. The final, overall uncertainty in the calculated offsets is estimated to be ±0.05 eV.

Using experimental, low temperature (at 4-10K) values of the bandgaps of $Zn_{1-y}Mg_ySe$ and $Zn_{1-x}Cd_xSe$, (see Ref. 86 for details on how these values have been obtained) for the three interface systems we would expect bandgap differences ΔE_g of 0.327, 0.482, and 2.111 eV,

respectively. Using such bandgap differences, and the above calculated values of ΔE_v, our best predictions for Q_V are 0.34, 0.31, and 0.26, respectively, also included in Table I.

Table I

Interface	ΔE_V (exp., eV)	ΔE_V (th., eV)	Q_V (exp.)	Q_V (th.)
y=0.15 on x=0.10	0.04±0.05	0.11	0.14±0.17	0.34
x=0.10 on y=0.15	0.12±0.05		0.41±0.17	
y=0.26 on x=0.15	0.14±0.05	0.15	0.32±0.11	0.31
x=0.15 on y=0.26	0.25±0.05		0.57±0.11	
y=1 on x=0.58	0.57±0.05	0.55	0.28±0.03	0.26
x=0.58 on y=1	0.60±0.05		0.30±0.03	

Table 1 Experimental and theoretical determinations of the band alignment in a series of lattice-matched, (001)-oriented $Zn_{1-y}Mg_ySe/Zn_{1-x}Cd_xSe$ (rows 1, 3, and 5) and $Zn_{1-x}Cd_xSe/Zn_{1-y}Mg_ySe$ (rows 2, 4, and 6) heterojunctions. Column 1: composition of the semiconductor constituents. Column 2: photoemission-determined value of the valence band offset. Column 3: valence band offsets from ab-initio pseudopotential calculations. Column 4: experimental valence band contribution to the bandgap difference, from room temperature data for the alloy bandgaps. Column 5: predicted valence band contribution to the bandgap difference, from low temperature data for the alloy bandgaps.

In general, one should not expect a constant value of Q_V with varying alloy concentration.[106] Specifically, the calculations suggest that the predicted decrease in Q_V with increasing Cd and Mg concentration originates from the larger bowing of ΔE_v as compared to ΔE_g. If we write the y-dependence of the two quantities as: $\Delta E_v(y) = a \cdot y + b \cdot y(1-y)$ and $\Delta E_g(y) = a' \cdot y + b' \cdot y(1-y)$, we obtain: $\frac{dQ_v}{dy}(y) = (ab' - a'b) \cdot \left[\frac{y}{\Delta E_g(y)}\right]^2$. Since the calculated b/a, i.e., the offset bowing, is almost twice as large as b'/a', i.e., the bandgap bowing, then (ab'-

a'b)=aa'(b'/a'-b/a) is negative, and Q_V is predicted to decrease with increasing Mg and Cd (y/x=1.6) concentration.

The above considerations, however, should be taken with some caution, since estimates of bowing are complicated by the uncertainties affecting the theoretical values of the bandgaps and, to a lesser extent, of the valence band offsets.

4.5. Conclusions

Within the combined experimental and theoretical uncertainty, the theoretical predictions are generally consistent with experiment, both for the y/x~1.6 lattice matching and the band alignment. The 70:30 ratio in the conduction to valence band offset is especially comforting in view of the proposed application of $Zn_{1-y}Mg_ySe/Zn_{1-x}Cd_xSe$ lattice-matched heterostructures in strain-free lasers, since it will guarantee effective carrier confinement in the quantum well. Theory, however, does not predict the small, but detectable deviations from commutativity observed experimentally for heterojunctions involving ternary overlayers in Fig. 5.

The results of the calculations suggest that any difference in the nature of the Mg-Se bond relative to the Zn-Se or Cd-Se bond, cannot explain *per se* the observed deviations, since the difference is fully captured by the *ab-initio* approach, and the related numerical results support the LRT framework. The possible formation of charged point defects, such as antisites, during heterostructure fabrication remains therefore the most likely candidate to explain the experimental deviations from the LRT predictions.

Chapter five: Multiple quantum well structures

5.1. Introduction

We report here a first characterization of the electronic properties of lattice-matched $Zn_{1-x}Cd_xSe/Zn_{1-z}Mg_zSe$ multiple quantum well structures grown by MBE on graded-composition $In_yGa_{1-y}As$ substrates. We focus, in particular, on the QW excitonic properties, and on the band alignment across the QW boundaries.

All heterostructures were fabricated in our multi-chamber systems. A 1 μm-thick, graded composition $In_yGa_{1-y}As$ buffer was first grown on GaAs(001)2x4 substrates at T = 500°C, with a III/V BPR in the 1/15÷1/30 range and a growth rate of about 1.5 μm/h. A superlinear, parabolic composition profile with y varying from 0 to 0.25 during growth was obtained by gradually increasing the In cell temperature. As discussed in Chapter 2, the in-plane *surface* lattice parameter of such layers is matched to the bulk lattice parameter of $Zn_{1-x}Cd_xSe$ alloys with x=0.15 (blue emitters). The structures were designed so that $a_{||}(In_yGa_{1-y}As)=a_0(Zn_{0.85}Cd_{0.15}Se)=a_0(Zn_{0.74}Mg_{0.26}Se)=5.730$ Å, where $a_{||}$ is the in-plane, surface lattice parameter of the partially relaxed $In_yGa_{1-y}As$ graded buffer, and a_0 is the bulk lattice parameter of the unstrained alloys within the QW and barrier layers. The maximum lattice mismatch which was observed as a result of unintentional variations in the alloy composition was of the order of ~0.1-0.2 %. We emphasize that within the graded III-V buffer, misfit dislocations are spatially distributed in a ~0.2-0.5 μm-thick region adjacent the $In_yGa_{1-y}As$/GaAs interface, and the reduced dislocation interaction leads to a topmost region free from threading dislocations, within experimental uncertainty.[11,12] The surfaces of such $In_yGa_{1-y}As$ substrates, however, exhibit a characteristic pattern of corrugations that represent a potential challenge to their utilisation.[11,12,26,27,84] We probed such corrugations prior to II-VI overlayer growth using atomic force microscopy (AFM). The As cap layer used to protect the substrate during transfer to the II-VI MBE chamber was thermally desorbed from subsections of the wafer and the surface was analyzed by AFM *ex-situ*,

using a commercial instrument operated in contact mode, with Si_3N_4 tips on cantilevers with a spring constant of 0.12 N/m. Typical scan rates were in the 0.5-2 Hz range.

Fig. 1(a) shows the general morphology of the surface. Parallel corrugations extend throughout the 12 µm x 12 µm sampled area along the [110] direction, with smaller perpendicular corrugations extending in the $[1\bar{1}0]$ direction. An AFM line-scan recorded along the [110] direction is shown in Fig. 1(b). The amplitude of the surface corrugations is of the order of 5-10 nm, and their period of the order of 0.5-1.0 µm.

On the $In_yGa_{1-y}As$ surfaces $Zn_{0.74}Mg_{0.26}Se$ barrier layers and $Zn_{0.85}Cd_{0.15}Se$ QWs were

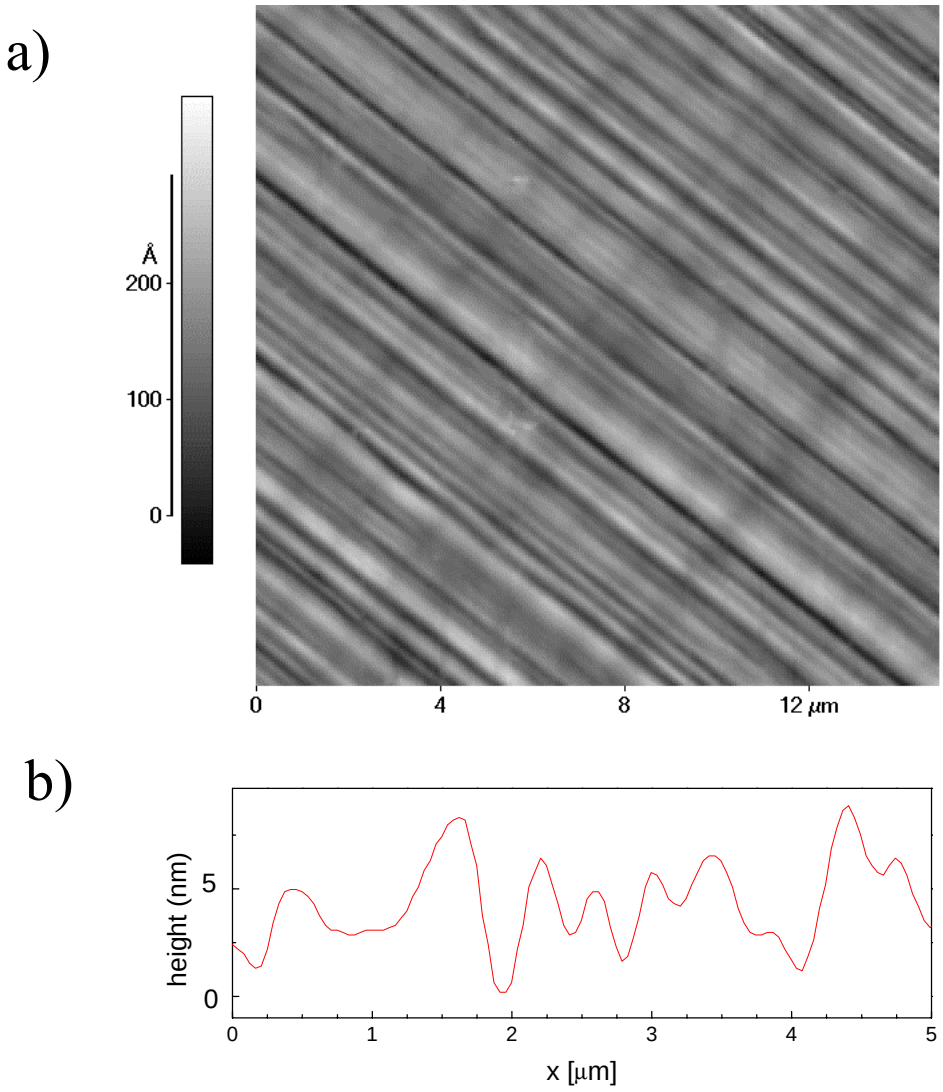

FIG. 1 AFM image of the In(y)Ga(1-y)As graded buffer surface (a); line scan recorded along the [110] direction (b).

fabricated at 280°C in Se-rich growth conditions (Zn to Se BPR 0.35-0.38), as confirmed by the 2x1 reconstruction in the reflection high energy electron diffraction (RHEED) pattern, with a growth rate of about 0.6 μm/h. The II-VI overlayer growth mode was layer-by-layer in all cases, as indicated by RHEED. A growth interruption of 2 s was employed at each interface. Lattice matching and alloy compositions were determined by XRD, and XPS as described in Chapters 3-4.

Several types of samples were fabricated to study the evolution of the quantum-confined states. Following growth of an initial, 80 nm-thick $Zn_{0.74}Mg_{0.26}Se$ buffer layer on $In_yGa_{1-y}As$, ten period structures were grown, with $Zn_{0.85}Cd_{0.15}Se$ QW of constant width L_W=1.1, 3.4, 4.8, 7.6, or 11.4 nm, separated by 32 nm-wide $Zn_{0.74}Mg_{0.26}Se$ barrier layers. A final, 15 nm-thick ZnSe cap-layer was grown to prevent oxidation of the topmost $Zn_{0.74}Mg_{0.26}Se$ barrier. The expected bandgap difference between the QW and the barrier materials is 0.439 eV at room temperature,[79,85] and 0.482 eV at 15K,[86] so that an improvement in quantum confinement is expected as compared to conventional $Zn_{1-x}Cd_xSe$/ZnSe QWs.

5.2. TEM findings

The structural quality of the final structures was investigated by cross-sectional transmission electron microscopy (TEM), using a Philips CM30-T microscope operated at 300 kV and equipped with a Gatan 794 MSC camera in collaboration with Dr. Parisini and co-workers at LAMEL Institute of CNR, in Bologna. Specimens were cut and prepared by conventional ion thinning. Representative results for a multiple quantum well structure with nominal L_W=4.8 nm are shown in Fig. 2. In Fig. 2(a) a bright-field, cross-sectional TEM micrograph clearly shows the InGaAs graded layer and the II-VI quantum well region. As expected, the topmost region of the InGaAs graded layer appears free from threading dislocations. In Fig. 2(b) the II-VI layer is shown in more detail. The individual $Zn_{0.85}Cd_{0.15}Se$ QWs, exhibit long-period undulations, which reflect corrugations of the underlying $Zn_{0.74}Mg_{0.26}Se/In_yGa_{1-y}As$ interface, and good coherence between the different periods.

From the results in Fig. 2(b) and analogous images from different regions of the same sample, we determined QW and barrier layer thicknesses of 5.0±0.6 and 32.2±0.6 nm, consistent

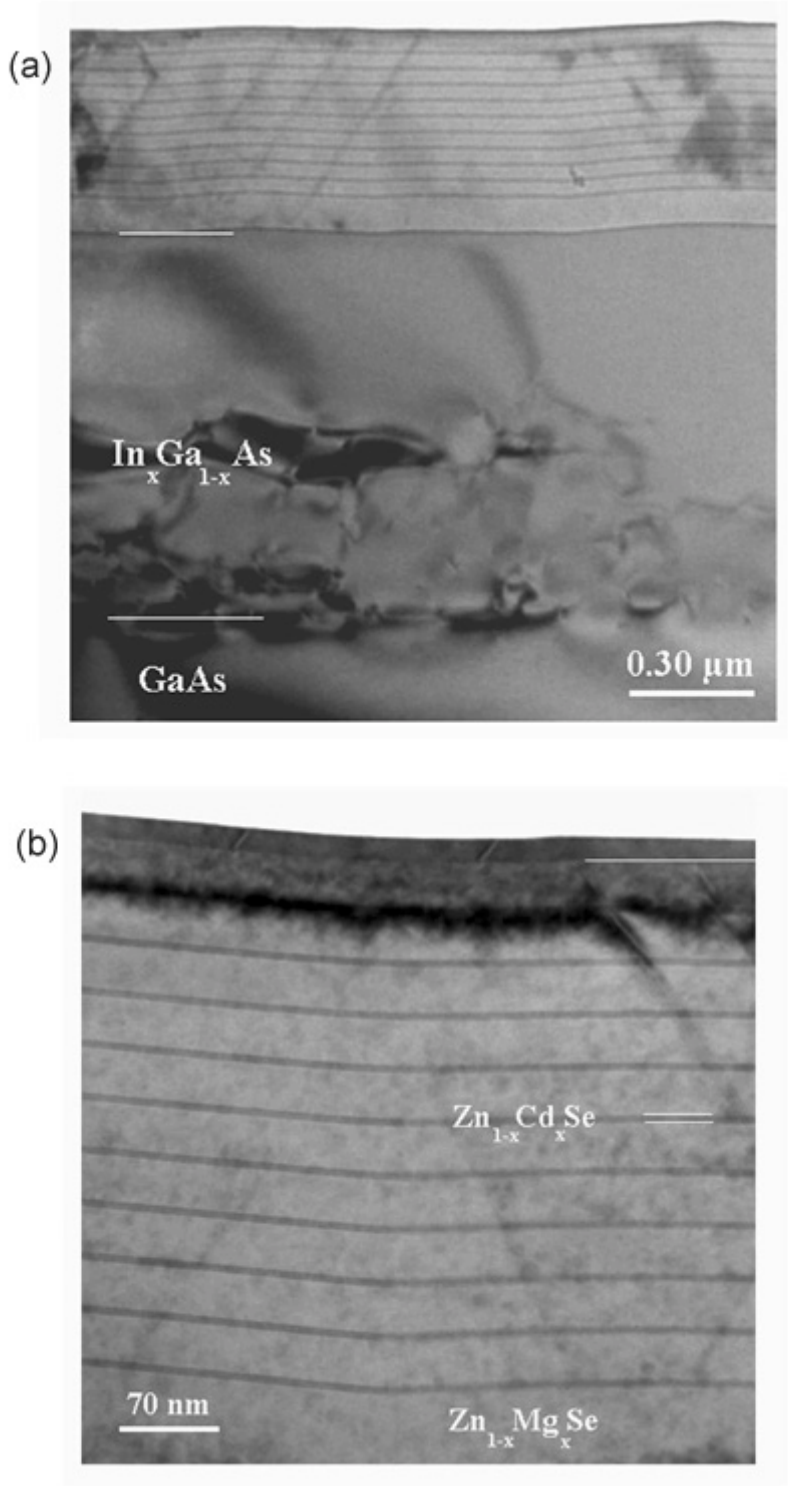

FIG 2 Cross sectional TEM micrograph of the 4.8-nm-thick lattice matched MQW heterostructure.(a) View of the whole structure. (b) Detail of the II-VI layer.

with the nominal values. The undulation amplitudes are typically of 5-10 nm, and the corresponding period of 0.5-1.0 μm, in agreement with the AFM results of Fig. 1.

The results in Fig. 1-2 imply that the cross-hatched pattern of the initial $In_yGa_{1-y}As$ surface poses no obstacle to the implementation of high-quality multiple quantum well structures. This is a fortunate result of the conformal growth of both $Zn_{1-x}Cd_xSe$ quantum well layers and the $Zn_{1-z}Mg_zSe$ barrier layers onto the III-V substrate. We caution the reader that a substantial density of stacking faults (SFs) was also present on {111} planes. Such SFs, out of focus in Fig. 1, are present in all II-VI structures grown on III-V substrates, including state-of-the-art laser structures, are not affected by strain and do not contribute to strain relaxation.

We emphasize that the SF concentration can be controlled by implementing growth procedures already established for ZnSe/GaAs heterostructures. A first possible procedure would consists of preexposuring the InGaAs surface to a Zn flux prior to the II-VI growth and an initial migration-enhanced epitaxy (MEE) of the II-VI layer. In the case of ZnSe on GaAs this procedure leads to final defect densities below $10^4/cm^2$.[87,88,89,90] Heun et al. have reported an alternate way of reducing the stacking faults density.[91] The technique involves growth of a thin composition-control interface layer (CIL) at the II-VI/III-V interface. CIL consisting of a 2nm thick ZnSe layer grown with a Zn/Se beam pressure ratio (BPR) of 0.1, yielded a final defect density below $10^5/cm^2$.[91]

5.3. Optical results

The electronic structure of the QW samples was investigated by means of photoluminescence (PL) and optical absorption spectroscopy by our optical group. All measurements were performed at 15 K using a closed-cycle He refrigerator. For PL measurements, the 363 nm line from an Ar^+ ion laser was focused at normal incidence onto the sample surface. The PL emission was collected in a backscattering geometry along the growth direction and dispersed by a 0.05-nm resolution monochromator. For optical absorption measurements, the substrates were mechanically thinned down to about 50 μm, and circular areas of the III-V substrate - about $6x10^{-4}$ cm^2 in size - were selectively removed by photolithographic

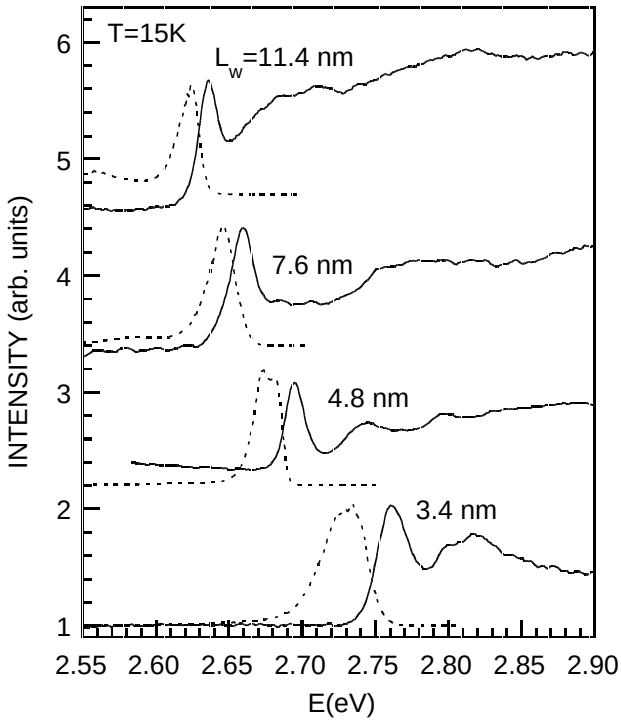

FIG. 3 Low temperature (15K) photoluminescence (dashed line) and absorption (solid line) spectra of lattice matched MQW heterostructures with different QW thickness.

and wet-etching techniques. Mechanical damage to the structures was ruled out by comparing PL spectra recorded before and after substrate removal.

In Fig. 3 we show representative PL (dashed line) and absorption spectra (solid line) for different QWs. The optical absorption spectrum for the L_W=4.8 nm sample is also shown in an expanded scale in the inset of Fig. 4. All absorption spectra exhibit a sharp fundamental peak followed by weaker and broader features at higher energies, corresponding to transitions involving excited states and characteristic of heterostructures where good quantum confinement has been achieved.

The PL lineshape in all samples reflects the partial superposition of two emission features. The linewidth of the QW overall emission line is only slightly reduced (by 10-20%) when the luminescence is collected from samples containing a single QW, indicating good reproducibility of the QW layers. Based on the dependence of the relative intensity of the two emission features on excitation power density and temperature (not shown), we associate the higher-energy emission feature with free-exciton recombination, and the lower-energy peak, with

impurity-bound exciton emission. Analogous donor-bound exciton emission features are observed in PL from bulk ZnSe,[92] $Zn_{1-x}Cd_xSe$ and $Zn_{1-z}Mg_zSe$ (not shown), as well as from pseudomorphic $Zn_{1-x}Cd_xSe$/ZnSe QWs on GaAs.[93,94]

The linewidth of the fundamental absorption peak and the Stokes shift relative to free-exciton PL feature, measured at high excitation power, are summarized in Table I for the different samples. The data in Table I compare well with those observed in the highest-quality, pseudomorphic $Zn_{1-x}Cd_xSe$/ZnSe multiple QW structures grown on GaAs.[95,96,97] This is a further indication that growth on the cross-hatched $In_yGa_{1-y}As$ surface does not hinder the structural quality of the QWs.

TABLE I

L_w(nm)	FWHM(eV)	ΔE_{ss}(eV)
1.1	0.0308	0.0328
1.9	0.0348	0.0366
2.7	0.0228	0.0204
3.4	0.0190	0.0252
4.8	0.0144	0.0136
7.6	0.0140	0.0204
11.4	0.0135	0.0109

Table 1 Full width at half maximum (FWHM) of the fundamental absorption peaks and Stokes shift (ΔE_{ss}) observed in the lattice matched MQW samples at 15K as a function of the quantum well width (L_w).

In the inset of Fig. 4 we have associated the main absorption features with the corresponding QW transition. The heavy- or light-hole character of the transitions, in particular, have been established for all samples from the observed polarisation dependence, and by comparing the experimental values of the peak energies with the predictions of a simplified theoretical model. By increasing the in-plane component of the electric field, the intensity of the first - and third, whenever resolved - absorption feature was found to increase, as expected for a

heavy-exciton transition. Correspondingly, the intensity of the second feature remained unchanged, revealing a light-hole character.[98]

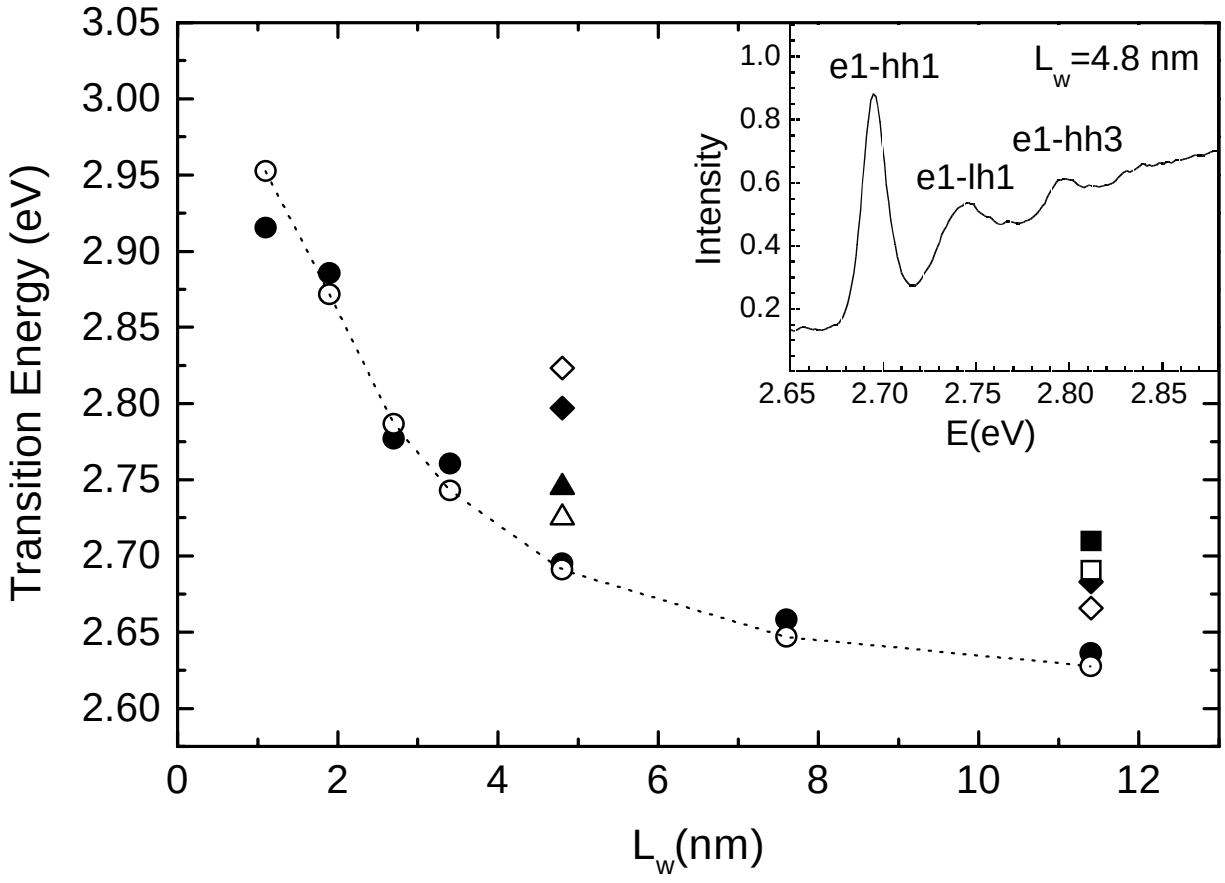

FIG. 4 Inset: detail of the absorption spectrum for a $Zn_{0.85}Cd_{0.15}Se/Zn_{0.74}Mg_{0.26}Se$ MQWS with nominal well thickness of 4.8 nm. Absorption transition energies as a function of well widths for all $Zn_{0.85}Cd_{0.15}Se/Zn_{0.74}Mg_{0.26}Se$ samples studied. Different solid symbols denote the experimental values of the fundamental and excited state transitions: circles for e1-hh1, triangles for e1-lh1, diamonds for e1-hh3, and squares for e2-hh2, respectively. Corresponding open symbols represent the calculated transition energies. The dotted line across the fundamental peak positions is intended only as a guide to the eye.

The energies of the different excitonic transitions were calculated by solving numerically the transcendental equation for the energy levels in a square QW while taking into account the dependence of the exciton binding energy on the well thickness. The latter was implemented following a simple analytic method which assimilates excitons in an anisotropic solid - such as a

QW - to excitons in an isotropic fractional-dimensional space.[99] The method has been shown to yield exciton binding energies in satisfactory agreement with the predictions of more sophisticated variational calculations for GaAs/AlGaAs,[99] and has also been applied successfully to ZnSe/$Zn_xMg_{1-x}S_ySe_{1-y}$ QWs.[100]

As input parameter in our calculations we used L_w, the observed transition energies as a function of L_w, the effective masses in $Zn_{0.85}Cd_{0.15}Se$, and the bandgap of $Zn_{0.74}Mg_{0.26}Se$.[95] The valence band contribution to the bandgap discontinuity $Q_v=\Delta E_v/\Delta E_g$, and the effective masses for $Zn_{0.74}Mg_{0.26}Se$ were used as fitting parameters. Some of the calculated transition energies (open symbols) resulting from the least squares best fit to the experimental transition energies (solid symbols) transition energies are shown in Fig. 4 for the different QW thicknesses examined. In view of the simplistic assumptions employed, the model does a remarkably good job of reproducing the experimental dependence of the fundamental excitonic feature on the QW thickness. The agreement is somewhat less impressive for transitions involving excited states, as expected since the two-band calculation does not take into account valence band mixings and Coulomb coupling between excitons belonging to different subbands,[99] but still sufficient to confirm the identifications proposed based on the polarisation-dependence of the different excitonic absorption features (see inset of Fig. 4).

The best fit in Fig. 4 corresponds to $Q_v=0.32$, and barrier effective masses $m_e=0.09m_0$, $m_{hh}=0.38m_0$, and $m_{lh}=0.07m_0$ for electrons, heavy- and light-holes, respectively. The effective masses are somewhat lower than expected, since they are measurably smaller than those of the QWs,[101] but we emphasize that the value of Q_v is largely insensitive to the actual values of the effective masses employed for the barrier. For example, when taking the same approach as Miyajima et al. for ZnSe/$Zn_xMg_{1-x}S_ySe_{1-y}$ QWs,[99,100] and fixing the barrier effective masses at the QW effective mass values,[100,101] we found only minimal variations in Q_v ($Q_v=0.33$). We conclude that the fitting procedure is sufficiently robust to derive a reliable estimate of the important band-structure parameter Q_v, which will play a central role in determining electron and hole confinement and injection.

The XPS results in Chapter 4, however, argued for a band alignment dependent on the growth sequence, with $Q_v=0.32$ for $Zn_{0.74}Mg_{0.26}Se$ overlayers on $Zn_{0.85}Cd_{0.15}Se$ and $Q_v=0.57$ for

$Zn_{0.85}Cd_{0.15}Se$ overlayers on $Zn_{0.74}Mg_{0.26}Se$. We have no evidence of the asymmetric quantum confinement expected from non-commutative heterojunction band offsets in our optical data. Admittedly, the simple theoretical model described in this chapter used only symmetric quantum wells, but the observed excitonic properties were well described by such symmetric QWs with Q_v=0.32 as opposed to a situation intermediate between Q_v=0.32 and Q_v=0.57.

We suggest that charged point defects responsible for the deviations of the band offsets from LRT predictions were effectively annealed-out during the growth process of the multiple quantum well structures. The $Zn_{0.85}Cd_{0.15}Se/Zn_{0.74}Mg_{0.26}Se$ heterostructures examined by XPS in Chapter 4 included 30Å-thick overlayers grown in about 15s at 280 °C and the overlayers were directly exposed to the UHV environment during cooling to room temperature and x-ray illumination. The MQWs examined in this work were grown in about 30 minutes at 280 °C and a ZnSe cap layer was used to protect the uppermost surface. Growth interruptions did not exceed 2 seconds, so that none of the interfaces was exposed the UHV environment for more than a few seconds. It is therefore not surprising that the formation of charged point defects might be easier in the thin films samples examined by XPS than in the MQWs examined in this chapter. An analogous, if more dramatic, situation exist in the literature for BeTe/ZnSe interfaces. Photoemission data have been interpreted in terms of a valence band offset varying from 0.46 eV to 1.26 eV depending on the growth conditions,[102,103] while optical studies of BeTe/ZnSe superlattices have been found to be invariably consistent with a valence band offset of about 0.9 eV, independent on the growth sequence.

5.4. Conclusions

We have successfully fabricated lattice-matched $Zn_{0.85}Cd_{0.15}Se$ multiple quantum well structures using $Zn_{0.74}Mg_{0.26}Se$ barriers and graded-composition $In_zGa_{1-y}As$ buffer layers on GaAs. We have found that the characteristic $In_zGa_{1-y}As$ surface corrugations do not affect the ordered growth of the II-VI multilayers. The linewidth of the main excitonic features and the Stokes shift in the low-temperature absorption spectra compare well with those observed in the highest-quality, pseudomorphic $Zn_{1-x}Cd_xSe/ZnSe$ quantum well structures grown on GaAs. The

measured excitonic properties allowed us to determine the band parameters relevant to electron confinement. Very good agreement between the optical determined Q_v and the calculations of Chapter 4 was found.

Chapter six: Zn/ZnSe

6.1. Introduction

The physical mechanisms that control the band alignment at metal/semiconductor interfaces are still the subject of intense debate.[104,105,106] The recent application of state-of-the-art *ab-initio* computational methods is producing stimulating results[107,108] for the few epitaxial metal/semiconductor contacts available, and further important insight is being obtained by extending to metal/semiconductor interfaces linear-response-theory (LRT) concepts used earlier in the study of heterojunction band offsets.[78,106] In particular, the role of the chemical and structural properties of the two bulk materials comprising the junction as compared to interface-specific effects, is finally being quantitatively assessed.

All such new theoretical approaches, however, are hindered by the lack of experimental information on the local atomic configuration of the interface. Information is usually derived from the trends observed for simplified, model interface configuration. Common criticisms are that calculations for ideal, abrupt interfaces do not take into account atomic intermixing and defects, and neglect as well the possible formation of interface reaction products. For example, in most B/AC interfaces involving a metal B overlayer and an AC compound semiconductor substrate, interface reactivity leads to a partial B-C exchange reaction in which the overlayer atoms react with the substrate anions (A), and the C cations displaced from the substrate are dissolved in the metal overlayer or segregated at the overlayer surface.[105] The interface heat of reaction calculated on the basis of the above phenomenology has been shown to correlate not only with the extent of atomic intermixing, but also in many cases with electronic properties as well.[105]

In view of the above complications, it is surprising that hardly any theoretical or experimental investigation has focused on a specific class of metal/semiconductor interfaces, namely those where the semiconductor cation is also used to fabricate the metallic overlayer (C/AC interfaces). Such common-cation metal/semiconductor junctions should minimize the

interface heat of reaction, and may represent a class of ideal, unreactive interfaces. Therefore, they should be uniquely suited to experimental and theoretical studies of the influence of the interface configuration on the band alignment. Secondly, in common-cation junctions the nature of the metal overlayer univocally determines the chemical potential of the system, and this allows unambiguous theoretical determinations of the formation energies of the different interfacial configurations.

Along these lines, we present in this Chapter comparative experimental and theoretical studies of Zn/ZnSe(001) interfaces. Junctions fabricated by molecular beam epitaxy (MBE) on different initial semiconductor surface reconstructions were investigated *in-situ* by monochromatic x-ray photoemission spectroscopy using new protocols especially suited to the study of common-cation interfaces. Selected junctions were also examined *ex-situ* by current-voltage (I-V) and capacitance-voltage (C-V) measurements. Calculations of the electronic properties and formation enthalpies of the different interfacial configurations were performed using *ab-initio* pseudopotential methods through a collaboration with N. Binggeli and A. Baldereschi, at the Ecole Polytechnique Fédérale of Lausanne.

6.2. Experimental details

All junctions were fabricated in our MBE facility. GaAs(001)2×4 buffer layers 0.5 μm-thick were initially grown at 600°C on GaAs(001) wafers in the III-V MBE chamber after thermal removal of the native oxide. ZnSe epilayers 0.5 to 1 μm-thick ZnSe layers were subsequently deposited at 290°C in the II-VI MBE chamber, with a typical growth rate of about 0.3 μm/h. ZnSe growth with a Zn/Se beam pressure ratio (BPR) of 0.4 or 1.0 was used to obtain Se-terminated 2x1 and Zn-stabilized c(2×2) surface reconstructions, respectively, as monitored by RHEED. The two reconstructions are believed to correspond, respectively, to a fully dimerized monolayer (ML) of Se,[109] and to half a monolayer of Zn atoms on a complete ML of Se, i.e., to an ordered array of Zn vacancies within the outermost layer of Zn atoms.[110,111] The Se-rich 1×1 reconstruction, which involves submonolayer[112] or monolayer amounts[109,113] of excess Se on top of a fully Se-terminated (001) sub-surface, was obtained here by depositing Se onto

ZnSe(001)2×1 surfaces at room temperature for a few seconds, until the 2× reconstruction disappeared.

Samples fabricated for XPS studies included ZnSe epilayers doped with Cl from a $ZnCl_2$ source at variable levels in the n=$3x10^{16}$ to $1x10^{18}$ cm^{-3} range. Samples fabricated for I-V measurements included ZnSe epilayers with a graded doping profile, tailored in order to obtain a 300 nm-thick n^+ layer (~$4x10^{18}$ cm^{-3}) near the interface with the GaAs substrate and decrease the series resistance due to the ZnSe/GaAs heterojunction, while comparatively lower doping ($3x10^{16}$ to $1x10^{17}$ cm^{-3}) was employed within a 500 nm-thick region at the interface with the metal.

After the ZnSe growth was completed, an elemental Zn flux (beam equivalent pressure $1.6x10^{-6}$ Torr) from an effusion cell was used to deposit elemental Zn on the desired substrate kept at room temperature. Overlayers 0.3 to 5 nm thick were typically used for XPS measurements addressing interface chemistry and the Schottky barrier height. The measurements were performed *in-situ* in the analysis chamber connected to the growth chambers. The RHEED pattern following Zn deposition was of polycrystalline type.

I-V and C-V measurements required *in-situ* deposition of 100 nm-thick Zn overlayers onto the different ZnSe surfaces. A final Al layer was deposited *ex-situ* to aid wire-bonding to the metal overlayer. Circular mesas with diameter in the 50-400 μm range were fabricated by standard photolithographic techniques to define the top contacts. Indium was used to fabricate the back contacts. The selective etchant for the metal was HF: H_2O_2: H_20 (1:2:50). The I-V Schottky barrier has been determined by an extrapolation of the log(I) versus V curve to V=0.[114] The barrier height ϕ_{Bn} has been calculated from the intercept I_s for the straight-line portion of the semi-log plot according to

$$\phi_{Bn}=\frac{kT}{q}\ln\left(\frac{AA^*T^2}{I_S}\right)$$

where A is the diode area and A* the Richardson's constant.[114]

The Schottky barrier height was determined from C-V measurements (at the frequency of 1 MHz) by plotting $1/(C/A)^2$ versus V.[114] The barrier height was determined from the intercept

voltage V_i on the V-axis by $\phi_{Bn}=-V_i+ V_0 +kT/q$, where $V_0=(kT/q)\ln(N_C/N_D)$, where N_c is the effective density of states in the conduction band and N_D the concentration of donors.[114]

6.3. Experimental findings

We monitored by XPS the emission from the Se 3d, Se 3p and Zn 3d core levels, as well as the valence band emission, from the different Zn/ZnSe(001) interfaces as a function of Zn coverage to rule out interdiffusion and gauge the Schottky barrier in-situ. Relative to conventional metal/semiconductor photoemission studies, common-anion systems present some additional experimental challenges. In conventional photoemission studies the substrate cation core emission is most often used to gauge interdiffusion and determine the Schottky barrier height.[104,105] This is because its lineshape and intensity is least affected by interface chemistry in the early stages of interface formation. In common-cation metal/semiconductor junctions, however, there is a partial superposition of substrate cation emission features and overlayer emission features, and the available XPS energy resolution is insufficient to separate the two core features with the necessary accuracy. Therefore, new procedures based on the substrate anion core emission and valence band spectra have to be developed and tested.

As an example, we show in Figs. 1-2 selected results for Zn/ZnSe(001) interfaces fabricated at 15°C on the 2×1 surface reconstruction. In the inset of Fig. 1 we show in a semilogarithmic plot the integrated intensity of the Se 3d doublet (solid symbols) and the Se $2p_{3/2}$ singlet (open symbols), normalized to the initial emission from the clean surface, as a function of Zn deposition time. Zn flux calibrations, and the observed exponential attenuation rate in Fig. 1, were consistent with layer-by-layer growth of the Zn overlayer at a rate of 0.04 nm/s, and unity sticking coefficient. The dashed line in the inset of Fig. 1 shows the expected ideal behaviour for layer-by-layer growth in the absence of detectable interdiffusion.[115,116]

In the main body of Fig. 1 we show the Se 3d lineshape (left) and the valence emission (right) from the ZnSe(001)2×1 surface prior to metal deposition (a), and following deposition of 2.4 nm (b) and 4.0 nm (c) of Zn at 15°C. The zero of the energy scale corresponds to the Fermi

level of the spectrometer E_F. The lineshape of the Se 3d core levels remains unchanged with increasing Zn deposition, as expected in the absence of any relevant interface chemistry.

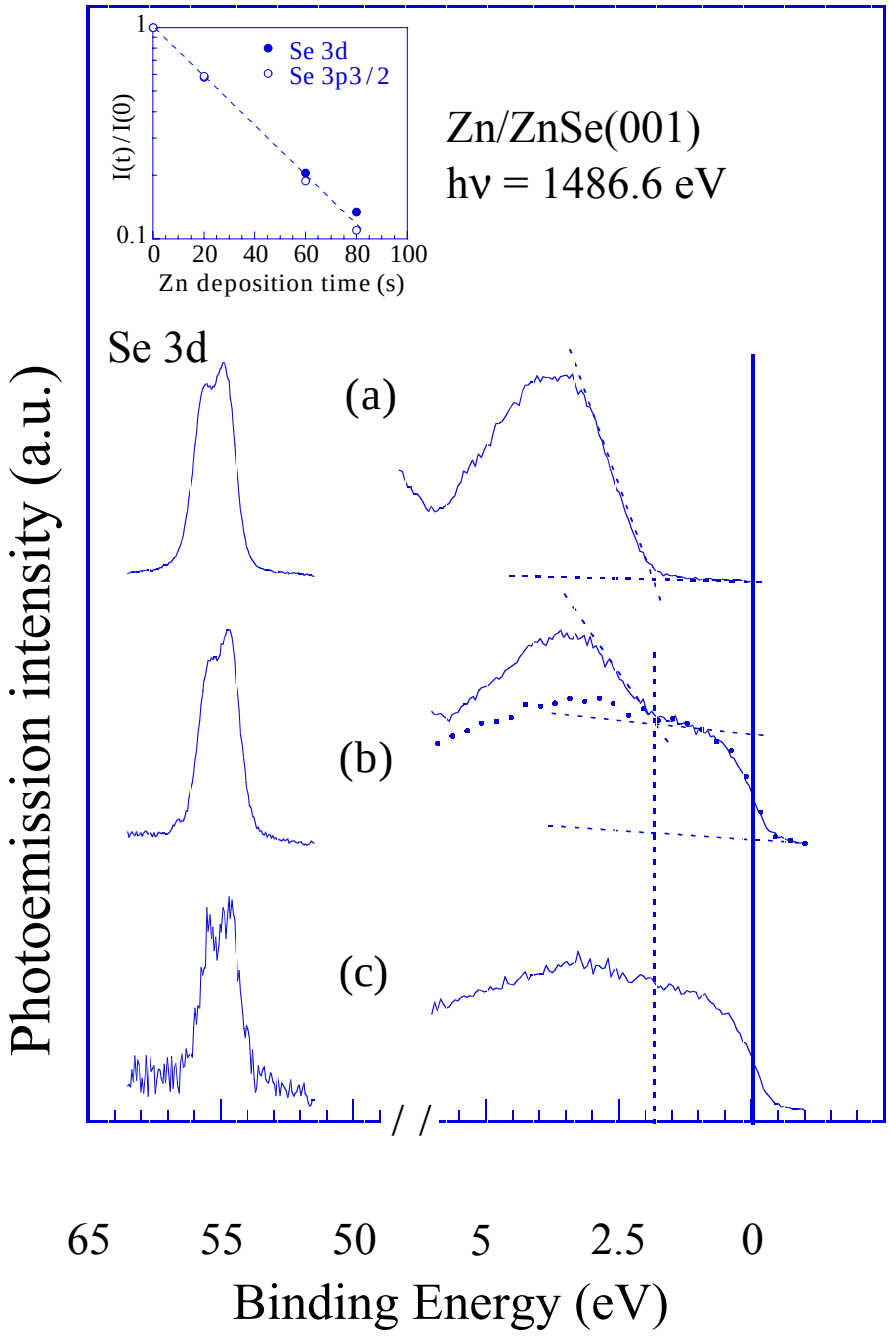

FIG. 1 Inset: Se 3d and Se2p$_{3/2}$ integrated photoemission intensity as a function of Zn deposition time during Zn deposition on ZnSe(001)2×1 surfaces at room temperature. (a)Se 3d (left) and valence band photoemission (right) from a ZnSe(001)2×1 surface prior to Zn deposition. (b)Se 3d and valence band photoemission following deposition of 2.4 nm of Zn. (c) Se 3d and valence band photoemission following deposition of 4.0 nm of Zn. The zero of the energy scale corresponds to the Fermi level E_F of the spectrometer. At intermediate coverages the valence band emission can be reproduced as a superposition of bulk-like ZnSe (dashed line) and metallic Zn (solid circles) contributions.

From the ZnSe valence band emission in Fig. 1(a) and a least-squares linear extrapolation of the leading edge (see dashed line), we determined the valence band maximum E_v, and the position of the Se 3d centroid relative to E_v (53.24±0.03 eV). The valence band emission in Fig. 1(c) is indistinguishable from that of bulk Zn, with a well-defined Fermi level cutoff with energy width consistent with the experimental resolution, as expected, since at a coverage of 4.0 nm the Se 3d core intensity is reduced to less than 7% of the initial emission intensity. The substrate valence band emission scales accordingly, and is therefore negligible in Fig. 1(c).

At all intermediate coverages our results consistently showed that the valence band emission can be reproduced by a superposition of a bulk-like ZnSe emission and a bulk-Zn emission, shifted by a suitable energy relative to each other. This is exemplified in Fig. 1(b), where the dotted line shows the overlayer bulk-like Zn emission, and the dashed line shows the leading valence band edge of the substrate bulk-like ZnSe emission. This is consistent with the expected, ideal unreactive behaviour of Zn/ZnSe(001) interfaces, and allowed us to read directly the energy separation between E_F and E_v in Fig. 1(b), i.e., the p-type Schottky barrier height ϕ_p=1.86±0.07 eV.

The more conventional approach to Schottky barrier measurements monitors the position of substrate core levels unaffected by interface chemistry as a function of metal coverage to infer the position of the valence band maximum E_v. Using to this purpose the measured Se 3d binding energy of 53.24±0.03 eV relative to E_v, in Fig. 1(b) we would determine ϕ_p=1.82±0.07 eV, consistent with the result of the previous determination.

The method of directly reading the band alignment by reproducing the overall valence band emission as a superposition of bulk-like substrate and overlayer emissions is only suitable for ideal unreactive interfaces, such as Zn/ZnSe(001), and at overlayer thicknesses comparable with the escape depth. Whenever it could be applied to the Zn/ZnSe(001) case, it confirmed the values obtained using the Se 3d core doublet. At relatively low and high Zn coverages, as compared to the escape depth, only the latter method could be applied.

There is substantial evidence in the literature that the initial semiconductor surface reconstruction may influence the final value of the Schottky barrier height.[104,105] For ZnSe interfaces, Chen et al. have reported a 0.25-eV reduction in ϕ_p for Au/ZnSe(001) junctions

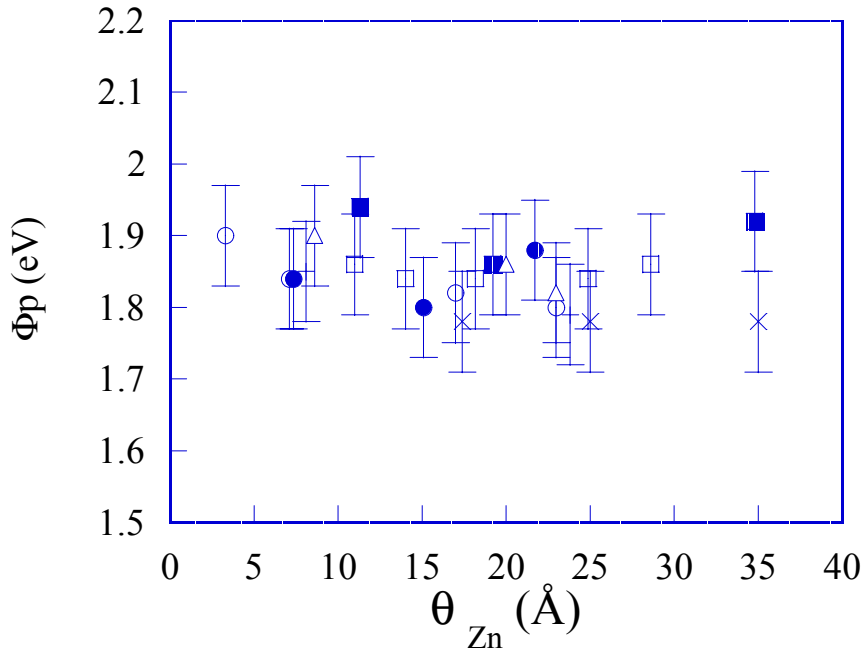

FIG. 2 XPS-determined values of the p-type Schottky barrier height ϕ_p as a function of Zn coverage θ for Zn/ZnSe junctions fabricated by Zn deposition on initial c(2×2) (crosses), 2×1 (open symbols), and 1×1 (solid symbols) ZnSe(001) surface reconstructions. Different symbol shapes correspond to different experimental runs.

fabricated on the 1×1, as opposed to the 2×1 surface reconstruction.[117] Lazzarino et al. recently found a 0.24-eV p-type barrier reduction when comparing Al/ZnSe(001) interfaces fabricated on ZnSe(001)1×1 surfaces to those fabricated on c(2×2) and 2×1 surfaces.[112] This effect was associated with a local interface dipole created mainly by charge transfer from the first metal monolayer to the excess Se atoms at the interface, with the a large relaxation in the Se-Se interatomic distances at the interface playing a major role in determining the value of the local dipole moment.[112]

Using the Schottky model, some tunability of the Schottky barrier height could be envisioned also for Zn/ZnSe(001). The work function of Zn metal is Φ_M = 4.33 eV.[118] For ZnSe(001), an electron affinity χ of 3.51 eV has been reported for the c(2×2) surface.[119] Chen et al. have observed an increase of 0.15 in the electron affinity when going from the c(2×2) to the 2×1 and a decrease of 0.25 eV when going from the c(2×2) to the 1×1 surface.[117] From the Schottky model, the p-type Schottky barrier height can be expressed as $\phi_p = E_g-(\Phi_M-\chi)$, where E_g is the ZnSe bandgap of ~2.70 eV. This would yield ϕ_p=1.88, 2.03, and 1.63 eV for interfaces fabricated on c(2×2), 2×1, and 1×1 and surfaces, respectively.

We therefore repeated the type of studies summarized in Fig. 1 on interfaces fabricated through Zn deposition at room temperature on ZnSe(001)c(2×2) and ZnSe(001)1×1 surfaces. Both types of interfaces showed an ideal unreactive behaviour consistent with that exhibited by Zn/ZnSe(001)2×1 interfaces. For the three types of interface, XPS determinations of the p-type Schottky barrier height through the valence band and Se 3d core level methods at different overlayer coverages are summarized in Fig. 2. Crosses, open symbols, and solid symbols denote results obtained following Zn deposition on ZnSe(001) c(2×2), 2×1, 1×1, and surfaces, respectively. Different symbol shapes correspond to different experimental runs, and the vertical error bars reflect the overall experimental uncertainty of ±0.07 eV. The resulting, XPS-determined best values of the p-type Schottky barrier heights were ϕ_p=1.78±0.07, 1.85±0.07, and 1.86±0.07 eV for the three types of interfaces. Such values are consistent with one another within the XPS experimental uncertainty.

To improve the accuracy in the determination of the barrier height and gauge the ideality of the corresponding junctions, I-V and C-V measurements were performed at 300 K on selected junctions. Representative I-V characteristics are shown in Fig. 3, where open circles, solid squares, and solid circles correspond to junctions fabricated through Zn deposition on ZnSe(001) c(2×2), 2×1, and 1×1 surfaces, respectively. The corresponding numerical values of the n-type Schottky barrier height ϕ_n and ideality factor *n* were ϕ_n=0.82±0.02, 0.82±0.02, and 0.83±0.02 eV, and n=1.07±0.01, 1.07±0.01, and 1.06±0.01, respectively, for the three interfaces.[120] C-V measurements on the same samples (not shown), yielded only slightly higher values of the n-type barriers, i.e., ϕ_n=0.87±0.02, 0.86±0.02, and 0.89±0.02 eV, respectively.

The transport results clearly rule out any Schottky barrier tunability. Taking $\phi_n \sim E_c - E_F \sim E_g - \phi_p$, where E_c is the conduction band minimum in ZnSe, from the C-V transport values we would infer p-type barrier heights ϕ_p~1.83±0.02, 1.84±0.02, and 1.81±0.02 eV, respectively, for interfaces fabricated on c(2×2), 2×1, and 1×1 surfaces. Within the combined transport and XPS experimental uncertainties, such barrier heights are fully consistent with the results of the XPS studies in Fig. 2.

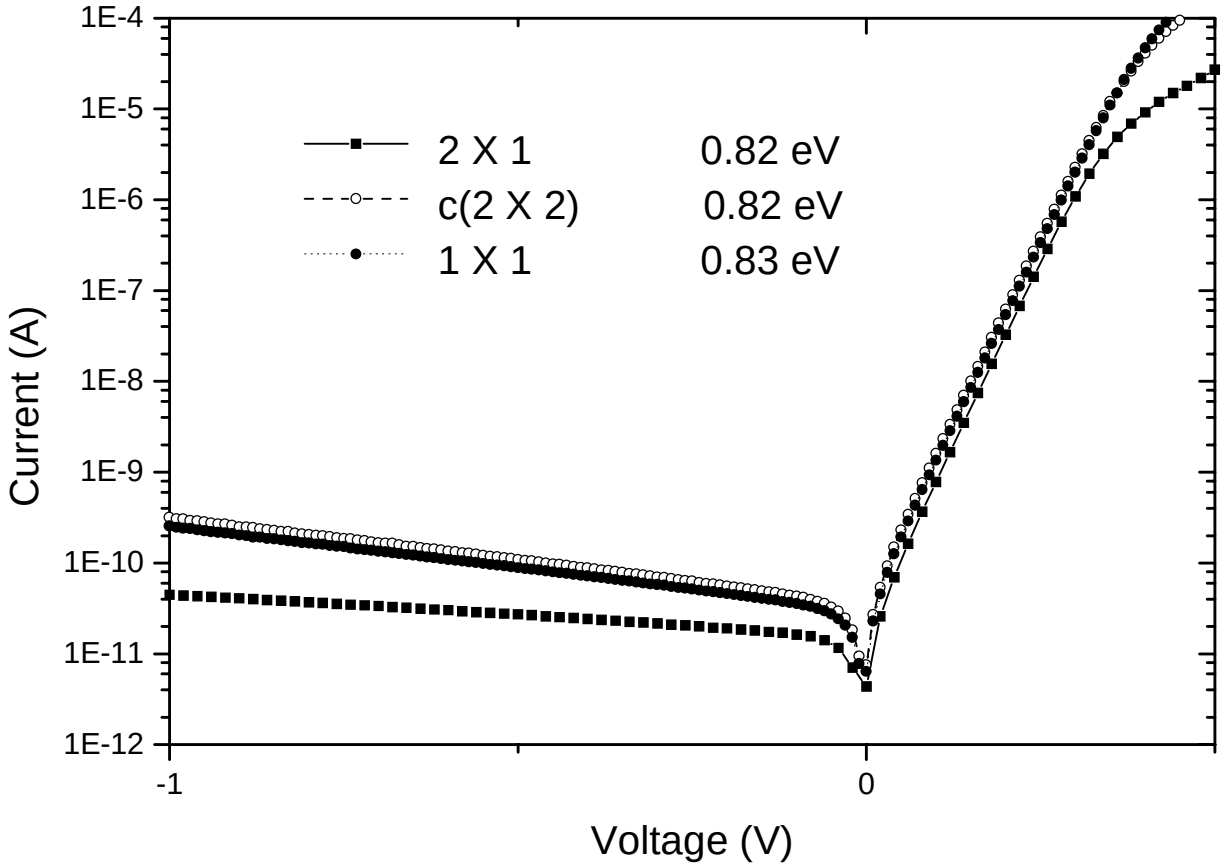

FIG. 3 Current-voltage characteristics for Zn/ZnSe junctions fabricated by Zn deposition on initial c(2×2) (open symbols), 2×1 (solid squares), and 1×1 (solid circles) ZnSe(001) surface reconstructions. The corresponding values of the n-type Schottky barrier height ϕ_n and ideality factor n are also shown.

In summary, both XPS and transport studies consistently show that the Schottky barrier height for ideal unreactive Zn/ZnSe(001) interfaces is independent of the initial reconstruction and composition of the ZnSe surface, in sharp contrast with the behaviour exhibited by Au/ZnSe(001) and Al/ZnSe(001) junctions. A possible explanation is that that the local interfacial configurations responsible for Schottky barrier tuning in Al/ZnSe(001) and Au/ZnSe(001) junctions correspond to more similar Schottky barrier heights in Zn/ZnSe(001). Alternatively, such configurations might simply not occur, i.e., be unstable for Zn/ZnSe(001) junctions. Calculations allowed us to discriminate between these two explanations.

6.4. Theoretical methods

The calculations were performed within the local-density approximation (LDA) to density functional theory (DFT), using the nonlocal pseudopotentials by Stumpf et al.[121] and a plane-wave basis set. We used a 30 Ry kinetic-energy cutoff for the plane-wave expansion of the electronic orbitals, and the exchange-correlation potential was taken from the work of Ceperley and Alder.[122] A nonlinear core correction was used for Zn.[123]

Isolated Zn/ZnSe(001) interfaces were simulated using a slab geometry in supercells characterized by 17 semiconductor layers and 13 metal layers. We obtained epitaxial Zn/ZnSe(001) contacts by constraining the Zn atoms on fcc - as opposed to hcp - lattice sites. The Zn [001] axis was made parallel to the ZnSe [001] growth axis, and the Zn fcc lattice was rotated by 45° about the [001] axis relative to the cubic substrate in order to satisfy the epitaxial condition $a_{//}=a_{ZnSe}/\sqrt{2}$, where $a_{//}$ is the Zn in-plane lattice constant.

A similar epitaxial geometry has been employed to simulate Al/GaAs(001) and Al/ZnSe(001) interfaces,[112,124] and is known to give rise to experimentally observed pseudomorphic structures, at least in the case of Al/GaAs(001).[125,126] In the case of Al contacts to GaAs and ZnSe, the in-plane lattice misfit is about 1% ($\sqrt{2}\, a_{Al}>a_{ZnSe}$). The atomic radius in a twofold coordinated metal structure (r_{12}=1.39 Å) is 3% smaller than that of Al (r_{12}=1.43 Å), and one therefore expects a 1.9% in-plane tensile strain ($\sqrt{2}\, a_{Zn}>a_{ZnSe}$) for Zn overlayer in pseudomorphic Zn/ZnSe(001) junctions.

The macroscopic elastic deformation of the Zn(001) overlayer was determined by minimizing the total energy of a bulk Zn fcc metal with respect to the lattice parameter $a_{\perp}$ along the [001] growth direction, with constraint: $a_{//}=a_{ZnSe}/\sqrt{2}$. We used the theoretical equilibrium lattice parameter a_{ZnSe}=5.46Å (the experimental value is 5.67). The calculations were performed in a 4-atom tetragonal unit cell, using a (6,6,2) Monkhorst-Pack grid for the Brillouin zone integration. The resulting lattice constant of the Zn overlayer along the growth direction was $a_{\perp}$=3.44Å. Our calculated equilibrium lattice constant for Zn is a_{Zn}=3.67Å, which means that the overlayer contracts by 6%. We emphasize that this should be considered as an upper bound, as

the polarisation of the Zn-3d electrons –not included here- is expected to increase both the Zn and the ZnSe lattice constant, with larger increase for Zn.

Along the lines of recent studies of Al/GaAs(001) and Al/ZnSe(001) junctions,[111,127,128] our interface geometries were generated by selecting simple atomic configurations that would give an ideal continuation of the semiconductor bulk, while taking into account the initial composition of the starting surface. The structures that we will refer to as unrelaxed in the following include only the macroscopic elastic deformation of the Zn overlayer, with no atomic relaxation at the interface. For these systems, we used as interplanar spacing across the metal-semiconductor interface the average of the interlayer spacings in the metal and in the semiconductor.

To evaluate the atomic relaxation at the interfaces, we first considered metal/semiconductor structures with a thin Zn overlayer in contact with vacuum. The initial configuration prior to relaxation were generated by removing 5 atomic layers from the middle of the Zn slab in supercells containing the unrelaxed Zn/ZnSe structures. The atomic configurations were then fully relaxed, by incorporating the Hellmann-Feyman forces in a gradient procedure to minimize the total energy with respect to the ionic positions. Due to the presence of the vacuum, the metallic overlayer could freely relax along the growth direction, and release any residual stress in the system. To examine the properties of the fully developed junctions, we incorporated then the resulting interplanar distances in a new supercell including a full Zn slab (13 layers of Zn). The interlayer spacings for the additional layers at the centre of the Zn slab were set to $a_{\perp}/2$. We then let this structure relax again to allow for small readjustments in the metal. The supercell calculations for the metal/semiconductor structures were performed using a (6,6,2) Monkhorst-Pack grid for reciprocal-space integrations, and a Gaussian broadening scheme with a full width at half maximum (FWHM) of 0.1 eV was used to take into account the partial filling of the bands.[129]

The p-type Schottky barrier height was written as:[130]

$$\phi_p = \Delta E_p + \Delta V \qquad (1)$$

where ΔE_P is the difference between the Fermi level E_F of the metal and the valence band maximum E_v of the semiconductor, each referenced to the average electrostatic potential of the corresponding crystal, and ΔV is the potential-energy lineup across the interface. The ΔE_P term was obtained from band structure calculations for bulk, strained, fcc Zn and bulk ZnSe, using (16,16,16) and (8,8,8) Monkhorst-Pack grids to evaluate the charge density in the metal and in the semiconductor, respectively. The ΔV term was derived from the self-consistent supercell charge density via Poisson's equation, using the planar and macroscopic averaging techniques.[120] ΔV is the only contribution to ϕ_p which is interface-specific, and will depend, in general, on the atomic configuration established at the interface.

The values of ϕ_p calculated in the LDA framework were corrected to take into account many-body and relativistic effects. As discussed elsewhere,[112,124] ΔV should be accurately described by LDA-DFT, but ΔE_P may vary substantially, mainly because of relativistic and self-energy corrections to the LDA band structure of ZnSe. Along the lines described in Ref. 112, we incorporated spin-orbit (–0.15 eV) and many-body (+0.50 eV) corrections to the position of E_v, resulting in an overall +0.35 eV increase in the p-type Schottky barrier ϕ_p relative to the LDA values. Because of the way the above correction was estimated,[112] it carries a substantial uncertainly, of the order of 0.2 eV. However, since it is a bulk-dependent correction, identical for the different interface configurations examined, it will not affect the *variations* in barrier height from one configuration to another. The estimated uncertainty for such variations is therefore of the order of the numerical accuracy of the LDA calculations, i.e., about 50 meV.

6.5. Theoretical results

The simple starting atomic configurations selected for the calculations of the Zn/ZnSe(001) interface properties are illustrated in Fig. 4, prior to any atomic relaxation. As in Ref. 112, such configurations were chosen in order to give an ideal continuation of the semiconductor bulk while taking into account the initial composition of the starting surface.

For Zn overlayers fabricated on the c(2×2) surface we positioned the Zn atoms at the Zn vacancy sites of the outermost semiconductor layer. This results in a full layer of Zn atoms at the

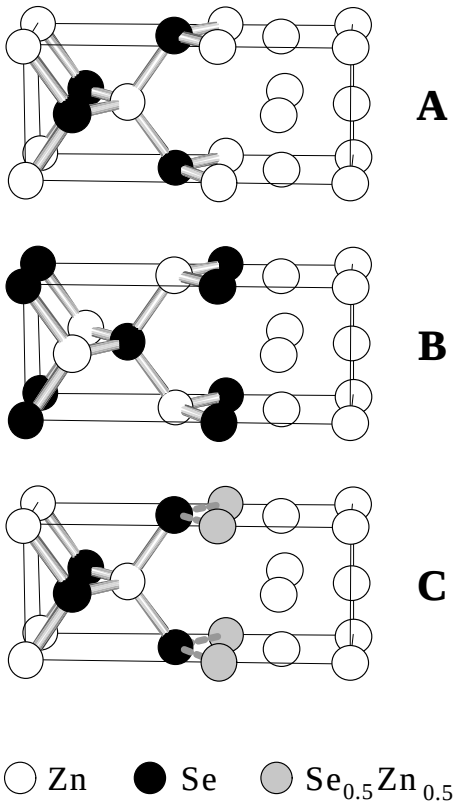

FIG. 4 Initial Zn/ZnSe(001) interfacial configurations employed in the supercell calculations, prior to atomic relaxation. Configuration A involves Zn atoms positioned at the Zn vacancy sites of the c(2×2) surface, below the Zn fcc lattice rotated 45° about the [100] axis relative to ZnSe to satisfy the epitaxial relation. Configuration B involves a ZnSe surface terminated by a full Se monolayer below the fcc metal. Configuration C involves a ZnSe surface terminated by a 50% Se-50% Zn atomic layer on top of a full Se monolayer.

ideal zincblende position below the first fcc atomic layer of metallic Zn (see configuration A in

Fig. 4). For Zn overlayers deposited on the 2×1 surface we terminated the semiconductor with a full layer of Se atoms at the ideal bulk zincblende positions and put the Zn atoms in the next layer on ideal fcc sites (configuration B).

For Zn overlayers fabricated on the 1×1 surface, we used a virtual crystal approach to terminate the semiconductor with a 50% Se-50% Zn atomic layer (see shaded symbols in Fig. 4) on top of the Se(001) subsurface layer (configuration C). The 50-50 composition was selected because the excess Se coverage at our 1×1 surfaces relative to the 2×1 surface was determined as about 0.5 ML.[112]

The starting metal-semiconductor interplanar spacing -in the [001] direction- across the interface was taken in all cases as the average of the interlayer spacing in ZnSe and fcc Zn. Atomic relaxation following energy minimisation typically involved three atomic layers across the interface, with maximum relaxation amounting as much as 10, 38, and 25% for the configurations A, B and C respectively in the direction perpendicular to interface.

In Fig. 5 we show the macroscopic average of the electrostatic potential V across the interface for the configurations examined, after full atomic relaxation. The relaxed positions of the different (001) atomic planes are illustrated by the atomic symbols below each electrostatic potential profile. The horizontal dashed lines in Fig. 5 are used to illustrate the calculated electrostatic potential lineup ΔV across the three Zn/ZnSe(001) interfaces. We caution the reader that the negative sign has been omitted from ΔV in Fig. 4 for clarity, and that the calculated values are -0.57, -0.44 and -0.74 eV, respectively, for configurations A, B, and C.

The LDA values of the Schottky barrier height can be obtained form Eq. (1) using the above values of ΔV and the calculated LDA value of the band-structure term ΔE_p=1.92 eV. For configurations A, B and C we obtained LDA p-type Schottky barrier heights of 1.35, 1.48, and 1.18 eV, respectively. Finally, by adding the combined relativistic and many-body correction of +0.35 eV, we estimated ϕ_p= 1.70, 1.83 and 1.53 eV for the three configurations examined.

The predicted variations in barrier height are much larger than the experimental uncertainty in the transport and XPS determinations of the barrier height. Therefore the three types of configurations which were used to explain the Schottky-barrier tunability in

Al/ZnSe(001) junctions,[112] if implemented in Zn/ZnSe(001), should give rise to clearly detectable differences in the Schottky barrier height, in contrast with the experimental results in Figs. 2-3.

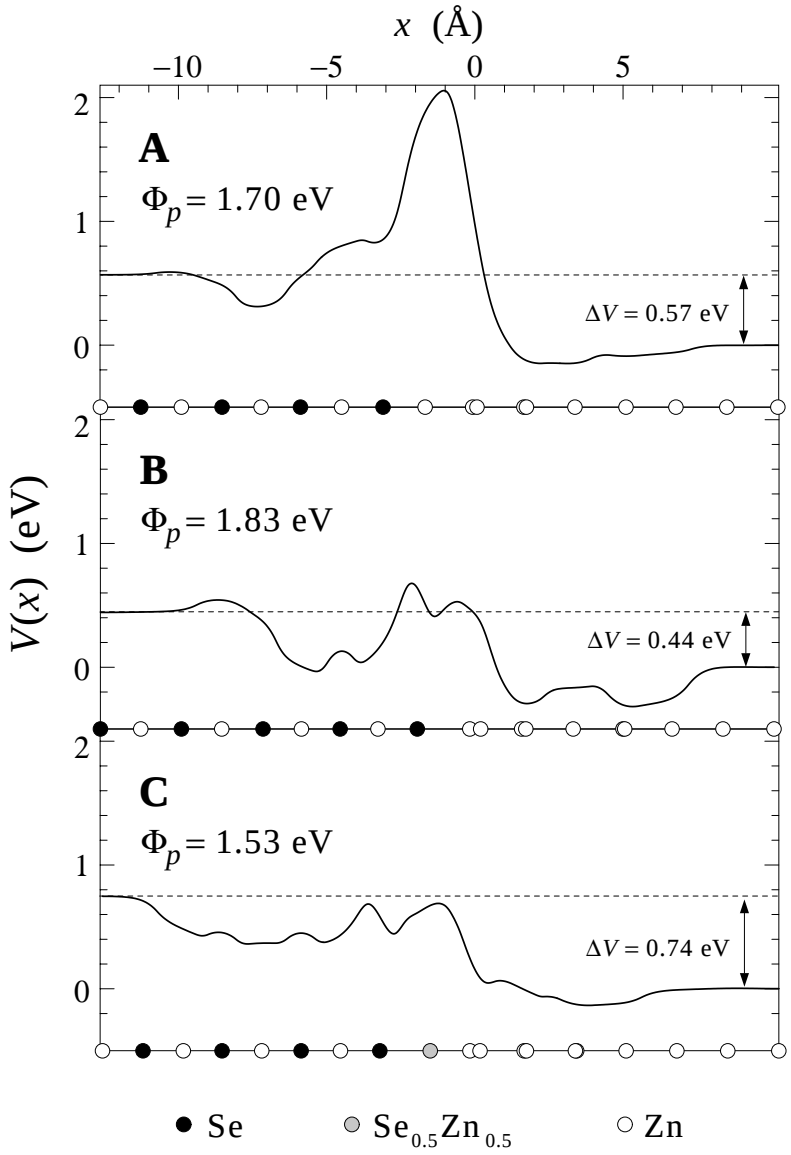

FIG. 5 Macroscopic average of the electrostatic potential energy V and potential energy lineup ΔV across the relaxed Zn/ZnSe(001) junctions. Relaxation is graphically illustrated at the bottom for each atomic plane. Double atomic symbols denote inequivalent relaxation at different sites. The calculated values of ϕ_p are also shown.

As to the absolute values of the calculated barrier heights, the large uncertainty carried by the many-body correction complicates comparison with experiment. Since the experimentally observed p-type Schottky barrier value in Figs. 2-3 remains at about 1.85 eV irrespective of the initial reconstruction of the ZnSe(001) surface, predictions for both configurations B and A would be consistent with experiment. Finally, we note that the calculated trend in the barrier height is qualitatively consistent with the estimates derived from the Schottky model, which predicted a 0.15 and 0.40 eV decrease in the p-type barrier for c(2×2) and 1×1 surfaces relative to 2×1 surfaces.

The formation energies E_f of the three Zn/ZnSe(001) interface configurations examined were calculated as:

$$E_f = \frac{1}{2}\left(E_{tot} - \sum_i n_i \mu_i \right) \qquad (2)$$

where E_{tot} is the calculated total energy of the supercell, n_{i} and μ_{i} are the number of atoms and the chemical potential for each atomic species *i* in the supercell, and the 1/2 factor takes into account that there are two equivalent interfaces within the supercell. In a generic B/AC metal/semiconductor junctions, there would be three atomic species and therefore three chemical potentials to contend with.

The chemical potential μ_B and $\mu_{AC}=\mu_A+\mu_C$ can be obtained from the calculated total energy of the corresponding bulk materials, but this is not enough to specify all three of the *atomic* chemical potentials in Eq. (2). Because the supercell contains a different number of A and C atoms, the interface formation energy would depend linearly on the isolated A or C chemical potential. For a general B/AC interface, therefore, the relative stability of the different interfacial configurations depends on the isolated anion (or cation) chemical potential, which, in turns, should be influenced by the experimental conditions. This very argument has been recently used to explain how the relative stability of As- and Ga-terminated Al/GaAs(001) and Al/Si/GaAs(001) interfaces could be determined by the growth conditions,[107,131] and account for the wide experimental tunability of the corresponding Schottky-barrier heights.[132,133,134]

In Zn/ZnSe(001), as for any other common-cation metal/semiconductor junction, the situation is intrinsically different. The chemical potentials μ_{Zn} and $\mu_{ZnSe}=\mu_{Zn}+\mu_{Se}$ can be determined from the calculated total energies of bulk, strained fcc Zn and bulk ZnSe, respectively, and in thermodynamic equilibrium conditions they are sufficient to univocally define the interface formation energy in Eq. (2).

For the relaxed configurations A and B interface formation energies of 0.53 and 0.62 eV, respectively, per interface atom were obtained. Although for the absolute values of our formation energies we estimated an uncertainty as 0.2 eV per interface atom, *variations* in the formation energy between two configurations carry an uncertainty of only 0.01 eV per interface atom. The implication is that configuration A is significantly more stable than configuration B.

Configuration C is of special interest, since for Al/ZnSe and Au/ZnSe interfaces fabricated on the ZnSe(001)1×1 surfaces, charge transfer to the excess Se atoms at the interface has been associated with an important reduction of the p-type Schottky-barrier height.[109,112] And a reduction in ϕ_P is also observed in Fig. 5 when comparing the configuration C with configurations A and B. The corresponding calculated interface formation energy, however, is 1.90 eV per interface atom. The more than threefold increase in interface formation energy relative to the other two interfaces, makes it exceedingly unlikely that this interface would ever be encountered in practice.

We caution the reader that the above configurations were obtained from simple, ideal continuations of the semiconductor bulk starting from *different initial compositions* of the ZnSe surface. They should not be interpreted as three possible evolutions of the same *initial* surface configuration. Therefore, even based solely on thermodynamics, and neglecting kinetic effects, strictly speaking one cannot conclude that configurations B and C will not form because they have higher formation energies than configuration A.

On the other hand, the calculated interface formation energies do capture the eminently reasonable trend that Se-rich semiconductor terminations are unlikely to remain stable under Zn deposition even at room temperature, and that the presence of a Zn flux during overlayer fabrication prevents the tunability of the interfacial configurations and of the Schottky barrier associated with the variable cation (or anion) chemical potential during interface fabrication.

6.6. Conclusions

Zn/ZnSe(001) metal/semiconductor junctions exhibit ideal unreactive properties, with layer-by-layer growth and no detectable atomic interdiffusion. Transport and photoemission measurements indicate a p-type Schottky barrier height of 1.85 eV, independent of the growth conditions and of the initial reconstruction and composition of the ZnSe(001) surface within experimental uncertainty. This is in contrast with the reported behaviour of Au/ZnSe(001)[109] and Al/ZnSe(001) contacts, that exhibited markedly lower p-type Schottky barriers heights for interfaces fabricated on the metastable, Se-rich 1×1 surface.

The absence of any observable tunability of the Schottky barrier for Zn/ZnSe(001) is consistent with the calculated formation enthalpies of model interface configurations, that suggest that all Se-rich semiconductor terminations are unlikely to remain stable, and that the presence of a Zn flux during overlayer fabrication prevents the tunability of the local atomic configurations associated with the variable cation (or anion) chemical potential.

For such ideal interface systems, the predictions of the Schottky model are quantitatively consistent with experiment, and qualitatively consistent with the trends of first-principles calculations.

Chapter seven: Au/Zn/ZnSe: Schottky barrier tuning

7.1. Introduction

Au/ZnSe is one of the most studied metal/ZnSe interfaces. The work function of gold is 5.1 eV[118] while the electron affinity of ZnSe (001) has been reported to vary from 3.25 to 3.65 eV depending on the ZnSe surface reconstruction.[109,110,119] An estimate of the Au/ZnSe Schottky barrier height using the Schottky model would therefore lead to a p-type Schottky barrier around 1 eV. This is one of the lowest values expected for metals on p-type ZnSe, not too different from those of other high work function metals such as Pd, Ni, which exhibit a work function of 5.12eV,[118] 5.15eV[118] and only slightly higher than Pt, which exhibit a work function of 5.59 eV.[118] Even if the low p-dopability of ZnSe (< $1x10^{18}$ cm^{-3})[16,135] has hindered the use of Au as direct contact metal to ZnSe in practical devices,[18,20] the technological importance of contacts on ZnSe has stimulated a number of investigations of Au/ZnSe junctions by several authors.[109,110,119,136,137,138,139,140,141,142]

One of the first photoemission study of Au/ZnSe(100) contacts, by Xu et al.[119], reported an Au/ZnSe p-type (n-type) Schottky value of 1.25±0.1 eV (1.45±0.1 eV). The data were obtained by means of ultraviolet photoemission spectroscopy (UPS) using ZnSe (001) samples grown by MBE ex-situ and transferred in air to the UPS spectrometer. Prior to Au deposition the surface was prepared by Ar^+ sputtering and annealing at 400 °C to eliminate surface contaminants and produce a c(2x2) reconstruction, as determined by low-energy electron diffraction. The same authors measured an electron affinity of 3.51±0.1 eV for the (001)-c(2x2) surface. After Au deposition (< 15Å) Xu et al. reported that epilayer growth was 2D, with no substrate disruption. No long-range order was detected by low-energy electron diffraction (LEED).

Chen et al.[109] performed a photoemission study of Au/ZnSe junctions as a function of the initial ZnSe surface reconstructions prior to Au deposition.[117] ZnSe (001) layers were grown by

MBE, and protected with a Se cap layer during transfer in air to the analysis chamber. The Se cap layer was then thermally desorbed to obtain a 1x1 Se rich reconstruction at 150 ºC, a 2x1 reconstruction at 300 ºC or a c(2x2) reconstruction above 400 ºC. The authors report a p-type (n-type) SB of 1.14±0.1 eV (1.56±0.1 eV) following Au deposition on 2x1 and c(2x2) surfaces, while a 0.25eV reduction in the p-type barrier was observed for the 1x1 reconstruction. On all surfaces, Chen et al. reported, based on photoemission investigations, an ideally unreactive behaviour during Au/ZnSe junction formation, i.e., the interfaces were found to be abrupt, with no evidence of chemical reaction.

Despite the reported unreactive behaviour of Au/ZnSe interface, transport studies of Au/ZnSe yielded a surprisingly wide range of n-type SB values from 0.90 eV to 2.1 eV.[136,137,138,139,140,141,142]

Among the highest values reported are those by Tam et al.[142], who measured by standard dc current-voltage (I-V) measurements an n-SB height of 2 eV. Au was deposited on ZnSe crystals commercially afforded, after surface cleaning with a chemical solution of methanol with 1% of bromine. Lower values have been found, for example, by Marshall et al.[141], who reported n-type barrier heights of 1.35-1.40 eV, depending on the sample. The ZnSe layers were grown by MBE and air-exposed. Before metal evaporation, the sample surface was cleaned for 60 s in $HF:H_2O$ (1:30), and the Schottky barrier height was evaluated by standard I-V measurements. Koide et al.[139] observed a p-SB value of 1.23 eV (1.47 eV n-SB) by capacitance-voltage (C-V) measurements. The samples were grown by MBE and nitrogen doped to $\sim 1 \cdot 10^{18}$ cm^{-3}. Prior to ex situ Au evaporation, the native oxide on the ZnSe surface was removed by a chemical etch with saturated-bromine water.

Morgan et al.[138] studied Au/n-ZnSe contacts by means of ballistic electron emission microscopy (BEEM). MBE-grown ZnSe layers were protected with a Se cap layer during transfer in air to the Au deposition chamber. In spite of the presence of a Se cap layer, the authors, before loading the sample in the evaporation chamber, rinsed the samples with methanol. The Se cap layer was then subsequently removed upon heating to ~300 °C in the Au deposition chamber and a substantial carbon contamination was observed by Auger spectroscopy. A layer of 20Å of Au was finally deposited in situ. Morgan et al. found an average n-SB value of 1.37 eV, with a

distribution of Schottky barrier heights varying from 1.32 to 1.43 eV, values which have been obtained when sampling different 210nm wide regions. They found lateral inhomogeneities in the Schottky barrier height already on a scale of 3-10 nm.

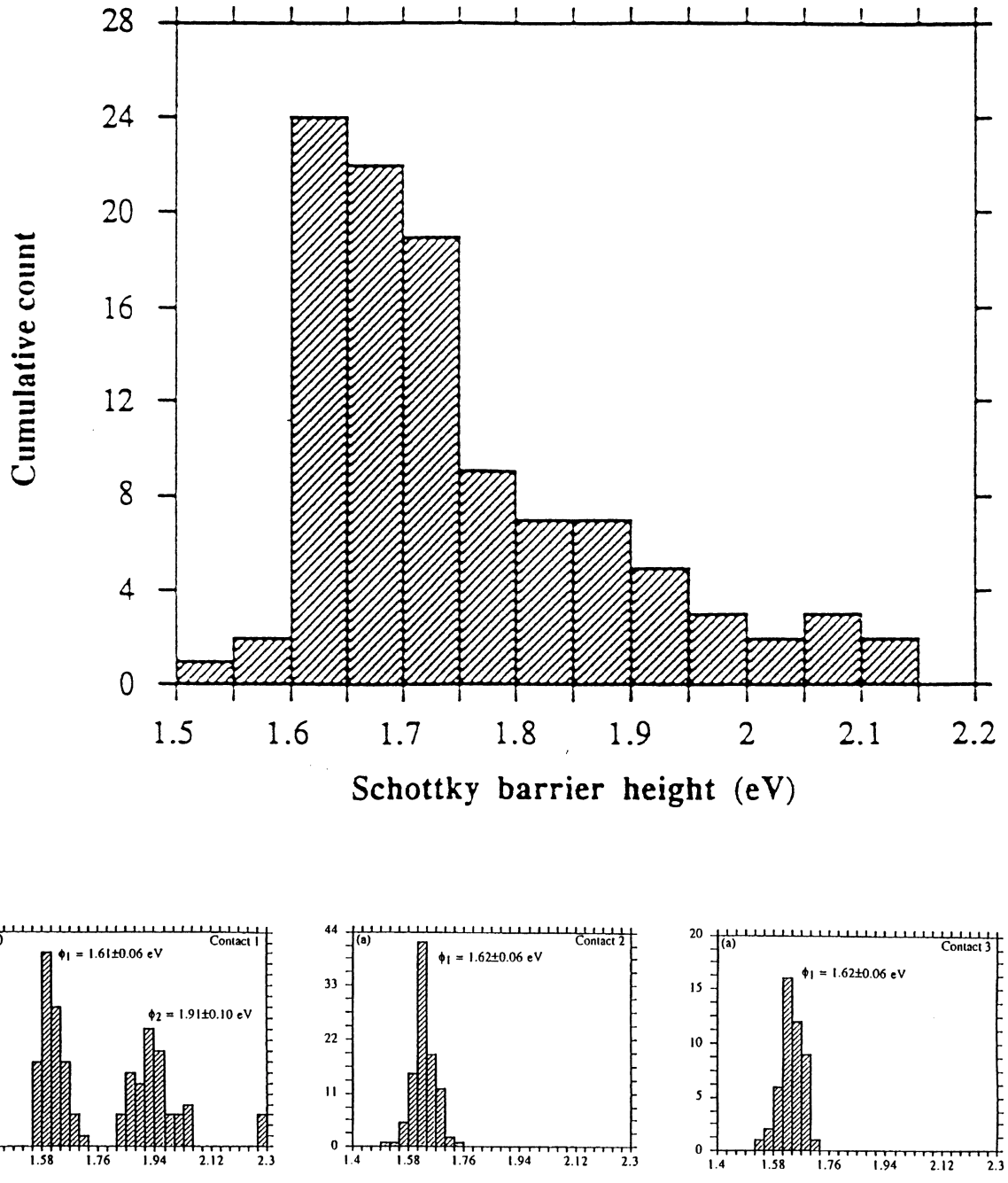

FIG. 1 Top: Histogram of the Schottky barrier heights deduced from more than 100 BEEM spectra on Au/ZnSe, taken on several points on the same sample, reported by Coratger et al.[137]. The wide distribution presents a maximum at about 1.65 eV, and the Schottky-barrier height ranges from 1.53 to 2.15 eV. Bottom: barrier heights measured with BEEM spectroscopy for three different Au/ZnSe diodes on the same wafer, reported by Coratger et al.[136]. Note the presence of barrier heights at 1.61±0.06 and 1.91±0.06 eV

A wider range of Au/ZnSe n-Schottky barrier values was observed by Coratger et al.[137]. Fig. 1 (top) shows some of the results. The initial ZnSe substrates were grown by MBE ex-situ and etched with a solution of NaOH and $Na_2S_2O_3$, prior to insertion in the UHV chamber and metal deposition. The BEEM spectra show SB heights ranging from 1.53 to 2.15 eV. The distribution is highly asymmetric and shows a maximum around 1.65 eV. The histogram was obtained by measuring several local barrier heights within a range of several micrometers, while lateral inhomogeneities were on a 10-20 nm scale. The bottom part of the figure shows results by some of the same authors,[136] from three different circular diodes lithographically defined on the sample surface. Sample preparation was the same described in the previous paper. The diodes had a diameter of the order of 0.5 mm and a number were previously examined by I-V technique. In particular the I-V results for the n-type barrier height were 0.9, 1.32, 1.45 and 1.65 eV. Only three of the diodes were chosen for BEEM analysis, and no description of the criterion of choice was given. For each diode the actually sampled area was about 200x200 nm^2. They found two distinct SB values, one at ~1.62 eV, and one at ~1.91 eV. Lateral inhomogeneities were found in the same range as in Ref. 137.

Evidence of large lateral inhomogeneities in the Au/ZnSe Schottky barrier height, and the wide range of Schottky barrier heights observed by different methods, are surprising for an interface which has been reported to be ideally unreactive. A major difficulty in comparing BEEM, I-V, C-V and photoemission results, however, is the widely different sample preparation methods employed by the different authors. We therefore elected to conduct new photoemission, I-V and C-V experiments on Au/ZnSe (001) junctions fabricated in-situ by MBE. Using lithographic techniques to fabricate diodes of different sizes, we also addressed the issue of the lateral homogeneity of the barrier height by systematic transport measurements. Our results point to a major role of an hitherto unreported interface reactivity of the Au/ZnSe junction. Finally, we explored the possibility of controlling interface reactivity and the Schottky barrier height through local modification of the metallurgical interface. In particular, we fabricated ultrathin Zn interlayer in the interface region of Au/ZnSe contacts.

7.2. Au/ZnSe

ZnSe epilayers 0.5 to 1 μm-thick were initially deposited by MBE at 290°C on GaAs(001) 2X4 epitaxial substrates, with a typical growth rate of about 0.3 μm/h, with a Zn/Se beam pressure ratio (BPR) of 0.4 and a Se-terminated 2x1surface reconstruction, as monitored by RHEED.

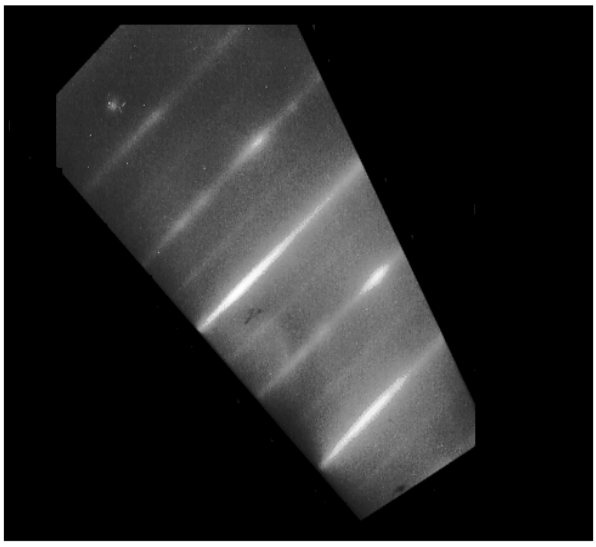

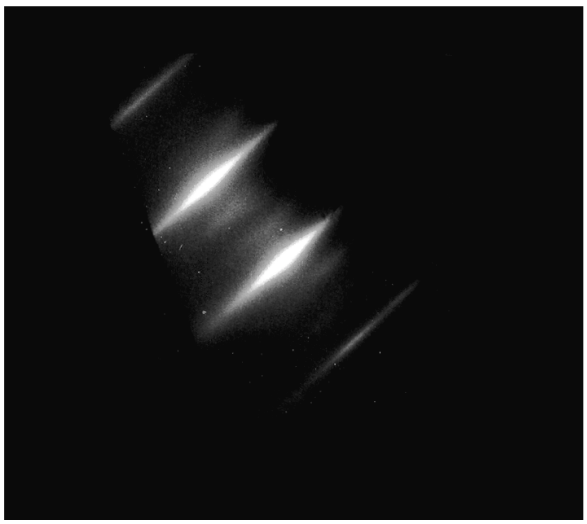

FIG. 2 2x3 RHEED pattern after room temperature deposition of 100Å of gold on ZnSe (2x1).

Substrates fabricated for XPS studies included ZnSe epilayers undoped, or doped with Cl from a $ZnCl_2$ source at variable levels in the n=3x10^{16} to 1x10^{18} cm^{-3} range. Substrates fabricated for I-V measurements were similar to those employed for the Zn/ZnSe studies (see Chapter 6), and included a ZnSe epilayer with a graded doping profile, tailored in order to obtain a 300 nm-thick n^+ layer (~4x10^{18} cm^{-3}) near the interface with the GaAs substrate to decrease the series

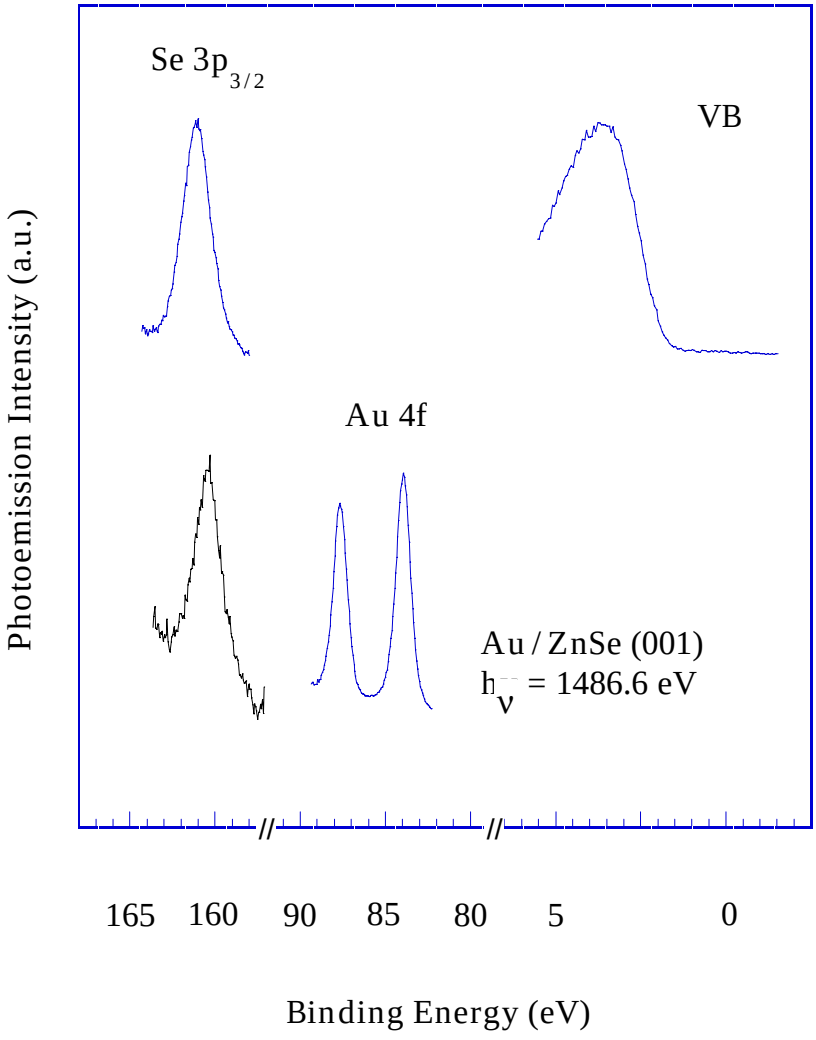

FIG. 3 Topmost section: energy distribution curves for the emission from the Se $3p_{3/2}$ core levels and the leading valence band edge from the 2×1 ZnSe surface, prior to Au deposition. The zero of the energy scale corresponds to the Fermi level of the system. A linear extrapolation of the leading edge of the ZnSe valence band was used to determine the valence band maximum E_V. The resulting Se $3p_{3/2}$ binding energy relative to E_V was 159.26±0.06 eV. Lower section: Se $3p_{3/2}$ and Au 4f emission after in situ deposition of 25Å of Au. The Schottky barrier height was determined by the Se $3p_{3/2}$ emission position relative to the Fermi level after Au deposition. The resulting p-type (n-type) Schottky barrier was 1.08±0.06 eV (1.62±0.06 eV). Au 4f were used to strictly monitor the Fermi level position.

resistance due to the ZnSe/GaAs heterojunction. Comparatively lower doping ($3x10^{16}$ to $1x10^{17}$ cm^{-3}) was employed within a 500 nm-thick region at the interface with the metal.

After ZnSe growth, the sample was cooled down to room temperature and an elemental Au flux from an effusion cell was used to deposit elemental Au in the metallization chamber. A thickness monitor located at the sample position in the metallization chamber was used to calibrate the gold deposition rate. Typical growth rates for Au were ~0.06 Å/s and the effusion cell was operated at temperatures of about 1300 ºC. Metal overlayer for XPS studies were typically 1 to 3 nm-thick, while samples for I-V measurements included 30 to 50-nm thick metal overlayers. During Au evaporation the sample was at a distance of about 20 cm far from the orifice of the Knudsen cell. Radiative heating from the cell, as determined by means of a thermocouple mounted on the sample holder, raised the sample temperature from room temperature to an equilibrium temperature of 60 °C in about 15 minutes.

For I-V analysis a final Au layer was deposited *ex-situ* to aid the photolithographic process. Circular mesas with diameter in the 50-400 μm range were fabricated by photolithographic techniques to define the top contacts. The selective etchant for gold was 0.4M $K_3Fe(CN)_6$, 0.2M KCN and 0.1M KOH water solution. Indium was used to fabricate the back contacts. More details about the lithographic process, the I-V, and C-V measurement techniques can be found in the previous two chapters.

Upon Au deposition onto the ZnSe(001) 2x1 surface a weak RHEED pattern initially showed superposition of line patterns with different orientations. Increasing the Au coverage above 45-50 Å, however, resulted in the emergence of a 2x3 RHEED pattern, which became increasingly streaky with increasing coverage. Representative patterns are shown in Fig. 2. To our knowledge this is the first report of an epitaxial relation between Au overlayers and ZnSe. Epitaxy of Au on ZnSe is not surprising in view of the small difference in lattice parameter between Au, ZnSe and GaAs and of the reported epitaxy of Au on GaAs.[143] Still, epitaxy has not been observed by other authors.[109,110,119] We suggest that the mixed reconstruction observed at low Au coverage and the late emergence (above 40-50Å) of a well defined 3x2 pattern might be a possible explanation. In fact previous reports on Au/ZnSe junctions fabricated in situ, investigated Au overlayers on ZnSe below 30Å in thickness.[109,110,119] At such a thickness no clear

RHEED pattern can be detected. We caution the reader, however, that the sample temperature during Au deposition in our system was not strictly room temperature, but rather in the 20-60 °C range. This could have had a positive influence on Au epitaxy on ZnSe.

Representative XPS measurements are shown in Fig. 3. In the topmost section we show energy distribution curves for the emission from the Se $3p_{3/2}$ core levels and the leading valence band edge from the 2×1 ZnSe surface, prior to Au deposition. The zero of the energy scale corresponds to the Fermi level of the system. A linear extrapolation of the leading edge of the ZnSe valence band was used to determine the valence band maximum E_V, and the resulting Se $3p_{3/2}$ binding energy relative to E_V was 159.26±0.06 eV. In the lower section of Fig. 3 we show the Se $3p_{3/2}$ and Au 4f emission after in situ deposition of 25Å of Au. The Schottky barrier height was determined from the Se $3p_{3/2}$ position relative to the Fermi level following Au deposition. The resulting p-type (n-type) Schottky barrier height was 1.08±0.06 eV (1.62±0.06 eV). The reason for using the anion Se $3p_{3/2}$ as opposed to Se 3d to monitor the barrier height was motivated by the superposition of the Au $5p_{3/2}$ core emission with the Se 3d signal.

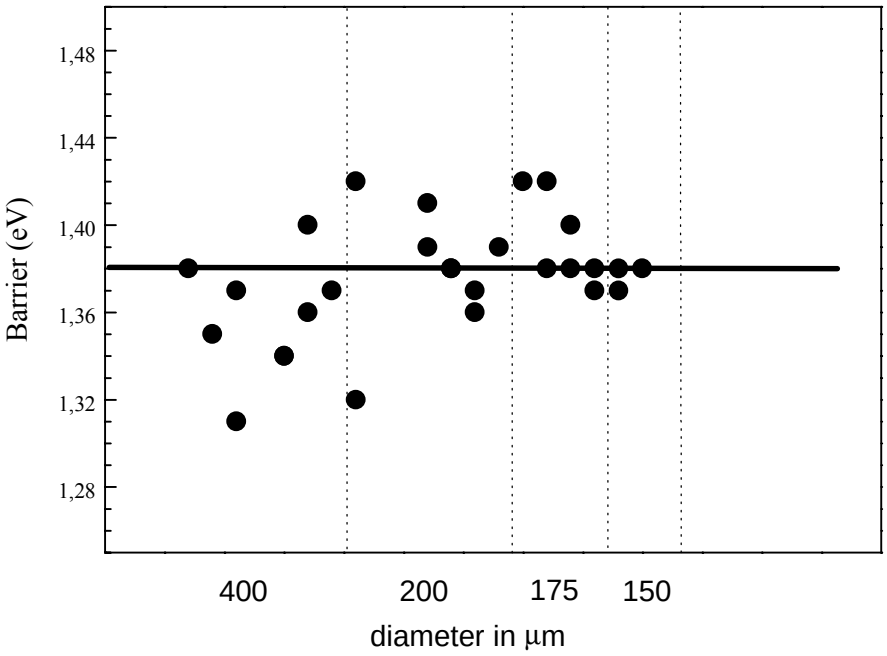

FIG. 4 Barrier height values for Au/ZnSe diodes plotted for various dot diameters, showing a scatter of the order of ± 0.06 eV around 1.38 eV. Barrier height values have been obtained by I-V measurements, and corrected by taking into account the image force lowering effects.

I-V and C-V measurements of the Au/n-ZnSe (001) barrier height were also performed at 300 K on selected junctions. Fig 4 shows the n-type barrier height for Au/ZnSe diodes of different diameter. A scatter of the order of ± 0.06 eV about the average n-type barrier height of 1.38 eV is clearly observed for the larger diodes examined. The scatter is much reduced when diodes of 150 μm in diameter are examined. The corresponding average value of the barrier height as determined from C-V measurements on a subset of diodes was 1.64 eV (not shown), in very good agreement with the XPS results (1.62±0.06 eV). Differences between I-V and C-V results are often found in the literature. Even after correction for image-force barrier lowering and tunneling across the barrier[105,114,144] C-V results tend to be somewhat higher than I-V determinations.[105,144] This has been ascribed to the different sensitivity of the two techniques to local inhomogeneities in the contact region. I-V measurements are strongly affected by inhomogeneities, even on the nanometer scale, corresponding to lower Schottky barrier heights, while C-V measurements are mostly unaffected.[144,145] Photoemission spectroscopy is also a space-averaging technique relatively insensitive to local microscopic inhomogeneities, and is expected to show a better agreement with C-V determinations of the barrier height.[105]

The scattering in the I-V determinations of the barrier height in Fig. 4 is only 0.06 eV, i.e., much smaller than the spread of transport values (0.9-2.0 eV) that can be found in the literature.[136,137,139,142] This supports our contention that the different ex-situ sample preparation procedures employed by the different authors produce different contaminants and defects on the surface, and that the measured barrier height is influenced by the different composition and structure of the interface. The scattering of ± 0.06 eV observed for junctions fabricated by MBE in situ (Fig. 4) is still larger than the experimental uncertainty of ± 0.01 eV on the single diode determination, and is comparable to that reported by Morgan et al.[138] and Marshall et al.[141]. Since the larger diodes are most affected, and I-V measurements weight preferentially local variations in barrier height, we suggest that local surface defects, spaced by more than about 150 μm, might explain the residual scatter observed in Fig. 4. Since inhomogeneities in the barrier height are in general, somewhat difficult to reconcile with the picture of Au/ZnSe as ideal, unreactive interfaces, we elected to use XPS to further probe the chemistry of the interface.

In the topmost section of Fig. 5 we show the evolution of the Zn $2p_{3/2}$ position relative to the Fermi level of the spectrometer as a function of gold thickness onto the ZnSe (001) 2x1 surface. The long-dashed line shows the Zn $2p_{3/2}$ position in metallic zinc,[146,147] while the short-dashed line indicates the expected position of the Zn $2p_{3/2}$ peak in an ideally unreactive Au/ZnSe junction, based on the XPS-determined value of the Schottky barrier height (see Fig. 3). In the lower section of Fig. 5 we show the integrated intensity of Zn $2p_{3/2}$ core emission as a function of overlayer thickness. The intensities are plotted as ln[I(t)/I(0)], where I denotes the integrated core emission intensity after background subtraction, t the overlayer thickness in Ångströms and I(0) denotes the initial substrate emission prior to Au deposition. The leftmost dashed line shows the expected ideal attenuation behaviour of the Zn $2p_{3/2}$ in the absence of any interdiffusion, with a slope consistent with the 6 Å effective escape depth.[73,148] The horizontal dashed line is only a guide to the eye through the relatively constant values of the Zn $2p_{3/2}$ intensity for overlayer thickness above 50/60Å.

In the high-coverage limit, the observed constant intensity of the Zn $2p_{3/2}$ with coverage, and the apparent binding energy of the Zn core levels, consistent with a metallic environment,[146] indicates the presence of segregated Zn atoms in the metallic overlayer, possibly near the surface. This is a behaviour often encountered in *reactive* metal/ZnSe interfaces,[105] where cations displaced in the early stages of interface formation are found to segregate at the metal-overlayer surface.

Exchange reactions between overlayer atoms and semiconductor cations are usually associated with the enthalpy of formation of overlayer-anion compounds and the alloying enthalpy of overlayer atoms and semiconductor cations. In the case of Au-ZnSe the corresponding thermodynamic quantities are -0.15 and -0.66 eV/atom.[149] Since the resulting interface heat of reaction[105] of –0.15-0.66=-0.81 eV/atom is lower than the heat of formation of ZnSe (-1.69 eV/atom)[149], Au-Zn exchange reactions should be unlikely at defect-free surfaces. A possible explanation, consistent with the relatively small number of cations displaced is that reactions take place only at suitable lattice sites such as steps and kinks, where the formation enthalpy is reduced relative to the bulk. We caution the reader, however, that the thermodynamic considerations discussed above neglect entropic contributions. Analogous considerations, when

supplied to Au/Si (111), Au/GaAs, and other Au/semiconductor interfaces,[150] would predict no reactions, while extensive intermixing has been observed in all those interfaces.[150]

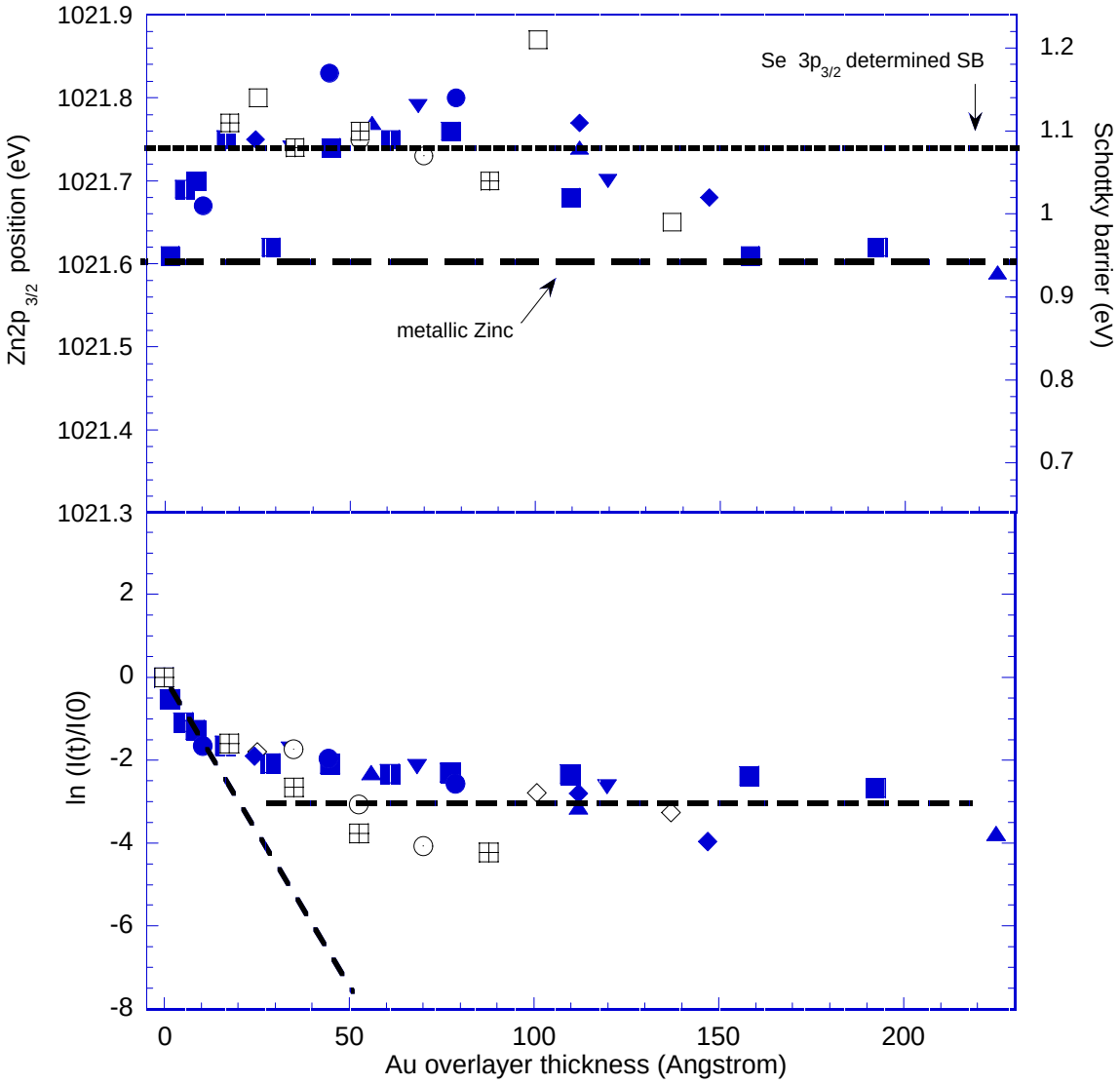

FIG. 5 Top: Zn $2p_{3/2}$ position respect to the Fermi level as a function of Au overlayer thickness. The right hand scale shows the Schottky barrier value if evaluated from the Zn $2p_{3/2}$ position. Long-dashed line: the Zn $2p_{3/2}$ position in metallic Zinc.[146,147] Short-dashed line: expected position of Zn $2p_{3/2}$ peak in an ideal unreactive Au/ZnSe junction, based on the XPS-determined value of the SB. Lower section: integrated intensity of Zn $2p_{3/2}$ core emission as a function of overlayer thickness. The intensities are plotted as ln[I(t)/I(0)], where I denotes the integrated core emission intensity after background subtraction, t the overlayer thickness in Ångström and I(0) denotes the initial substrate emission prior to overlayer deposition. The leftmost dashed line shows the expected ideal attenuation behaviour of Zn $2p_{3/2}$ in the absence of any interdiffusion, with a slope consistent with the 6 Å effective escape depth.[73,148] The horizontal dashed line is only a guide to the eye through the relatively constant values of Zn $2p_{3/2}$ intensity for overlayer thickness above 60Å.

Different phenomena characterize the 20-80 Å intermediate coverage range in Fig. 5. The apparent Zn $2p_{3/2}$ binding energy is consistent with the position expected from bulk ZnSe, given the observed band bending and Schottky barrier height. This indicates that emission from the substrate still dominates over that of the segregated Zn atoms. The Zn core intensity, however, is much larger than expected from the ideal, exponential attenuation in the case of layer-by-layer growth. Both trends and the slow emergence of a single RHEED pattern in this coverage range, could be consistent with a Stranski-Krastanov growth mode for the Au overlayer on ZnSe. The presence of relatively large 3D islands separated by terraces where only monolayer Au coverage are present, would be expected to give rise to a lower Zn attenuation than predicted from a layer-by-layer growth and a Zn position pinned at the SB extrapolated value. Preliminary AFM observations confirm the existence of 3D structure in this coverage range. Coalescence of the 3D islands to yield a more homogeneous growth film occurs in the 50-100Å range, and is accompanied by an increasingly well defined RHEED pattern and a relatively abrupt disappearance of the substrate related Zn core emission. The residual Zn emission reflects at this point only the segregated Zn atoms in the overlayer.

In the low-coverage range in Fig. 5 the position of Zn $2p_{3/2}$ core levels reaches that expected from the measured value of the Schottky barrier height at a coverage of about 15Å. Such an evolution is in agreement with that reported by Vos et al.[110] and Chen et al.[109] based on ultraviolet and soft x-ray spectroscopy data, and such slow build-up of the Schottky barrier could be consistent with a non-uniform coverage of the semiconductor surface. Nevertheless, at a coverage of 15-20 Å the position of the core levels is definitely consistent with the equilibrium Schottky height, while the Zn core level intensity already shows important deviations from the ideal layer-by-layer attenuation. The latter indicates that exchange reactions which displace Zn atoms from selected surface sites have already occurred, and therefore that such events accompany the establishment of the equilibrium barrier height. The somewhat increased FWHM of the Zn core level at such coverages (not shown) also suggests that the segregated Zn atoms give rise to an unresolved low-binding-energy contribution to the overall Zn 2p lineshape.

To further test the possibility that exchange reactions at selected surface sites are responsible for the observed lateral inhomogeneities in the Au/ZnSe barrier height, we exploited

the ideally unreactive nature of the Zn/ZnSe junction (see Chapter 6) and fabricated Zn interlayers in the interface region of Au/ZnSe contacts.

7.3. Au/Zn/ZnSe(2x1)

Zn interlayers were deposited at room temperature on ZnSe (001) 2x1 surfaces following the experimental procedures described in the previous chapter. In particular, Zn deposition

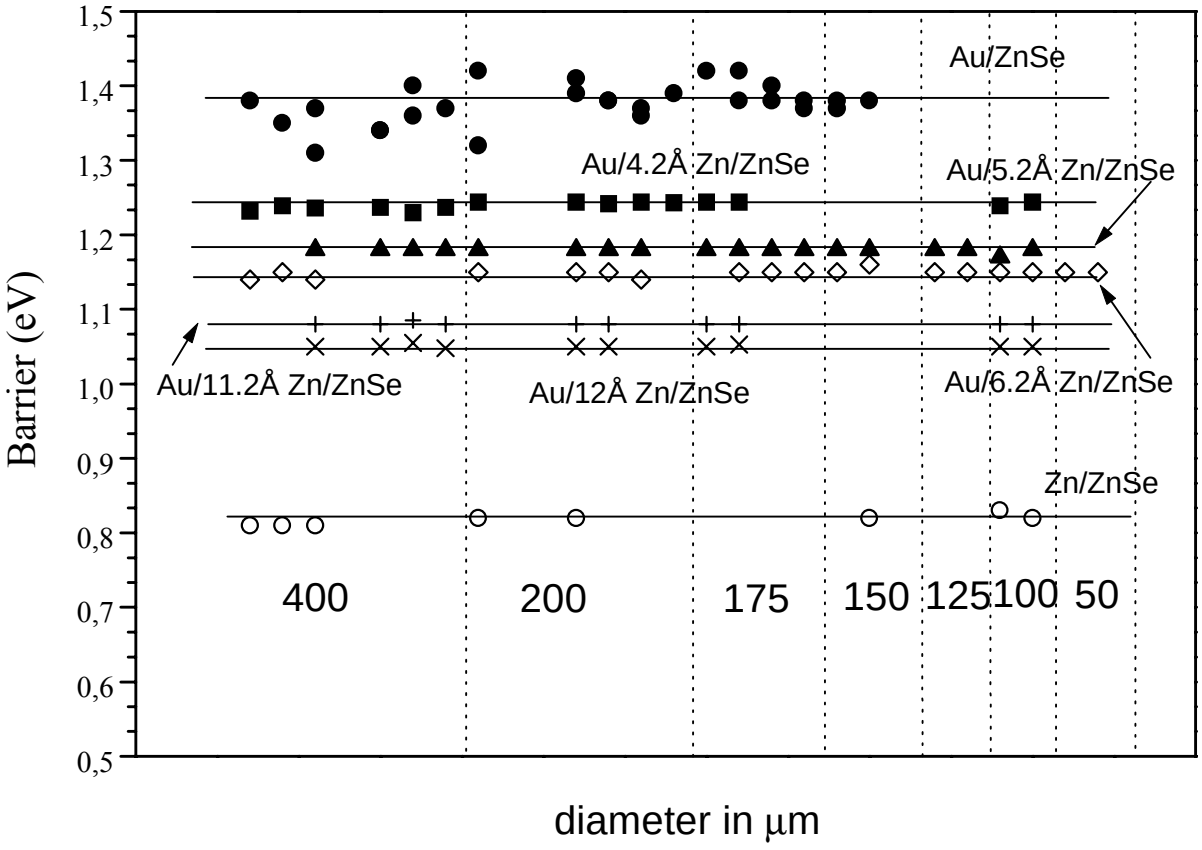

FIG. 6 Comparison of barrier heights for Au/ZnSe, Au/Zn/ZnSe and Zn/ZnSe diodes plotted for various dot diameters. Barrier height values have been corrected by taking into account the image force lowering effects. Data are plotted as follows: Au/ZnSe: open circle; Au/4.5Å Zn/ZnSe: solid square; Au/5.2Å Zn/ZnSe: solid triangle; Au/6.2Å Zn/ZnSe: open diamond; Au/11.2Å Zn/ZnSe: plus sign; Au/12Å Zn/ZnSe: cross sign; Zn/ZnSe: open circles. The presence of a Zn interlayer definitely improved the lateral homogeneity of the diodes.

occurred in the II-VI chamber, with Zn thickness determined from flux calibration. The sample was then transferred in ultra-high-vacuum to the metallization chamber where Au deposition was performed following the procedures described in the previous section. The RHEED pattern following Au deposition was of polycrystalline type for Zn interlayers thicknesses larger than 3/4 Å, and somewhat similar to that of Au/ZnSe for lower Zn interlayer thicknesses. Diodes of different sizes were fabricated onto the resulting Au/Zn/ZnSe junctions to sample the lateral homogeneity of the barrier height through I-V and C-V techniques. Data as a function of Zn interlayer thickness were recorded to probe the effect of the local Zn-induced modification of the interface environment on the Schottky barrier height.

Fig. 6 summarizes the I-V data after correction for image force barrier lowering effects. Different symbols denote different thickness of the Zn interlayers. Solid lines through the data show the average value of the n-type Schottky barrier height.

We also included in Fig. 6 for comparison data of Au/ZnSe junctions (solid circles) already shown in Fig. 4, and data for Zn/ZnSe junctions (open circles) already discussed in the previous chapter. While Au/ZnSe junctions showed, especially for the larger diode diameters, a ±0.06 eV scatter in the Schottky barrier height about the average value of 1.38 eV (solid circles), insertion of a 0.42 nm-thick Zn interlayers yields a laterally homogeneous barrier, within an experimental uncertainty of ±0.01 eV, and a n-type barrier height of 1.24±0.01 eV. Increasing the Zn interlayer thickness to 0.52, 0.62, 1.12 and 1.20 nm, yields a further monotonic reduction in the n-type barrier height, and laterally homogeneous interfaces, within experimental uncertainties. The corresponding average barrier heights in Fig. 6 were 1.18, 1.15, 1.08 and 1.05 eV. We also performed systematic C-V measurements on the same diodes, which yielded n-type barrier heights of 1.43, 1.32, 1.18, 1.1, and 1.09 eV respectively. We note that while in the case of Au/ZnSe there is a difference of about 260 meV between I-V and C-V measurements, this difference is progressively reduced with increasing Zn interlayer thickness and saturates (above 6Å) to about the value observed for Zn/ZnSe interfaces (~30/40 meV).

The reduced scattering in the I-V data and the improved agreement between I-V and C-V measurements, suggest that the suppression of the Au/ZnSe reactions, which results from the fabrication of an unreactive Zn interlayer at the interface, eliminates the lateral inhomogeneities in the Au/ZnSe barrier height. This supports our contention that the Au/ZnSe exchange reactions at selected surface sites during the early stages of Au/ZnSe interface formation are responsible for the observed lateral inhomogeneities in the barrier height. Clearly, the scale of the lateral inhomogeneity probed in Fig. 6 is much larger than that probed by BEEM in Fig. 1, and future BEEM studies will have to address of the effect of the Zn interlayer on a more microscopic scale. A single, preliminary result is anticipated in Fig. 7, where we plot a distribution of BEEM results from a single Au/ZnSe sample with a Zn-rich interface. The results, obtained at the Technical University of Berlin in collaboration with Professor M. Dähne-Prietsch, are preliminary in the sense that no quantitative information on the amount of Zn present at the Au/ZnSe interface could

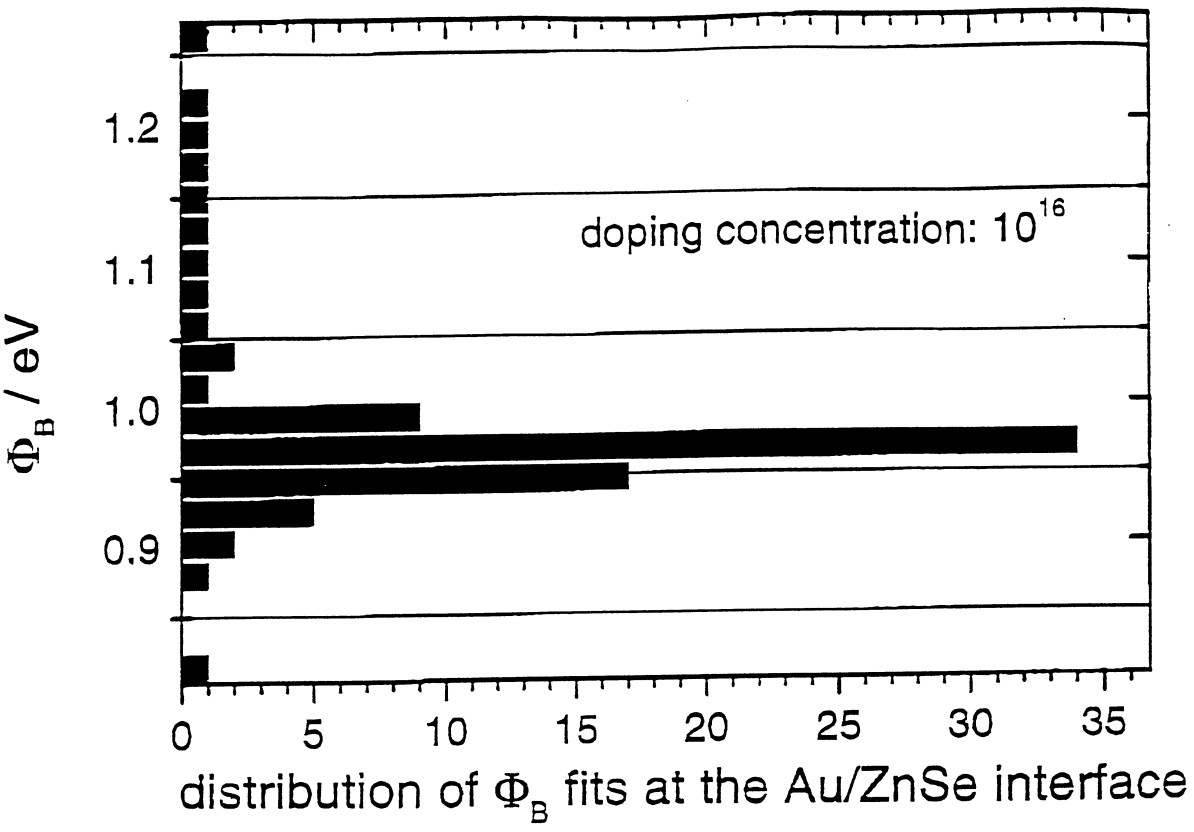

FIG. 7 Preliminary BEEM study, by Professor M. Dähne-Prietsch. No quantitative information on the amount of Zn present at the Au/ZnSe interface could be obtained.

be obtained. Nevertheless the qualitative indications are quite clear, the presence of a Zn interlayer at the Au/ZnSe interface yields a narrow distribution of barrier values (±0.04 eV)in Fig. 7 about the average n-type Schottky barrier height (0.96 eV in Fig. 7).

The systematics depicted in Fig. 6-7 also indicates that Zn interlayers may be used to tune the Au/ZnSe barrier height, i.e., that a local modification of the interface environment can be used to control the transport properties of Au/ZnSe contacts. An intriguing issue is raised by the observed dependence on the Schottky barrier height on the thickness of the Zn interlayer. The progressive reduction of the Au/ZnSe n-type barrier height with increasing interlayer thickness and the minimum barrier height of about 1.0 eV are somewhat unexpected from the point of view of an ideal Schottky picture of barrier formation. One would have rather expected a relative abrupt change in barrier height from 1.38 eV (the Au/ZnSe value) to 0.82 eV (the Zn/ZnSe value) upon completion of a full Zn monolayer on top of the ZnSe surface. Two effects might explain the observed deviation from such a prediction. First, the slower evolution of the barrier height towards the Zn/ZnSe value may reflect a slower evolution of the surface work function towards the Zn value. Second, Zn/Au alloying effects might explain both the slower change in the barrier height and the incomplete convergence to the Zn/ZnSe value for the thickest interlayers examined.

The first mechanism might be expected to lead to an average Au/Zn work function and Au/Zn/ZnSe barrier height which depends on the spatial extension of the Au- and Zn-related metallic wavefunctions, and of the related metal-induced gap states. These are, however, unlikely to exceed 3 to 5 Å, and should not play a significant role in the case of the thickest Zn interlayers examined. Some measure of Zn-Au alloying, on the other hand, would be qualitatively consistent with the alloying enthalpy of Zn atoms in Au of about -0.66 eV per atom,[149] and with the non negligible ~15% equilibrium solubility of Zn in fcc Au predicted by the Au-Zn binary phase diagram.[151]

We sought evidence of Au-Zn alloying in the valence and core photoemission spectra from the Au overlayer on Zn/ZnSe substrates. In Fig. 8 we show valence band photoemission spectra from an Au/Zn/ZnSe samples which include a 20Å Au overlayer and an 8Å Zn interlayer (solid line), and a 20Å Au overlayer and an 11Å Zn interlayer. For comparison we also show a spectrum obtained from a 60Å Au overlayer directly deposited on ZnSe, which is representative of the bulk Au emission (dotted line). The region of the valence band selected in Fig. 8 includes the Fermi level, shown in the inset in an expanded scale, and the shallowest region of the 5d states, which is most affected by alloying. The result of the presence of a Zn interlayer of increasing thickness in Fig. 8 is a marked change in the lineshape of the crystal-field spilt shallower d bands, with an apparent narrowing of the related bandwidth, together with a

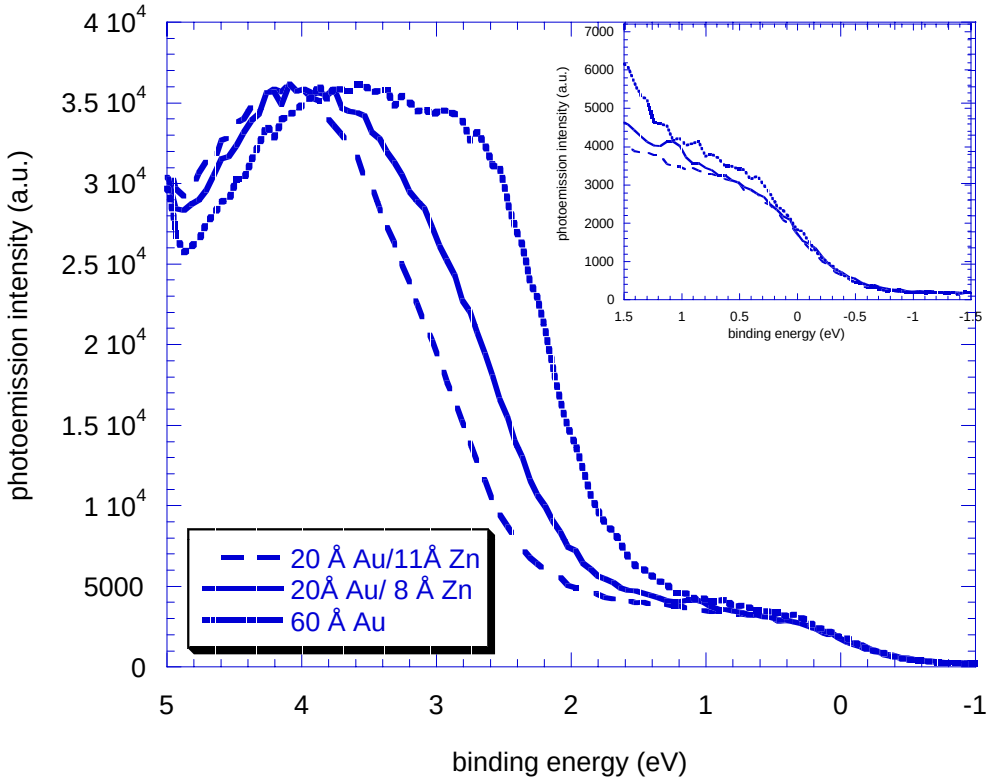

FIG. 8 Representative Fermi edges for three different samples with different Zn interlayer between Gold and ZnSe as measured by XPS. Spectra are normalized to same height. The dotted line is the Fermi edge of 60 Å of gold on ZnSe, while the continuous and the dashed line are the Fermi edges of 20Å of gold deposited on 8Å of Zn and 20Å of gold deposited on 11Å of Zn respectively. When a Zn interlayer is deposited a higher binding energy shift in the Au d *bands is found, characteristic of an alloy formation. The shift is smaller for higher Au/Zn ratios. Inset: Fermi level region in an expanded scale.*

progressive shift to higher binding energies. The Au 4f core level emission from the same three samples, shown in Fig. 9, shows a rigid shift to increasing binding energies, relative to Fermi level, with increasing Zn interlayer thickness. Both trends have been observed before whenever Au atoms have been intermixed or alloyed with elements whose valence bands were composed of sp electrons. The supportive photoemission systematics includes results for Au-Si,[152] Au-Sn,[153] Au-Cd,[154,155] Au-In,[154,155] Au-Sb,[154] Au-Te,[154] Au-Ga[155] and Au-Al.[156]

Such consistent general trends have been interpreted as reflecting a selective hybridisation of the shallowest (antibonding) 5d states, with comparative little effects on deeper Au 5d bonding states, which are more strongly hybridised with Au s electrons in the fcc structure. The effects on the deeper d states become evident only when the concentration of the sp element in the alloy is further increased. The shift to higher binding energy has been associated with a reduction of the d-d overlap between different Au atoms upon alloying, and to the consequent trend of the Au atoms to become more "atomic-like".[157]

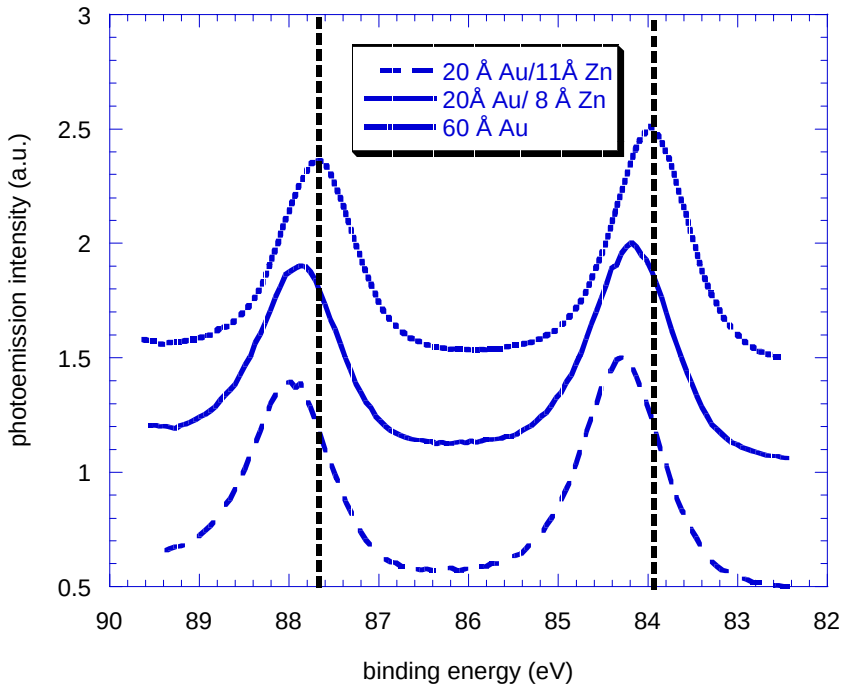

FIG. 9 Au 4f position respect to Fermi level in the same three different samples as in Fig. 6. Dotted line, continuous and dashed lines are respectively: 60 Å of gold on ZnSe, 20Å of gold deposited on 8Å of Zn and 20Å of gold deposited on 11Å of Zn. The higher the Zinc interlayer the higher the shift towards higher binding energies detected in the position of Au 4f peaks.

Our conclusion is that the results in Fig. 8-9 provide clear evidence of Au-Zn alloying, and that this may explain the detail of the systematic in the Au/Zn/ZnSe Schottky barrier height.

We conclude with two important words of caution. First, since alloying between the Au overlayer and Zn interlayer will be affected by deposition temperature and interlayer thickness, different sample preparations might lead to somewhat different Schottky barrier heights. Secondly, complete alloying of Au and Zn to form an homogeneous intermetallic overlayer is inconsistent with our results and cannot explain the observed modifications of the Schottky barrier height in Fig. 6. Both issues are addressed in Fig. 10, where we compare barrier heights determined by different techniques (XPS, I-V, and C-V) on different samples, as a function of Zn interlayer thickness. The samples for XPS studies included a 30Å Au overlayer, while samples for I-V and C-V measurements included 300-1000Å thick Au overlayers. For comparison we also

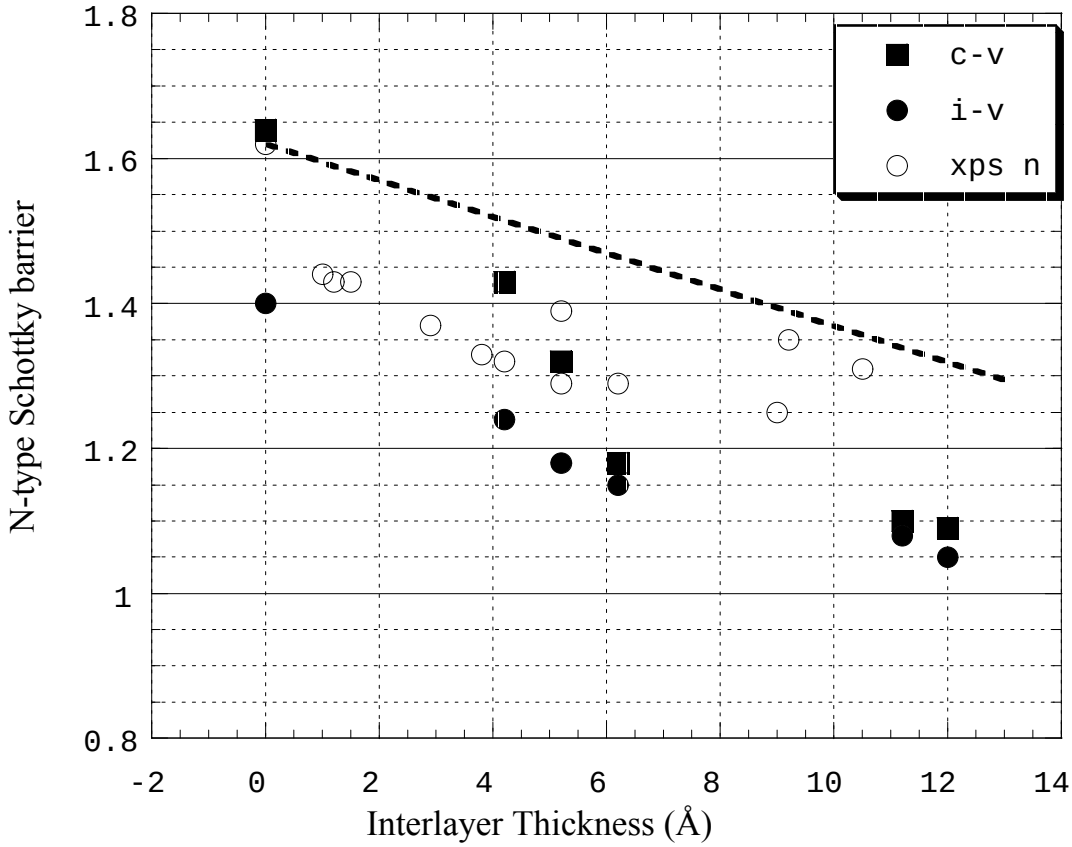

FIG. 10 n-type SB values as determined by XPS, I-V and C-V as a function of Zn interlayer thickness. The XPS values have been measured after 30Å gold deposition on the Zn/ZnSe surface. The dotted line is the XPS expected SB value in the occurrence of total alloying.

show (dashed line) the expected n-type barrier height from the XPS-type samples in the case of complete Au-Zn alloying. This was estimated by assuming that an $Au_{1-x}Zn_x$ homogeneous overlayer on ZnSe would give rise to an n-type Schottky barrier height which is the weighted average of the Au/ZnSe and Zn/ZnSe barrier heights: $\Phi_n(Au_{1-x}Zn_x/ZnSe)=(1-x)\cdot\Phi_n(Au/ZnSe)+x\cdot\Phi_n(Zn/ZnSe)$.

The XPS data in Fig. 10 (open circles) are clearly inconsistent with the formation of an homogeneous intermetallic overlayer (dashed line), although the XPS samples are somewhat more affected by alloying effects than the I-V (solid circles) and C-V (solid squares) samples.

7.4. Conclusions

We have shown that previously unreported interface reactions at selected surface sites might be involved in determining a ±0.06 eV lateral inhomogeneity of the Schottky barrier height at Au/ZnSe(001) 2x1 contacts. Larger lateral inhomogeneities reported in the literature are not encountered in state-of-the-art contacts fabricated by MBE and should be ascribed to contaminants and/or extrinsic defects. By fabricating ultrathin Zn interlayers at the Au/ZnSe(001) 2x1 interface, we were able to greatly reduce the lateral inhomogeneities in the barrier and continuously tune the value of the barrier height.

Chapter eight: Conclusions

Our thesis work has focused on two main issues relevant to the physics and technology of wide-bandgap II-VI materials: i) the effect of strain in ZnCdSe quantum wells and the implementation of strain free emitters; ii) the optimisation of the properties of metal/II-VI contacts through modification of the local interface environment.

On the first subject, we showed that graded composition $In_xGa_{1-x}As$ buffer layers on GaAs (001) wafers can be used to match the $Zn_{1-y}Cd_ySe$ quantum well lattice parameter. Detailed studies of electronic and structural properties of $Zn_{1-z}Mg_zSe$ alloys allowed us to fabricate strain-free $Zn_{1-y}Cd_ySe/Zn_{1-z}Mg_zSe$ multiple quantum wells on the novel InGaAs graded composition buffers. We showed that the surface corrugations of the III-V buffer do not hinder the structural quality of the quantum wells, and give only rise to long-period coherent undulations of quantum well and barrier layers. The optical emission and absorption of the new strain-free multiple quantum wells were found to compare well with those of the highest-quality, pseudomorphic $Zn_{1-y}Cd_ySe/ZnSe$ quantum wells in the literature. Modelling of the observed excitonic transition energies was used to determine the electronic parameters crucial for electronic confinement and excitonic stability.

These promising results open the way to the use of strain-free $Zn_{1-y}Cd_ySe/Zn_{1-z}Mg_zSe$ quantum wells to quantitatively evaluate the effect of strain on laser degradation. This will require minimisation of the stacking fault density and stimulated emission studies. In the structure described in Chapter 5, we made no attempt at minimizing the stacking fault density. We are now growing the same strain-free structure using interface fabrication protocols (Zn pre-dosing, and low BPR CIL insertion, see Chapter 5) which have been shown to reduce the stacking fault density in ZnSe/GaAs and ZnMgSSe/ZnSe interface below the $10^4/cm^2$ range.[90,91] Having achieved the desired reduction in stacking fault density, we will be in the position of directly comparing the degradation rate of strain-free structures with those of the conventional, highly strained, pseudomorphic quantum wells. The first optical pumping studies are scheduled at the

beginning of December, in collaboration with the research group of Dr. Cingolani at the University of Lecce.

As far as metal/semiconductor junctions were concerned, our experimental studies of Zn/ZnSe (001) confirmed new theoretical predictions, to the effect that this interface should represent a prototype of an ideally unreactive metal/ZnSe contact. We found instead that Au/ZnSe contacts exhibit evidence of interface reactions, in contrast with most earlier reports, and significant lateral inhomogeneities in the interface parameters, possibly related to preferential reactions at surface steps and kinks. By inserting ultrathin layers of Zn at the interface between Au and ZnSe(001), we were able to induce both large modifications in the Schottky barrier height, and an improved lateral homogeneity and ideality of the resulting metal/ZnSe contacts. Having successfully completed this important proof-of-concept, we envision two different avenues for future investigations. First, analogous studies should be directed to high work-function metal overlayers. In particular the reactive Pd/ZnSe (001) interface,[110,158] and the reportedly unreactive Pt/ZnSe (001) interface[158,159] are of special interest, in view of their current importance for contact fabrication to p-type, wide-bandgap II-VI semiconductors. Second, to the most promising prototype metallization, addition of suitable local interface dipoles to further lower the p-Schottky barrier height should be explored. Such local interface dipoles have been successfully implemented through the fabrication of Si bilayers in metal/III-V contacts, and the same technique could be extended to metal/II-VI junctions through the use of appropriate heterovalent interlayers. In view of the lattice matching and valence difference involved, Ge bilayers grown under cation flux seem promising candidates. Alternatively, the fabrication of doping interface dipoles[160] by means of nitrogen- and chlorine-δ-doped layers could be envisioned.

Acknowledgments

I thank all of my collaborators for their contributions to this work.

Of particular importance were the efforts of my research advisor, Prof. Alfonso Franciosi, in many long and productive discussions of the experimental results.

A special "thanks" goes to my co-workers Silvia Rubini and Beatrice Bonanni, for their primary contribution to the success of this research work, and, for sure, also because they had the patience to stand me for nearly four years.

I necessarily have also to thank young Esubalew (age: 4) for his impressive work in colouring the figures of this thesis (not shown).

Last but not least, I am extremely grateful to Professor Hommel for his steadfast support.

Publications

1. E. Pelucchi, S. De Rossi and F. Ciccacci, "Spin polarized photoemission from thin GaAs photocatodes", J. Electr. Spect. Rel. Phenom. **76**, 505 (1995).
2. F. Ciccacci, S. De Rossi, E. Pelucchi and A. Tagliaferri, "Spin-resolved Electron Spectroscopy with highly polarized sources: Inverse Photoemission from Ferromagnets", Rev. Sci. Instrum. **68**, 1841 (1997).
3. C. Cai, M.I. Nathan, S. Rubini, L. Sorba, B. Mueller, E. Pelucchi and A. Franciosi, "Electrical properties of n-n ZnSe/In(0.04)Ga(0.96)As (001) heterojunctions", Appl. Phys. Lett. **73**, 2033 (1998).
4. S. Rubini, B. Bonanni, E. Pelucchi, A. Franciosi, Y. Zhuang and G. Bauer, "CdTe epitaxial layers in ZnSe-based heterostructures", J. Crystal Growth **201/202**, 465 (1999).
5. A. Hierro, D. Kwon, S.H. Goss, L.J. Brillson, S.A. Ringel, S. Rubini, E. Pelucchi and A. Franciosi, "Evidence for a dominant midgap trap in n-ZnSe grown by molecular beam epitaxy", Appl. Phys. Lett. **75,** 832 (1999).
6. A. Hierro, D. Kwon, S.A. Ringel, S. Rubini, E. Pelucchi and A. Franciosi, "Photocapacitance study of bulk deep levels in ZnSe grown by molecular-beam epitaxy" J. Appl. Phys. **87**, 730 (2000).
7. C. Marinelli, L. Sorba, M. Lazzarino, D. Kumar, E. Pelucchi, B.H. Muller, D. Orani, S. Rubini, and A. Franciosi, "Tunable Schottky barrier contacts to In(x)Ga(1-x)As", J. Vac. Sci. Technol. B **18**, 2119 (2000).
8. S. Rubini, B. Bonanni, E. Pelucchi, A. Franciosi, A. Garulli, A. Parisini, Y. Zhuang, G. Bauer, and V. Holy', "ZnSe/CdTe/ZnSe heterostructures", J. Vac. Sci. Technol. B **18**, 2263 (2000).
9. B. Bonanni, E. Pelucchi, S. Rubini, D. Orani, A. Franciosi, A. Garulli, and A. Parisini, "Excitonic properties and band alignment in lattice-matched ZnCdSe/ZnMgSe multiple quantum well structures", Appl. Phys. Lett **78,** 434 (2001).
10. E. Pelucchi, S. Rubini, B. Bonanni, A. Franciosi, and M. Peressi, "Band discontinuities in ZnMgSe/ZnCdSe(001) lattice-matched heterostructures", to appear in APL.

11 S. Rubini, E. Milocco, L. Sorba, E. Pelucchi, A. Franciosi, A. Garulli, A. Parisini, Y. Zhuang, and G. Bauer, "Structural and electronic properties of ZnSe/AlAs heterojunctions", to appear in PRB.

12. S. Rubini, E. Pelucchi, M. Lazzarino, D. Kumar, and A. Franciosi, "Ideal unreactive metal/semiconductor interfaces: the case of Zn/ZnSe(001)", submitted to PRB.

13. E. Pelucchi, S. Rubini, B. Bonanni, A. Franciosi, M. Peressi, D. De Salvador, F. Romanato, and A. Drigo, "Structural properties of wide-bandgap $Zn_{1-x}Mg_xSe$ alloys", to be submitted to PRB.

14. E. Pelucchi, S. Rubini, D. Kumar, M. Lazzarino and A. Franciosi, "Microscopic properties of Au/Zn contacts to ZnSe (001)", to be submitted to JVST.

Communications

1. S. De Rossi, E Pelucchi (*presenting author*), and F Ciccacci, "Low energy Mott polarimetry of strained GaAs photocatodes", 19th Annual Meeting on Advances in Surface and Interface Physics, Modena (Italy), December 19-21, (1994).

2. E. Pelucchi, B. Bonanni, S. Rubini, and A. Franciosi, "Zn(1-y)Mg(y)Se/Zn(1-x)Cd(x)Se lattice matched heterostructures", 17th General Conference of the CONDENSED MATTER DIVISION of the European Physical Society, Grenoble (1998).

3. S. Rubini, B. Bonanni, E. Pelucchi, A. Franciosi, Y. Zhuang, and G. Bauer, "CdTe epitaxial layers in ZnSe-based heterostructures", 10th International Conference on Molecular Beam Epitaxy, Cannes (1998)

4/5. E. Pelucchi, B. Bonanni, S. Rubini, and A. Franciosi, "Molecular Beam Epitaxy of Zn(1-y)Mg(y)Se/Zn(1-x)Cd(x)Se lattice matched heterostructures"; S. Rubini, B. Bonanni, E. Pelucchi, A. Franciosi, A. Garulli, and A. Parisini " MBE growth and characterisation of ZnSe/CdTe heterostructures", National Conference on the Physics of Matter, Rimini (1998).

6/7 S. Rubini, B. Bonanni, E. Pelucchi, M. Lazzarino, S. Heun, R. Lantier, B. Muller, L. Sorba and A. Franciosi, "II-VI/III-V Heterointerfaces"; E. Pelucchi, S. Rubini, D.

Kumar, M. Lazzarino and A. Franciosi, "In situ Zn and Au contact fabrication to ZnSe", International Workshop on Advances in Growth and Characterization of II-VI Semiconductors, Wuerzburg (1999).

8/9/10. B. Bonanni, E. Pelucchi, S. Rubini, D. Orani and A. Franciosi, "Strain-free Wide-gap multiple Quantum Well Structures"; D. Kumar, E. Pelucchi, S. Rubini, M. Lazzarino and A. Franciosi, "Au/Zn Tunable Schottky Barrier to ZnSe"; D. Orani, S. Rubini, S. Cozzi, E. Pelucchi and A. Franciosi "Al/GaN(0001) Junctions Fabricated in-situ by molecular Beam Epitaxy", National Conference on the Physics of Matter, Catania (1999).

11/12 E. Pelucchi (*oral presentation*), S. Rubini, B. Bonanni, A. Franciosi, M. Peressi, D. De Salvador, F. Romanato, and A. Drigo, "Theoretical and experimental structural properties of ZnMgSe alloys"; B. Bonanni, E. Pelucchi, S. Rubini, A. Franciosi, "Excitonic properties and band alignment in lattice-matched ZnCdSe/ZnMgSe multiple quantum well structures", PBULD II-VI Workshop, Trieste (2000).

13/14/15E. Pelucchi, S. Rubini, B. Bonanni, A. Franciosi, M. Peressi, D. De Salvador, F. Romanato, and A. Drigo, "Electronic and structural properties of ZnMgSe alloys ternary alloys"; B. Bonanni, E. Pelucchi, S. Rubini, and A. Franciosi, "Excitonic properties and band alignment in lattice-matched ZnCdSe/ZnMgSe multiple quantum well structures"; D. Orani, S. Rubini, M. Piccin, E. Pelucchi, A. Franciosi, A. Passasseo, M. Lomascolo, R. Cingolani, "Tunability of the Schottky barrier height for metal contacts to GaN(0001)", National Conference on the Physics of Matter, Genova (2000).

[1] M.A. Haase, J. Qiu, J.M. DePuydt, and H. Cheng, Appl. Phys. Lett. **59**, 1272 (1991).

[2] H. Jeon, J. Ding, W. Patterson, A. Nurmikko, W. Xie, D. Grillo, M. Kobayashi, and R.L. Gunshor, Appl. Phys. Lett. **59**, (3619).

[3] N. Nakayama, S. Itoh, T. Ohata, K. Nakano, H. Okuyama, M. Ozawa, A. Ishibashi, M. Ikeda, and Y. Mori, Electron. Lett. **29**, 1488 (1993).

[4] A. Salokatv, H. Jeon, J.H. Ding, M. Hovinen, A.V. Nurmikko, D.C. Grillo, L. He, J. Han, Y. Fan, M. Ringle, R.L. Gunshor, G.C. Hua, and N. Otsuka, Electron. Lett. **29**, 2192 (1993).

[5] E. Kato, H. Noguchi, M. Nagai, H. Okuyama, S. Kijima, and A. Ishibashi, Electron. Lett. **34**, 282 (1998).

[6] S. Tanighchi, T. Hino, S. Itoh, K. Nakano, N. Nakayama, A. Ishibashi, and M. Ikeda, Electron. Lett. **32**, 552 (1996).

[7] M. Strassburg, O. Schulz, U.W. Pohl, D. Bimberg, S. Itoh, K. Nakano, and A. Ishibashi, Electron. Lett. **36**, 44 (2000).

[8] A. Toda, K. Nakano, and A. Ishibashi, Appl. Phys. Lett. **73**, 1523 (1998).

[9] R. Vogelgesang, J.J. Liang, V. Wagner, H.J. Lugauer, J. Geurts, A. Waag, and G. Landwehr, Appl. Phys. Lett. **75**, 1351 (1999).

[10] J.-M. Bonard, J.-D. Ganiere, L. Vanzetti, J.J. Paggel, L. Sorba, A. Franciosi, D. Hervé, and E. Molva, J. Appl. Phys. **84**, 1263 (1998).

[11] B.H. Müller, S. Heun, R. Lantier, S. Rubini, J.J. Paggel, L. Sorba, A. Bonanni, M. Lazzarino, B. Bonanni, A. Franciosi, E. Napolitani, F. Romanato, A. Drigo, J.-M. Bonard and J.-D. Ganiere, L. Lazzarini and G. Salviati, J. Vac. Sci. Technol. B **16**, 2334 (1998).

[12] B.H. Müller, R. Lantier, L. Sorba, S. Heun, S. Rubini, M. Lazzarino, A. Franciosi, E. Napolitani, F. Romanato, A.V. Drigo, L. Lazzarini and G. Salviati, J. Appl. Phys **85**, 8160 (1999).

[13] L. Zeng, B.X. Yang, A. Cavus, W. Lin, Y.Y. Luo, M.C. Tamargo, Y. Guo, and Y.C. Chen, Appl. Phys. Lett. **72**, 3136 (1998); W. Lin, B.X. Yang, S.P. Guo, A. Elmoumni, F. Fernandez, and M.C. Tamargo, Appl. Phys. Lett. **75**, 2608 (1999).

[14] M. Lomascolo, M. DiDio, D. Greco, L. Calcagnile, R. Cingolani, L. Vanzetti, L. Sorba, and A. Franciosi, Appl. Phys. Lett. **69**, 1145 (1996); R. Cingolani, L. Calcagnile, G. Colí, R. Rinaldi, M. Lomascolo, M. DiDio, A. Franciosi, L. Vanzetti, G. C. LaRocca, and D. Campi, J. Opt. Soc. Am. B **13**, 1268 (1996).

[15] F.P. Logue, P. Rees, J.E. Heffernan, C. Jordan, J.F. Donegan, J. Hegarty, E. Hiei, S. Taniguchi, T. Hino, K. Nakano, and A. Ishibashi, J. Opt. Soc. Am. B **15**, 1295 (1998).

[16] K. Ohkawa, T. Karasawa, T. Mitsuyu, Jpn. J. Appl. Phys. **30**, L152.

[17] Y. Fan, J. Han, L. He, J. Saraie, R.L. Gunshor, M. Hagerott, H. Jeon, A.V. Nurmikko, G.C. Hua, and N. Otsuka, J. Vac. Sci. Technol. B **11**, 1748 (1993).

[18] S. Kijima, H. Okuyama, Y. Sanaka, T. Kobayashi, S. Tomiya, and A. Ishibashi, Appl. Phys. Lett. **73**, 235 (1998).

[19] S. Tomiya, S. Kijima, H. Okuyama, H. Tsukamoto, T. Hino, S. Taniguchi, H. Noguchi, E. Kato, and A. Ishibashi, J. Appl. Phys. **86**, 3616 (1999).

[20] M. Ozawa, F. Hiei, A. Ishibashi, and K. Akimoto, Electr. Lett. **29**, 503.

[21] I. Karpov, N. Venkateswaran, G. Bratina, W. Gladfelter, A. Franciosi, and L. Sorba, J. Vac. Sci. Technol. B **13**, 2041 (1995).

[22] Y. Fan, I. Karpov, G. Bratina, L. Sorba, W. Gladfelter, and A. Franciosi, J. Vac. Sci. Technol. B **14**, 623 (1996).

[23] See for example: M.C. Tamargo, J.L. de Miguel, D.M. Hwang, and H.H. Farrell, J. Vac. Sci. Technol. B **6**, 784 (1988), J. Qiu, Q.D. Qian, M. Kobayashi, R.L. Gunshor, D.R. Menke, D. Li, and N. Otsuka, J. Vac. Sci. Technol. B **8**, 701 (1990), S. Guha, H. Munekata, F.K. LeGoues, and L.L. Chang, Appl. Phys. Lett. **60**, 3220 (1992).

[24] Throughout this thesis the mismatch is defined as follows: $(a_0-a_s)/a_s$; where a_0 is the free standing lattice parameter of the InGaAs epilayer and a_s is the lattice parameter of the GaAs substrate. The elastic deformation will be quantified in terms of the diagonal components of the strain tensor $\varepsilon_\perp$ and $\varepsilon_{//}$: $\varepsilon_{//}=(a_{//}-a_0)/a_0$; $\varepsilon_\perp=(a_\perp-a_0)/a_0$; where $a_{//}$ and $a_\perp$ are the parallel and perpendicular lattice parameters of the strained layer, respectively. In a biaxial strain field with small distortions the two values are connected to each other and with the tetragonal distortion by

the simple equations: $\varepsilon_{\perp}=-\alpha\varepsilon_{//}$,$\alpha= 2C_{12}/C_{11}=2\nu/\nu-1$, where C_{12} and C_{11} are the elastic stiffness constants and ν is Poisson's ratio.

[25] A. V. Drigo, A. Aydinli, A. Carnera, F. Genova, C. Rigo, C. Ferrari. P. Franzosi, and G. Salviati, J. Appl. Phys. **66**, 1975 (1989), and references therein.

[26] S. Heun, J.J. Paggel, S. Rubini, and A. Franciosi, J. Vac. Sci. Technol. B **14**, 2980 (1996).

[27] S. Heun, J. J. Paggel, L. Sorba, S. Rubini, A. Bonanni, R. Lantier, M. Lazzarino, B. Bonanni, A. Franciosi, J.-M. Bonard, J.-D. Ganière, Y. Zhuang, and G. Bauer, J. Appl. Phys. **83**, 2504 (1998).

[28] A. Bosacchi, A. C. De Riccardis, P. Frigeri, S. Franchi, C. Ferrari, S. Gennari, L. Nasi, G. Salviati, A. V. Drigo, and F. Romanato, J. Cryst. Growth **175/176**, 1009 (1997); L. Lazzarini, C. Ferrari, S. Gennari, A. Bosacchi, S. Franchi, F. Romanato, M. Berti, A. V. Drigo, and G. Salviati, Inst. Phys. Conf. Ser. **157**, 149 (1997).

[29] F. Romanato, E. Napolitani, A. Carnera, A. Drigo, L. Lazzarini, G. Salviati, C. Ferrari, A. Bosacchi, and S. Franchi, J. Appl. Phys **86**, 4748 (1999).

[30] N. Grandjean, and J. Massies, J. Cryst. Growth **134**, 51 (1993).

[31] K. H. Chang, R. Gibala, D. J. Srolovitz, P. K. Bhattacharya, and J.F. Mansfield, J. Appl. Phys. **67**, 4093 (1990); S. F. Yoon, J. Vac. Sci. Technol. B **11**, 562 (1993).

[32] E. A. Fitzgerald, Y. H. Xie, M. L. Green, D. Brasen, A. R. Kortan, J. Michel, Y. J. Mii, and B. E. Weir, Appl. Phys. Lett. **59**, 811 (1991).

[33] J. Tersoff, Appl. Phys. Lett. **62**, 693 (1993).

[34] R. Beanland, M. Aindow, T. B. Joyce, P. Kidd, M. Lourenço, and P. J. Goodhew, J. Cryst. Growth 149,1 (1995); S. Pal and D. P. Landau, Phys. Rev. B **49**, 10597 (1994).

[35] S.Y. Shiryaev, F. Jensen, and J.W. Petersen, Appl. Phys. Lett. **64**, 3305, 3305 (1994).

[36] B. Jobst, D. Hommel, U. Lunz, T Gerhard, G Landwehr, Appl. Phys. Lett. **69**, 97 (1996).

[37] H. Okuyama, Y. Kishita, and A. Ishibashi, Phys. Rev. B **57**, 2257 (1998).

[38] J. Puls, M. Rabe, A. Siarkos, and F. Henneberger, Phys. Rev. B **57**, 14749 (1998).

[39] B. Vögele, C. Morhain, B. Urbaszek, S.A. Telfer, K.A. Prior, B.C. Cavenett, J. Cryst. Growth **201/202**, 950 (1999).

[40] M. Wörz, E. Griebl, Th. Reisinger, R. Flierl, B. Haserer, T. Semmer, T. Frey, W. Gebhardt, Phys. Stat. Sol. (b) **202**, 805 (1997).

[41] J. Petruzzello, B. L. Greenberg, D.A. Cammack, and R. Dalby, J. Appl. Phys. **63**, 2299 (1988).

[42] M.Th. Litz, K. Watanabe, M. Korn, H. Ress, U. Lunz, W. Ossau, A. Waag, G. Landwehr, Th. Walter, B. Neubauer, D. Gerthsen, U. Schüssler, J. Cryst. Growth **159**, 54 (1996).

[43] S. Adachi, and T. Taguchi, Phys. Rev. B **43**, 9569 (1991) report a ZnSe RT gap of 2.69 eV; U. Lunz, B. Jobst, S. Einfeldt, C.R. Becker, D. Hommel. And G. Landwehr, J. Appl. Phys. **77**, 5377 (1995), found a ZnSe RT gap of 2.68 eV; while C. C. Kim, and S. Sivananthan, Phys. Rev. B **53**, 1475 (1996) report a RT gap of 2.711 eV. Our determined ZnSe RT bandgap is 2.694 eV.

[44] U. Lunz, C. Schumacher, J. Schull, A. Gerhard, U. Schüssler, B. Jobst, W. Fashinger, and G. Landwehr, Semicond. Sci. Technol. **12**, 970 (1997).

[45] We are using here the estimated temperature dependence of MgSe bandgap that can be found in K. Watanabe, M. Th. Litz, M. Korn, W. Ossau, A. Waag, G. Landwehr, and U. Schüssler, J. Appl. Phys. **81**, 451 (1997).

[46] G. Kalpana, B. Palanivel, Reena Mary Thomas, M. Rajagopalan, Physica B **222**, 223 (1996).

[47] R. Pandey and A. Sutjianto, Solid State Commun. **91**, 269 (1994).

[48] A.M. Saitta, S. de Gironcoli, and S. Baroni, Phys. Rev. Lett. **80**, 4939 (1998).

[49] A.M. Saitta, S. de Gironcoli, S. Baroni, Appl. Phys. Lett. **75**, 2746 (1999).

[50] Sun-Ghil Lee and K. J. Chang, Phys. Rev. B **52**, 1918 (1995).

[51] W.J. Bartels, J. Vac. Sci. Technol. B **1**, 338 (1983).

[52] "Numerical Data and Functional Relationships in Science and Technology", Group III, vol. 17 a-b, 22 a, edited by Landolt-Bornstein (Springer, New York, 1982).

[53] A.T. Macrander, G.P. Schwartz, and G.J. Gualtieri, J. Appl. Phys. **64**, 6733 (1988).

[54] K. Pinardi, Uma Jain, S.C. Jain, H.E. Maes, R. Van Overstraeten, and M. Willander, J. Appl. Phys. **83**, 4724 (1998).

[55] To determine the equilibrium lattice constant of the $Zn_{1-x}Mg_xSe$ alloys from the observed tetragonal distortion of the layers, the elastic stiffness constants of the material need to be known and a self consistent system of equations solved, in which the dependence of the lattice parameter

and of the elastic stiffness constants on concentration are known. Only for the purpose of determining which were the correct lattice parameters, Vegard's law has been used for both the lattice parameter and the elastic stiffness constants, using ZnSe and MgSe parameters as end points. The above-discussed reported discrepancies about Vegard's law would introduce a totally negligible error in the determination of the lattice parameter with this procedure. The lattice parameters used for ZnSe and MgSe have been respectively 5.6687Å (see Ref. 41) and 5.904Å (see Ref. 44). The value of C_{12}/C_{11} for ZnSe was 0.603 (see Ref. 41), 0.708 for MgSe. C_{11} and C_{12} elastic constants of MgSe have been calculated in the plane-wave pseudopotential framework of density functional theory, by numerical differentiation of the stress tensor with respect to uniaxial cell deformation (±1%) in the (001) direction, by Dr. S. de Gironcoli (private communication).

[56] D.J. Dunstan, H.G. Colson, and A.C. Kimber, J. Appl. Phys. **86**, 782 (1999).

[57] The lattice parameter for CdSe is 6.077 Å, as reported by N. Samarth, H. Luo, J.K. Furdyna, S.B. Qadri, Y.R. Lee, A.K. Ramdas, and N. Otsuka, Appl. Phys. Lett. **54**, 2680 (1989).

[58] J.J. Yeh and I. Lindau, At. Data Nucl. Data Tables **32**, 1(1985).

[59] The same techniques has been applied elsewhere (see ref. 134) for the evaluation of S(In $4d_{5/2}$)/S(Ga 3d) and S(In $3d_{5/2}$)/S(Ga 3d). In that case differences between theory and experiment were around 5%.

[60] C. Cohen, J.A. Davis, A.V. Drigo and T.E. Jackman, Nucl. Instrum. Methods Phus. Res. **218**, 174 (1983).

[61] Handbook of Modern Ion Beam Analysis, edited by J.R. Tesmer and M. Nastasi (Materials Research Society, Pittsburgh, 1995).

[62] J.F. Ziegler, Stopping Power and Ranges of Ions in Matter (Pergamon Press, New York, 1977), Vol. 4.

[63] The simplest approach would be the "virtual-crystal approximation" (VCA) where the Zn(1-x)Mg(x)Se alloy is described by a fictitious zincblende compound with a cation sublattice containing a single type of atoms: the virtual cation <Zn(1-x)Mg(x)>, whose atomic pseudopotential is a weighted average of those of Zn and Mg. By its nature, the VCA approach could not reproduce any feature of the structural or electronic properties related to individual kind

of cation. Furthermore, also some macroscopic properties such as the average lattice parameter would be poorly estimated within the VCA. We have really compared the VCA results for the DOS of the alloys studied here, and we have seen that they are appreciably different from those obtained with the "true" atom supercell approach.

[64] A. Zunger A., S.-H. Wei, L. G. Ferreira, and J. E. Bernard, Phys. Rev. Lett. **65**, 353 (1990); S.-H. Wei, L. G. Ferreira, J. E. Bernard, and A. Zunger, Phys. Rev. B **42**, 9622 (1990).

[65] A. Baldereschi and M. Peressi, Journal of Physics: Condens. Matter **5**, B37 (1993).

[66] U. Tinivella, M. Peressi, and A. Baldereschi, J. Phys.: Condens. Matter **9**, 11141 (1997).

[67] A. Wall, Y. Gao, A. Raisanen, A. Franciosi, and J.R. Chelikowsky, Phys. Rev. B **43**, 4988 (1991).

[68] P.Y. Yu and M. Cardona, Fundamentals of Semiconductors (Springer-Verlag, Berlin, 1996).

[69] The LT gap was obtained by adding the exciton emission energy the exciton binding energy dependence on lattice parameter reported by Wörz et al. (see Ref. 40).

[70] We used this functional dependence, the data of Fig. 1 and the two different LT bandgap dependencies on concentration reported by Puls et al. and Vögele et al. to determine the RT bandgap dependencies on concentration shown in Fig. 2 for Puls et al. and Vögele et al.

[71] The data of Jobst et al. show a pronounced deviation from a linear dependence of band gap vs. lattice parameter only for lattice parameters above 5.85Å. The parabolic fitting procedure used by the authors emphasize the bowing in the fitting curve also at lower lattice parameters. We think that a more genuine comparison with Jobst et al. data in the range of lattice parameters shown in Fig. 5 would result if a linear fitting of Jobst et al. data below 5.85Å is shown.

[72] M. P. Seah and W. A. Dench: "Quantitative Electron Spectroscopy of Surfaces: A Standard Data Base for Electron Inelastic Mean Free Paths in Solids", Surf. Interface Anal. I (1979).

[73] In the kinetic-energy range of interest, the escape depth of normally emitted Zn 3d and Mg 2p photoelectrons is 26.6 Å, see E.A. Kraut, R.W. Grant, J.R. Waldrop, and S. P. Kowalczyk, Phys. Rev. B **28**, 1965 (1983). In our experimental geometry the average photoelectron collection angle is 55° from the sample normal, leading to an effective escape depth of about 15.3 Å.

[74] The 4MeV beam samples the whole II-VI layer and part of the GaAs substrate, as can be derived from Ref. 62. The concentration value, on the other hand, was derived only by considering energies from 3000 to 3300 keV. This energy range corresponds to roughly the first 3000Å of the sample (see Ref. 62)

[75] A.D. Katnani, and G. Margaritondo, Phys. Rev. B **28**, 1944 (1983).

[76] J.R. Waldrop, R.W. Grant, and E.A. Kraut, J. Vac. Sci. Technol. B **5**, 1209 (1987).

[77] L. Sorba, G. Bratina, A. Antonini, A. Franciosi, L. Tapfer, A. Migliori, and P. Merli, Phys. Rev. B **46**, 6834 (1992).

[78] A. Franciosi, and C.G. Van de Walle, Surf. Sci. Rep. **25**, 1 (1996), and references therein.

[79] Room temperature bandgap values employed were 2.560 eV for $Zn_{0.9}Cd_{0.1}Se$, 2.497 eV for $Zn_{0.85}Cd_{0.15}Se$ and 2.020 eV for $Zn_{0.42}Cd_{0.58}Se$. See Y. D. Kim, M. V. Klein, S. F. Ren, Y.C. Chang, H. Luo, N. Samarth, and J. K. Furdyna, Phys. Rev. B **49**, 7262 (1994).

[80] M.W. Wang, J. F. Swenberg, M.C. Phillips, E.T. Yu, J.O. McCaldin, R.W. Grant, T.C. McGill, Appl. Phys. Lett. **64**, 3455 (1994).

[81] A. Baldereschi, R. Resta, M. Peressi, S. Baroni, and K. Mäder, in Proc. NATO Adv. Res. Workshop Physical *Properties of Semiconductor Interfaces at Sub-Nanometer Scale*, H.W. Salemink, ed. (Kluwer Academic Publishers, Dordrecht, 1993).

[82] E. Griebl, B. Haserer, T. Frey, T. Reisenger, and W. Gebhardt, Phys. Status Sol. (b) **198**, 355 (1996).

[83] S.B. Zhang, D. Tomanek, S. G. Louie, M. L. Cohen and M. S. Hybertsen, Sol. State Comm. **66**, 585 (1988); X. Zhu and S.G. Louie, Phys. Rev. B **43**, 14142 (1991).

[84] Such cross-hatched surfaces are known to occur in both $In_yGa_{1-y}As$ alloys and $Si_{1-x}Ge_x$ epilayers during growth on lattice-mismatched substrates and have been related to local variations in growth rate or slip-steps resulting from the misfit dislocation network at the overlayer-substrate interface. See Chapter 2 and references therein for further details.

[85] Room temperature bandgap employed for $Zn_{0.85}Mg_{0.15}Se$ and $Zn_{0.74}Mg_{0.26}Se$ have been 2.855 eV for $Zn_{0.85}Mg_{0.15}Se$ and 2.936 for $Zn_{0.85}Mg_{0.15}Se$, as derived from optical absorption data, as discussed in Chapter 3, and 4.05 eV for MgSe, from U. Lunz et al.[44].

[86] The low-temperature bandgap of $Zn_{1-x}Cd_xSe$ has been evaluated using the room temperature bandgap in Ref. 79 and the bandgap temperature-dependence for CdSe and ZnSe reported by W. Shan, J. J. Song, H. Luo, and J. K. Furdyna, Phys. Rev. B **50**, 8012 (1994), and by N. Garro, A. Cantarero, M. Cardona, A. Göbel, T. Ruf, and K. Eberl, Phys. Rev. B **54**, 4732 (1996), respectively. We obtained 2.669 eV for $Zn_{0.9}Cd_{0.1}Se$, 2.606 eV for $Zn_{0.85}Cd_{0.15}Se$, and 2.129 eV for $Zn_{0.42}Cd_{0.58}Se$. The low-temperature bandgap of $Zn_{1-y}Mg_ySe$ was evaluated from our photoluminescence results, adding to the exciton emission energy, at T=15K, the exciton binding energy, as estimated by linearly interpolating the reported values in ZnSe (Ref. 52) and MgSe (Ref. 40). We obtained 2.996 eV for $Zn_{0.85}Mg_{0.15}Se$ and 3.088 eV for $Zn_{0.74}Mg_{0.26}Se$. For MgSe Lunz et al.[44] observed a room-temperature bandgap of 4.05 eV, from which K. Watanabe, M. Th. Litz, M. Korn, W. Ossau, A. Waag, G. Landwehr, and U. Scüssler, J. Appl. Phys. **81**, 451 (1997), estimated a value of 4.24 eV at 0 K.

[87] J. M. Gaines, J. Petruzzello, and B. Greenberg, J. Appl. Phys. **73**, 2835 (1993).

[88] L. H. Kuo, L. Salamanca-Riba, J. M. DePuydt, H. Cheng, and J. Qiu, Appl. Phys. Lett. **63**, 3197 (1993); L. H. Kuo, L. Salamanca-Riba, J.M. DePuydt, H. Cheng, and J. Qiu, Philos. Mag. A **69**, 301 (1994); L. H. Kuo, L. Salamanca-Riba, G. Hofler, B.J. Wu, and M. A. Haase, Proc. SPIE **2228**, 144 (1994); B.J. Wu, G. M. Haugen, J. M. DePuydt, L.H. Kuo, and L. Salamanca-Riba, Appl. Phys. Lett. **68**, 2828 (1996).

[89] S. Guha, H. Munekata, and L. L. Chang, J. Appl. Phys. **73**, 2294 (1993).

[90] S. Taniguchi, T. Hino, S. Itoh, N. Nakayama, A. Ishibashi, and M. Ikeda, Electron. Lett. **32**, 552 (1996).

[91] S. Heun, J.J. Paggel, S. Rubini, L. Sorba, A. Franciosi, J.M. Bonard, and J.D. Ganiere, Appl. Phys. Lett. **70**, 237 (1997);S. Heun, J.J. Paggel, L. Sorba, S. Rubini, A. Franciosi, J.-M. Bonard, and J.-D. Ganiere, J. Vac. Sci. Technol. B **15**, 1279 (1997); J.M. Bonard, J.D. Ganiere, S. Heun, J.J. Paggel, S. Rubini, L. Sorba, and A. Franciosi, Phil. Mag. Lett. **75**, 219 (1997).

[92] J. Gutowski, N. Presser, G.Kudlek, Phys. Status Sol. (a) **120**, 11 (1990).

[93] H. J. Lozykowski and V. K. Shastri, J. Appl. Phys. **69**, 3235 (1991).

[94] D. Greco, R. Cingolani, A. D'Andrea, N. Tommasini, L. Vanzetti, A. Franciosi, Phys. Rev. B **54**, 16998 (1996).

[95] V. Pellegrini, R. Atanasov, A. Tredicucci, F. Beltram, C. Amzulini, L. Sorba, L. Vanzetti, and A. Franciosi, Phys. Rev. B **51**, 5171 (1995); A. De Nardis, V. Pellegrini, R. Colombelli, F. Beltram, L. Vanzetti, A. Franciosi, I.N. Krivorotov, and K.K. Bajaj, Phys. Rev. B **61**, 1700 (2000).

[96] R. Cingolani, P. Prete, D. Greco, P.V. Giugno, M. Lomascolo, R. Rinaldi, L. Calcagnile, L. Vanzetti, L. Sorba, and A. Franciosi, Phys. Rev. B **51**, 5176 (1995); R. Cingolani, G. Bastard, M. Labardi, F. Fuso, M. Allegrini, L. Sorba, L. Vanzetti, and A. Franciosi, J. Appl. Phys. **86**, 6793 (1999).

[97] C. Guérnard, E. Deleporte, A. Filoramo, Ph. Lelong, A. Delande, C. Morhain, E Tournié, and J. P. Faurie, J. Appl. Phys. **87**, 1863 (2000).

[98] G. Bastard, in *Wave Mechanics Applied to Semiconductor Heterostructures* (Les Editions de Physique, Les Ulis, 1988) p. 247.

[99] H. Mathieu, P. Lefebvre, and P. Christol, Phys. Rev. B **46**, 4092 (1992); see also Xing-Fei He, Phys. Rev. B **43**, 2063 (1991).

[100] T. Miyajima, F.P. Logue, J.F. Donegan, J. Hegarty, H. Okuyama, A. Ishibashi, and Y. Mori, Appl. Phys. Lett. **66**, 180 (1995).

[101] For the quantum wells we used $m_e=0.1355m_0$, $m_{hh}=0.484m_0$, and $m_{lh}=0.145m_0$, for electrons, heavy- and light-holes, respectively. See Ref. 95 for details.

[102] M. Nagelstrasser, H. Dröge, F. Fisher, T. Litz, A. Waag, G. Landwehr, H.-P. Steinrück, J. Appl. Phys. **83**, 4253 (1998).

[103] T. Walter, A. Rosenauer, R. Wittmann, D. Gerthsen, F. Fisher, T. Gerhard, A. Waag, G. Landwehr, P. Shunk, and T. Shimmel, Phys. Rev. B **59**, 8114 (1999).

[104] W. Mönch, ed., *Electronic Structure of Metal-Semiconductor Contacts* (Kluwer, Dordrecht, 1990).

[105] L.J. Brillson, in: *Handbook on semiconductors*, Vol. I, Ed. P.T. Landsberg (North Holland, Amsterdam, 1992) p. 281.

[106] M. Peressi, N. Binggeli, and A. Baldereschi, J. Phys. D **31**, 1273 (1998), and references therein.

[107] J. Bardi, N. Binggeli, and A. Baldereschi, Phys. Rev. B **59**, 8054 (1999), and references therein.

[108] J. Bardi, N. Binggeli, and A. Baldereschi, Phys. Rev. B **61**, 5416 (2000), and references therein.

[109] W. Chen, A. Khan, P. Soukiassan, P. S. Mangat, J. Gaines, C. Ponzoni and D. Olego, J. Vac. Sci. Technol. B **12**, 2639 (1994).

[110] M. Vos, F. Xu, S.G. Anderson, J.H. Weaver and H. Cheng, Phys. Rev. B **39**, 10744 (1989).

[111] H.H. Farrell, M.C. Tamargo, and S.M. Shibly, J. Vac. Sci. Technol. B **8**, 884 (1990).

[112] M. Lazzarino, G. Scarel, S. Rubini, G. Bratina, L. Sorba, A. Franciosi, C. Berthod, N. Binggeli, and A. Baldereschi, Phys. Rev. B **57**, R9431 (1998).

[113] G.P. Lopinsky, J.R. Fox, J.S. Lannin, F.S. Flack, and N. Samarth, Surf. Sci. **355**, L355 (1996).

[114] S.M. Sze, Physics of Semiconductor Devices (Wiley, New York, 1981).

[115] The expected functional form for the integrated intensity I of a substrate core level as a function of the overlayer thickness θ is $I(\theta)=I_0 \exp(-\theta/\lambda)$, where I_0 is the initial intensity prior to metal deposition, and λ is the effective escape depth of the photoelectrons. In the kinetic energy range of interest for the present study, and our experimental geometry, the effective photoelectron escape depth was about 15 Å, as explained in Ref. 73.

[116] A similar analysis of the intensity of the Zn 3d substrate emission was precluded by the partial superposition with the overlayer Zn 3d emission, the available XPS energy resolution been insufficient to separate the two core doublets with the necessary accuracy.

[117] W. Chen, A. Khan, P. Soukiassan, P. S. Mangat, J. Gaines, C. Ponzoni and D. Olego, Phys. Rev. B **49**, 10790 (1994).

[118] Herbert B. Michaelson, J. Appl. Phys. **48**, 4729 (1977).

[119] F. Xu, M. Vos, J. H. Weaver and H. Cheng, Phys. Rev. B **38**, 13418 (1988).

[120] See, for instance, D. K. Schroder, *Semiconductor Material and Device Characterization,* (Wiley, New York 1990) p. 130-.

[121] R. Stumpf, X. Gonze, and M. Scheffler, Fritz-Haber-Institut Research Report No.1, April 1991.

[122] D.M. Ceperley and B. J. Alder, Phys. Rev. Lett. **45**, 566 (1986).

[123] S.G. Louie, S. Froyen, and M. Cohen, Phys. Rev. B 26, 1738 (1982); in order to properly include the Zn non-linear-core correction, the Zn pseudopotential was generated –with the parameters of Ref. 121- using the *same* atomic configuration ($s^{1.5}$, $p^{0.25}$, $d^{0.25}$) for each *L* component of the pseudopotential.

[124] G. Margaritondo, Rep. Prog. Phys. **62**, 765 (1999).

[125] A.Y. Cho and P.D. Dernier, J. Appl. Phys. **49**, 3328 (1978).

[126] G.A. Prinz, J.M. Ferrari, and M. Goldenberg, Appl. Phys. Lett. **40**, 155 (1982).

[127] R.G. Dandrea and C.B. Duke, J. Vac. Sci. Technol. B **11**, 1553 (1993).

[128] A. Ruini, R. Resta, and S. Baroni, Phys. Rev. B **56**, 14921 (1997).

[129] C.-L. Fu and K.-M. Ho, Phys. Rev. B **28**, 5480 (1983).

[130] C. Berthod, N. Binggeli, and A. Baldereschi, Europhys. Lett. **36**, 67 (1996); C. Berthod, J. Bardi, N. Binggeli, and A. Baldereschi, J. Vac. Sci. Technol. B **14**, 3000 (1996).

[131] C. Berthod, N. Binggeli, and A. Baldereschi, Phys. Rev. B **57**, 9757 (1998).

[132] see for example M. Cantile, L. Sorba, S. Yildirim, P. Faraci, G. Biasiol, A. Franciosi, T.J. Miller, and M.I. Nathan, Appl. Phys. Lett. **64**, 988 (1994); L. Sorba, S. Yildirim, M. Lazzarino, A. Franciosi, D. Chiola, and F. Beltram, Appl. Phys. Lett. **69**, 1927 (1996); L. Sorba, J.J. Paggel, and A. Franciosi, J. Vac. Sci. Technol. B **14**, 29994 (1996); G. Gigli, M. Lomascolo, M. De Vittorio, R. Cingolani, A. Cola, F. Quaranta, L. Sorba, B.H. Müller, and A. Franciosi, Appl. Phys. Lett. **73**, 259 (1998).

[133] S. De Franceschi, F. Beltram, C. Marinelli, L. Sorba, M. Lazzarino, B. Müller, and A. Franciosi, Appl. Phys. Lett. **72**, 1996 (1998); C. Marinelli, L. Sorba, B.H. Müller, D. Kumar, D. Orani, S. Rubini, A. Franciosi, S. De Franceschi, M. Lazzarino, and F. Beltram, J. Cryst. Growth **201/202**, 769 (1999).

[134] C. Marinelli, L. Sorba, M. Lazzarino, D. Kumar, E. Pelucchi, B.H. Müller, D. Orani, S. Rubini, e A. Franciosi, J. Vac. Sci. Technol. B **18**, 2119 (2000).

[135] see for example B.J. Wu, J.M. DePuydt, G.M. Haugen, G.E. Höfler, M.A. Haase, H. Cheng, S. Guha, J. Qiu, L.H. Kuo, and L. Salamanca-Riba, Appl. Phys. Lett. **66**, 3462 (1995); H. Okuyama, Y. Kishita, T. Miyajima, and K. Akimoto, Appl. Phys. Lett. **64**, 904 (1994); E. Tournie', and J.-P. Faurie, Appl. Phys. Lett. **75**, 382 (1999).

[136] R. Coratger, C. Girardin, J. Beauvillain, I.M. Dharmadasa, A.P. Samanthilake, J.E.F. Frost, K.A. Prior, and B.C. Kavenett, J. Appl. Phys. **81**, 7870 (1997), and references therein.

[137] R. Coratger, F. Ajustron, J. Beauvillain, I.M. Dharmadasa, C.J. Blomfield, K.A. Prior, J. Simpson, and B.C. Kavenett, Phys. Rev. B **51**, 2357 (1995), and references therein.

[138] B.A. Morgan, K.M. Ring, K.L. Kavanagh, A.A. Talin, R.S. Williams, T. Yasuda, T. Yasui, and Y. Segawa, J. Appl. Phys. **79**, 1532 (1996), and references therein.

[139] Y. Koide, T. Kawakami, N. Teraguchi, Y. Tomomura, A. Suzuki, and M. Murakami, J. Appl. Phys. **82**, 2393 (1997).

[140] A. Chahboun, R. Coratger, F. Ajustron, J. Beauvillain, I.M. Dharmadasa, and A.P. Samantilleke, J. Appl. Phys. **87**, 2422 (2000).

[141] T. Marshall, S. Colak, and D. Cammack, J. Appl. Phys. **66**, 1753 (1989).

[142] N.T. Tam, and T. Chot, phys. Stat. Sol. (a) **93**, K 91 (1986).

[143] T.G. Andersson, G. Le Lay, J. Kanski, and S.P. Svensson, Phys. Rev. B **36**, 6231 (1987).

[144] see for example: J. Osvald, J. Appl. Phys. **85**, 1935 (1999), and references therein.

[145] R.T. Tung, Phys. Rev. B **45**, 13509 (1992).

[146] G.K. Wertheim, M. Campagna and S. Hüfner, Phys. Cond. Matter **18**, 133 (1974).

[147] M. Cardona and L. Ley, Photoemission in Solids I, II (Springer-Verlag, Berlin, 1978).

[148] J.M. Moison, C. Guille, F. Barthe, and M. Van Rompay, Phys. Rev. B **40**, 6149 (1989).

[149] S.G. Anderson, F. Xu, M. Vos, J.H. Weaver, and H. Cheng, Phys. Rev. B **39**, 5079 (1989).

[150] See, for example, M. W. Ruckman, M. del Giudice, J. J. Joyce, and J. H. Weaver, Phys. Rev. B **34**, 5118 (1986) for Au/Ge; F. Xu, C. M. Aldao, I.M. Vitomirov, and J. H. Weaver, Appl. Phys. Lett. **51**, 1946 (1987) for Au/Si; F. Xu, Y. Shapira, D. M. Hill, and J. H. Weaver, Phys. Rev. B **35**, 7417 (1987) for Au/GaAs; Y. Shapira, L. Brillson, A. D. Katnani, and G. Margaritondo, Phys. Rev. B **30**, 4856 (1984) for Au/InP; Y. Shapira, F. Boscherini, C. Capasso, F. Xu, D. M. Hill, and

J. H. Weaver, Phys. Rev. B **36**, 7656 (1987) for Au/InSb, and the extensive literature cited therein.

[151] M. Hansen, "Constitution of Binary Alloys", 2nd ed. (McGraw-Hill, New York, 1958).

[152] I. Abbati, L. Braicovich, A. Franciosi, I. Lindau, P.R. Skeath, C.Y. Su, and W.E. Spicer, J. Vac. Sci. Technol. **17**, 930 (1980).

[153] R.M. Friedman, J. Hudis, M.L. Perlman, and R.E. Watson, Phys. Rev. B **8**, 2433 (1973).

[154] T.K. Sham, M.L. Perlman, and R.E. Watson, Phys. Rev. B 19, 539 (1979).

[155] A. Nicholson, J.D. Riley, R.C.G. Leckey, J. G. Jenkin, J. Liesegang, and J. Azoulay, Phys. Rev. B **18**, 2561 (1978).

[156] J.C. Fuggle, L.M. Watson, D.J. Fabian, and P.R. Norris, Solid State Commun. **13**, 507 (1973); J.C. Fuggle, E. Källne, L.M. Watson, and D.J. Fabian, Phys. Rev. B **16**, 750 (1977).

[157] I. Abbati, L. Braicovich, and A. Franciosi, Solid State Commun. **33**, 881 (1980).

[158] K.J. Duxstad, E.E. Haller, K.M. Yu, E.D. Bourret, X.W. Lin, S. Ruvimov, Z. Liliental-Weber, and J. Washburn, J. Vac. Sci. Technol. B **15**, 891 (1997) and references therein.

[159] C. Bourgognon, S. Tatarenko, J. Cibert, L. Carbonell, V.H. Etgens, M. Eddrief, B. Gilles, A. Marty, and Y. Samson, Appl. Phys. Lett. **76**, 1455 (2000).

[160] F. Capasso, G. Ripamonti, A.L. Hutchinson, D.J. Meuhlner, J.F. Walker, and R.J. Malik, IEDM Tech. Dig. 902, 491 (1998).